REGIONAL TECTONIC EVOLUTION OF THE PIONEER CORE COMPLEX, SOUTH-CENTRAL IDAHO

A Thesis submitted to the faculty of
San Francisco State University
In partial fulfillment of
the requirements for
the Degree

Master of Science

In

Geoscience

by

Rui Liu

San Francisco, California

January 2017

CERTIFICATION OF APPROVAL

I certify that I have read Regional Tectonic Evolution of the Pioneer Core Complex, South-Central Idaho by Rui Liu, and that in my opinion this work meets the criteria for approving a thesis submitted in partial fulfillment of the requirement for the degree Master of Science in Geoscience at San Francisco State University.

Mary Leech, Ph.D.
Associate Professor

John Caskey, Ph.D.
Associate Professor

Karen Grove, Ph.D.
Emeritus

REGIONAL TECTONIC EVOLUTION OF THE PIONEER CORE COMPLEX, SOUTH-CENTRAL IDAHO

Rui Liu
San Francisco, California
2017

The Pioneer core complex (PCC) is one of lesser-studied Cordilleran metamorphic core complexes (MCCs) located north of the Snake River Plain in the Rocky Mountain region of the western U.S.. Based on analyses of zircon geochronology, Ti thermometry and thermodynamic modeling, the tectonic evolution of the PCC followed a clockwise P-T-t-d path with prograde to peak conditions of 4 kbar and 860°C from 52 to 48 Ma, followed by retrograde metamorphism to 2 kbar and 590°C at 43 Ma. The prograde metamorphism (corresponding to D1) of the PCC began near the start of the Sevier orogeny (before 109 Ma) in the Late Cretaceous as the Farallon plate began to subduct eastward beneath North America. The PCC underwent compressional deformation during the Sevier orogeny at 86-84 Ma (D2) when the subducting Farallon plate flattened and deformation verged eastward. The Eocene Challis magmatism and extension in the PCC (52-43 Ma, corresponding to D3) likely resulted from slab rollback of the Farallon plate and asthenospheric upwelling, under a stalled, accreted microplate (Siletzia).

I certify that the Abstract is a correct representation of the content of this thesis.

Chair, Thesis Committee — Date 12/20/16

ACKNOWLEDGEMENTS

This research was supported by the Pestrong Fund in the Earth & Climate Sciences Department at SF State, and a National Science Foundation CAREER grant (EAR 0847721 to Mary Leech) jointly supported by the Tectonics, Petrology & Geochemistry, and Education & Human Resources programs, for field and lab work. Russell McArthur, Joseph Verdian, Claire Zurkowski, Brandon Swanson, Beth Holmes, Jesse Waco, Nolen Brown, Salvatore Romano provided great assistance in field work. Andrew Nieblas and Jackson Reeder offered valuable help in lab work.

TABLE OF CONTENTS

LIST OF TABLES

Table Page

LIST OF FIGURES

Figures Page

LIST OF APPENDICES

Appendix Page

INTRODUCTION

The Cordilleran metamorphic core complexes (MCCs) are exposures of high-grade, deep crustal rocks exhumed from beneath low-angle detachment faults and a brittle upper plate, that formed during crustal rifting in the Basin and Range province (Armstrong, 1982; Whitney et al., 2013). MCCs are composed of greenschist- to upper amphibolite-facies metamorphic rocks, and they are frequently associated with granitoid intrusions (Haney, 2008). The MCCs of the Basin and Range comprise a belt extending from southern British Columbia, Canada, southward through the western U.S. to Mexico, in the western hinterland of the Cretaceous-Paleogene Sevier-Laramide fold-and-thrust belt (e.g., Armstrong, 1982; Silverberg, 1990; Vogl et al., 2012). The MCCs underwent Mesozoic compressional deformation during the Cretaceous Sevier-Laramide orogeny when the subducting Farallon plate flattened beneath North America; this was followed by Cenozoic extension related to roll-back of the Farallon plate. The extension taking place in the thinned Basin-and-Range crust also triggered volcanism that is associated with the emplacement of plutonic rocks in the Cordilleran core complexes (e.g., Armstrong, 1982; Janecke, 1992, 1994; Lee Armstrong and Ward, 1991; O'neill and Pavlis, 1988; Silverberg, 1990; Vogl et al., 2012; Wust, 1986).

The Pioneer Mountains metamorphic core complex

The Pioneer core complex (PCC) is one of the lesser-studied Cordilleran core complexes, that is located north of the Snake River Plain in the Rocky Mountains. The

complex resides in a transitional zone separating Eocene MCCs to the north and Oligocene-Miocene MCCs to the south (Fig. 1; Armstrong, 1982; Silverberg, 1990; Vogl et al., 2012). The PCC comprises a fan-shaped NW-SE-trending dome that is bounded by the Wildhorse Detachment fault and the high-angle White Mountains normal fault in the southeast (Fig. 1), and it consists of Precambrian-Ordovician metamorphic rocks and Eocene plutonic rocks (O'neill and Pavlis, 1988; Silverberg, 1990; Vogl et al., 2012; Wust, 1986). The complex is subdivided into three units—the Middle plate, the Lower plate, and the Pioneer Intrusive Suite (Fig. 1; Vogl et al., 2012). The gneissose core of the PCC comprises the Lower plate, and consists of Precambrian (~2 Ga) paragneisses and orthogneisses. The Middle plate, also defined as Hyndman Group in Silverberg (1990), is the S/SW part of the PCC that consists of Neoproterozoic (~1.1 Ga) to Ordovician metapelite, quartzite, marble, and calc-silicate rocks. The Eocene Pioneer Intrusive Suite (PIS) emplaced plutonic rock types such as granodiorite, quartz monzonite, diorite, and pyroxenite, between the Middle and Lower plates at ~50-48 Ma during Challis volcanism (Silverberg, 1990).

PREVIOUS RESULTS

Previous studies have used U-Pb, $^{40}Ar/^{39}Ar$, and (U-Th)/He dating techniques to constrain the timing of deformation in the PCC (see Appendix 1; Silverberg, 1990; Vogl et al., 2012, 2014). The Pioneer complex underwent five episodes of deformation according to Silverberg (1990): The oldest deformational event, D1, represents a period

of NE-SW compression but is poorly-preserved due to penetrative D2 compressional deformation. The Late Cretaceous NE-SW D2 event during the Sevier orogeny is poorly-constrained to be pre-79 Ma based on $^{40}Ar/^{39}Ar$ thermochronology of hornblende (Silverberg, 1990). The PCC experienced prograde metamorphism to upper amphibolite-facies P-T conditions during the D2 event (Silverberg, 1990), but both D1 and D2 are extensively overprinted by D3. The region underwent NW-SE-directed extension in Early Eocene (~50-46 Ma) based on zircon U-Pb dating (Vogl et al., 2012). The D3 extensional event was synchronous with Challis volcanism ≥50-45 Ma (Vogl et al., 2012). The PIS was emplaced ~48 Ma based on $^{40}Ar/^{39}Ar$ cooling ages for hornblende (Silverberg, 1990). Garnet-biotite thermobarometry gave peak metamorphism in upper amphibolite-facies at >687°C and 3.6 kbar (Silverberg, 1990). The PCC underwent retrograde metamorphism during exhumation at c. 45 Ma at greenschist-facies at 567°C, 2.4 kbar (Silverberg, 1990). The Hyndman Shear Zone developed during D3 and separates the Middle plate from the PIS. Late Eocene $^{40}Ar/^{39}Ar$ cooling ages of 38-33 Ma were interpreted to record the D4 NW-SE extension (Silverberg, 1990). The Wildhorse Detachment fault system and White Mountains normal fault developed during D4. Vogl et al. (2012) noted that it was unclear whether that Eocene extensional event was continuous over the 17 Ma period from 50 to 33 Ma or took place in two, distinct stages by a similar mechanism. The PCC experienced rapid exhumation in the Miocene and reached a maximum rate of ~0.3 mm/a from 11 to 8 Ma base on apatite (U-Th)/He dating

(Vogl et al., 2014). This later D5 NE-SW-directed extensional deformation has continued since the Miocene and comprises the final structural overprint on PCC rocks.

My project investigates the pressure-temperature-time-deformation (P-T-t-d) history of the Pioneer Core Complex in the context of regional tectonic events, and better constrains the timing of Sevier compression (corresponding to D1 and D2) and Early Eocene extension and magmatism in the PCC (corresponding to D3), by applying zircon geochronology, Ti thermometry and thermodynamic modeling. My geochronology data supports the "slab window" model proposed by Schmandt and Humphreys (2011) that explains the mechanism of Challis magmatism and extension in northern MCCs in Early Eocene and initiation of magmatism in Basin-and-Range in Late Eocene to Miocene.

METHODS

I completed field work including structural measurements and sample collection in summer 2015. Structural data of foliation and fold axis hinge line data were collected on gneiss and deformed monzonite in Wildhorse Creek and Kane Creek in the Lower plate, and on phyllite and foliated quartzite on the E Fork Wood River along the boundary between the Middle plate and sedimentary rocks bounding the PCC. I collected samples for thin sectioning, thermodynamic modeling, zircon U-Pb dating, and Ti-in-zircon and Ti-in-biotite thermometry that are summarized in Table 1.

Perple_X thermodynamic modeling

Eight samples (PC-1, -2, -3, -8, -10, -21, -50, -51) were sent to the WSU GeoAnalytical Lab for whole-rock chemistry analysis using XRF and ICP-MS. Samples included four gneisses (PC-1, -2, -3, -21), two andalusite phyllites (PC-8 and -10), one quartzite (PC-50), and one phyllite (PC-51). I generated isochemical phase equilibria diagrams (i.e., pseudosections) based on the whole-rock chemistry data of each of these samples using Perple_X 6.7.0, a computer program for thermodynamic modeling of mineral equilibria that incorporates mineral chemistry and experimental data. Pseudosections were calculated in the Na_2O-CaO-K_2O-FeO-MgO-Al_2O_3-SiO_2-H_2O-TiO_2-O_2 (NCKFMASHTO) system. Solution phases were clinoamphibole (cAmph(DP2), Diener et al., 2007); white mica (Mica(CHA), Auzanneau et al., 2009); biotite (Bio(TCC), Tajčmanová et al., 2009); garnet (Gt(WPH), White et al., 2000); plagioclase (Pl(h), Newton et al., 1980); chlorite (Chl(HP), Holland et al., 1998); clinopyroxene (Omph(GHP2), Green et al., 2007); ilmenite (IlGkPy, Andersen and Lindsley, 1988); and cordierite (hCrd, Holland and Powell, 1998). Rocks were modeled over a P-T range of 0-7 kbar and 300-1300°C (573-1573°K). Selected pseudosections (PC-1, -2, -3, -10, -21) were combined with Ti-in-biotite and Ti-in-zircon thermometry data and zircon U-Pb dating results to model the complete P-T-t-d history of the PCC.

Zircon U-Pb dating

The crystallization ages of the youngest (outer) zircon rims were determined by U-Pb depth-profiling on the SHRIMP-RG ion microprobe co-operated by the U.S. Geological Survey and Stanford University in the SUMAC facility at Stanford University between 10/12/2015 and 10/13/2015. Six samples (PC-1, -2, -3, -21, -22, -50) were analyzed: this included four gneisses (PC-1, -2, -3, -21), one granitic dike (PC-22), and one quartzite (PC-50). Zircons from the selected samples were concentrated by standard heavy mineral separation processes at Isotope Geology Laboratory at Boise State University. They were co-mounted with a standard Temora-2 (416.8 Ma, (Black et al., 2004) and an in-house compositional standard (MADDER) at SHRIMP lab at Stanford. Standard zircons were pressed into soft indium metal held in a 25 mm diameter by 4 mm think aluminum disk, which was ground and polished to a 1 micron finish. Sample zircons were hand selected and mounted on glass slides coated in thin (<10 microns) film of vacuum grease in ca. 1 x 6 mm rows with the flat euhedral zircon surfaces (m-face) oriented down, against the glass. Oriented zircons grains were pressed into the pre-polished indium, exposing flat non-polished zircon surfaces to be exposed parallel to the mount surface and standard grains. One mount (ML66) was created and zircon U-Pb ages were measured over one two-day session. The mounted grains were submerged in acetone to remove mounting grease, scrubbed with soap and water, and rinsed in dilute ethylenediaminetetraacetic (EDTA) acid and distilled water, dried in a vacuum oven, and coated with Au. The mount was stored at high pressure (10^{-7} torr) for several hours before

being moved into the source chamber of the SHRIMP-RG to minimize degassing of the epoxy and isobaric hydride interferences and masses 204-208. Secondary ions were generated from the target spot with an O_2^- primary ion beam varying in intensity from 2.5 to 3.5 nA. The typically primary ion beam was defocused to achieve a spot diameter between 20-25 microns and a depth of ~2-4 microns. The Au was removed from the sample surface by pre-sputtering the primary beam for 30 seconds before data is collected. Measurements were made at mass resolutions of $M/\Delta M$ = 8000-8500 (10% peak height), which eliminated interfering molecular species. The acquisition routine included high mass normalizing species ($^{90}Zr_2{}^{16}O^+$), followed by $^{180}Hf^{16}O^+$, $^{204}Pb^+$, a background measured at 0.046 AMU above the $^{204}Pb^+$ peak, $^{206}Pb^+$, $^{207}Pb^+$, $^{208}Pb^+$, $^{238}U^+$, $^{232}Th^{16}O^+$, and $^{238}U^{16}O^+$. All peaks were measured on a single EPT® discrete-dynode electron multiplier operated in pulse counting mode. Each mass was counted for 2, 1, 2, 10, 20, 10, 1, 5, 2, 4 seconds, respectively, with an emphasis placed on measuring ^{206}Pb, ^{207}Pb, and ^{238}U. Because the U-Th concentration and age can change as the analysis depth profiles deeper into the crystal with time, we attempted to analyze ^{206}Pb and ^{238}U as close together in time as possible to avoid mixing different domains. All analyses were performed with 7 scans by peak-hopping from mass 195.8 through 254. The primary focus was to measure ages from metamorphic zircon rims, which can be less than 2 μm thick, based on the cross-sectional cathodoluminescence images of polished zircon crystals. Therefore, for individual analyses for which the age increased more than ca. 20 Ma over the 7 cycles of data acquisition (i.e., depth profiling into an older age domain

with depth), only the youngest 2, 3, 4 or 5 cycles were used to calculate model ages. U-Pb ages by SIMS were calculated relative to age standards, and were reliant upon the assumption that the standards were treated in the same manner as the samples. Therefore, the data was reduced using two methods: (1) the U-Pb calibration constant was calculated using 7 cycles of Temora-2 data for unknown analyses that yielded Tertiary ages from 6 or 7 cycles, or (2), for analyses in which only 4 or 5 cycles of Tertiary ages, the U-Pb calibration constant was calculated using 5 cycles of Temora-2 data, or (3) for analyses in which only 2 or 3 cycles of Tertiary ages, the U-Pb calibration constant was calculated using 3 cycles of Temora-2 data. Zircon concentration data for Hf, U, and Th were standardized against well-characterized, homogeneous in-house zircon standards MADDER (3435 ppm U, calculated relative to MAD-green, (Barth and Wooden, 2010)). Calculated model ages for zircon are standardized relative to Temora-2, which were analyzed repeatedly throughout the duration of the analytical session (every 4^{th} analysis). Data reduction for geochronology followed the methods described by (Williams, 1997), and (Ireland and Williams, 2003), and used the MS Excel add-in programs Squid2.51 and Isoplot3.76 of (Ludwig, 2003, 2009). The measured $^{206}Pb/^{238}U$ was corrected for common Pb using ^{207}Pb, which was based on a model Pb composition from (Stacey and Kramers, 1975). All reported $^{206}Pb/^{238}U$ and $^{207}Pb/^{206}Pb$ model ages and uncertainties (2σ) include error summed in quadrature from the external reproducibility (1σ SD) of the standard Temora-2 during an individual analytical session (16-24 hours).

Ti-in-zircon and Ti-in-biotite thermometry

The Ti contents of zircon and biotite were measured on the Cameca SX 100 electron microprobe (EMP) at the U.S. Geological Survey in Menlo Park, CA, on 3/22/2016 and 3/31/2016 for Ti-in-zircon and -biotite thermometry; Ti-in-quartz analyses were performed but Ti contents were below the detectable limits of the electron microprobe. Five samples (PC-1, -2, -3, -10, -21) were analyzed, including four gneisses (PC-1, -2, -3, -21), and one andalusite phyllite (PC-10). Six thin sections made from the five samples were cleaned with ethanol and coated with 18-20-nm of C in the Electron Microscopy Facility at San Francisco State University. Synthetic zircon and biotite were used as standards on the EMP. Analyses were conducted with a focused beam at 15 kV accelerating potential and a sample current of 100 nA (Hayden et al., 2007). Zircons and biotites were analyzed for ZrO_2, SiO_2, TiO_2, Al_2O_3, FeO, MnO, MgO, CaO, Na_2O, K_2O, Cl, and Cr_2O_3 contents.

Ti is considered as an immobile element that primarily or entirely substitutes for Si in zircon when the grain crystallizes at different temperatures. The Ti content of zircon coexisting with rutile or other Ti-rich phases is strongly dependent on temperature (Ferry and Watson, 2007). Thus, I could use Ti content and activities of SiO_2 and TiO_2 to calculate the crystallization temperature of zircon following the equation of Ferry and Watson (2007):

$$\text{Log(ppm Ti-in-zircon)} = 5.711 - 4800/T(K) - \log a_{SiO2} + \log a_{TiO2}$$

where a_{SiO2} and a_{TiO2} are the activities of SiO_2 and TiO_2. Because quartz and rutile are present in all samples, samples may be considered saturated in SiO_2 and TiO_2, thus it is reasonable to assume $a_{SiO2} = a_{TiO2} = 1$.

As biotite is growing, Ti substitutes for Si or Al along with Mg-Fe exchange. The Ti substitution is dependent on temperature, pressure, biotite crystal chemistry and coexisting mineral assemblages, and temperature is most influential (Henry et al., 2005; Henry and Guidotti, 2002). Thus, the crystallization temperature of biotite could be determined by measuring Ti and Mg concentrations.

PCC samples meet most of the criteria for Ti-in-biotite thermometry presented by Henry et al. (2005): Samples should contain (1) ilmenite or rutile, (2) graphite, (3) quartz, and (4) aluminous minerals such as staurolite, cordierite or the Al_2SiO_5 polymorphs; (5) be in the pressure range of 4-6 kbar; and (6) biotite compositions should be in the range X_{Mg} = 0.275-1.0 and Ti = 0.04-0.6. All of the criteria were satisfied except that no graphite was observed in my samples or noted in previous studies.

Crystallization temperatures for biotite were calculated following Henry et al. (2005):

$$T(°C) = \{[\ln(X_{Ti\text{-}in\text{-}biotite}) - a - c(X_{Mg})^3]/b\}^{0.33333}$$

where X_{Mg} is Mg/(Mg + Fe), and a, b and c are parameters -2.3594, 4.6482e-9, and -1.7283, respectively.

SAMPLE DESCRIPTIONS

I describe the general lithologies of each of the PCC units below; mineral abbreviations are from Whitney and Evans (2010).

Lower plate

The Lower plate in the PCC consists of paragneisses and orthogneisses with granitic and leucogranitic dikes (Figs. 3a-j). The gneisses are well- to weakly-foliated and folded (Figs. 3a, f, and g). Chevron folds were observed in paragneiss (float) in Wildhorse Creek (Fig. 3a), consistent with Silverberg's (1990) interpretation that folds in the Lower plate are mainly tight to isoclinal due to D2 Sevier compression. Enclaves of paragneiss and calc-silicate are present in granite (Fig. 3d). Leucogranitic dikes intruded paragneisses and calc-silicates (Fig. 3e). Weakly-foliated biotite-quartz monzonite shows compositional banding. Conjugate fractures in calc-silicates are orientated at 169°, 32° NE and 122°, 78° NE (see stereonets in Figs. 2 and 3c), and they intersect at an acute angle of 58°, may suggesting a NE-SW-directed compressional stress, which is consistent with Silverberg's (1990) interpretation of D2 compression.

Mafic boudinage was observed in orthogneiss (float) in Kane Creek (Fig. 3h). A mafic boudin of paragneiss in orthogneiss (float) shows deformed veins after fracturing (Fig. 3i). These structures were most likely formed during D3 extensional shear stress.

Structural data were collected on gneisses and monzonite in Wildhorse Creek and Kane Creek (Fig. 2). The Lower plate is dome-shaped with a doubly-plunging anticlinal axis trending NW-SE (Fig. 2; Vogl et al., 2012). The foliation in the gneiss and banded

texture of monzonite in Wildhorse Creek is generally more shallowly-dipping on the east flank of the Lower plate (Fig. 2).

Quartzofeldspathic gneisses (PC-1, -2, -3, and -21)

PC-1, -2, -3 and -21 have a poorly-defined S1 foliation; mineral assemblages in this gneiss includes Qz + Mc + Bt + Pl + Ser + Chl + Zrn + Ap + Rt. Inclusions of quartz and feldspar are common in zircon and biotite (Fig. 4a). Some of the biotite grains show a zoning texture petrographically in thin section (Fig. 4a). Chlorite is observed as an alteration product of biotite because of retrogression at low temperature (Fig. 4b). Fine-grained sericite replaces plagioclase, and indicates retrogression at 300-400°C (Fig. 4c; Passchier and Trouw, 1996). Some quartz grains have microtextures including undulose extinction, a chessboard texture, subgrain rotation, bulging recrystallized grain boundaries, and the development of myrmekite (Fig. 4d); these textures suggest these samples have been recrystallized during retrogression at temperatures from >700°C to 300°C (Passchier and Trouw, 1996). Some quartz and feldspar grains show exsolution lamellae (Figs. 4e-h). Perthite is commonly observed in feldspar (Figs. f-h). One perthitic microcline grain contains plagioclase recrystallized in a fish-shape between microcline cleavage planes that resembles S-C fabrics may indicating shear stress during D3 extension parallel to the cleavage (Figs. 4g-h). Fluid inclusions are commonly found in quartz and feldspar that suggest fracturing and healing were post-kinematic of D3 extension at least, probably syn-kinematic with respect to D5 exhumation. Additionally,

Silverberg (1990) identifies titanite in gneisses and a mineral assemblage for the schist from the Lower plate as Grt + Hbl + Bt + Qz + Pl + Zrn + Ap + Sil + Chl + Crd + Ttn.

Granitic dike (PC-22)

The PC-22 dike is an undeformed leucogranite that cross-cuts the foliation in its host gneiss. The dike's mineral assemblage is Qz + Fsp + Bt + Zrn + Ap.

Middle plate

The Middle plate mainly consists of metapelites, such as phyllite, schist, foliated quartzite, and massive marble (Fig. 2). In E Fork Wood River area of the complex, andalusite phyllite is along the boundary of the PCC (Fig. 3j). Porphyroblasts of andalusite have a square-shaped cross-section (Fig. 3j). Further north along the river, granitic dikes cut through dioritic gneiss, and epidote-rich calc-silicates are present in scree on steep slopes beneath cliffs. Quartzite layers are isoclinally-folded (Fig. 3k).

Andalusite phyllite (PC-8 and -10) and phyllite (PC-51)

Phyllites have a mineral assemblage of Bt + Ms + Qz + Pl + Ksp + Ap + Chl + And + Ser + Sil + Zrn. PC-8, -10 and -51 display a well-developed foliation (S1) defined by Qz + Ms + Bt ± And porphyroblasts (Figs. 4i-l). Some biotite grains were altered to chlorite. In PC-8 and -10, andalusite prophyroblasts have a poikiloblastic texture with inclusions of Qz + Bt + Ms (Figs. 4i and j). One andalusite prophyroblast shows distinct

curvature of aligned inclusions (Fig. 4j). Some parts of the andalusite are sericitized (Fig. 4k). Pressure shadows at both sides of andalusite are composed of mostly quartz and minor biotite and muscovite (Fig. 4i). The presence of pressure shadows and aligned inclusions suggest that the growth of andalusite was pre- to syn-kinematic with respect to D3 extensional deformation. Some andalusite prophyroblasts have fractures that created syntaxial veins (Fig. 4k); the fibrous minerals in the vein (quartz and sericite) are the same as walls and show a medial line indicating the fibers were growing inward from the wall toward the center of the vein from both sides. Sericite fibres in the vein suggest the vein developed after andalusite sericitized, indicating it was syn- to post-kinematically developed with respect to low temperature retrogression during D4 extension. Andalusite is absent in PC-51. Fibrous sillimanite grew in biotite during D3 extension at relatively high grade conditions (Fig. 4l). Silverberg (1990) also described Hbl + Bt + Qz + Pl + Ms + Grt + Ksp + Chl + Ilm + Crd + Rt + Ttn + Sil + And + Ap + Hc + Ep in schist in the Middle plate.

Quartzite (PC-50)

The foliated quartzite has a mineral assemblage of Qz + Bt + Ksp + Pl + Zrn + Ap + Chl + Ilm. Biotite grains are aligned in two directions: one is parallel to the foliation (S1) and the other one is at ~30° to the foliation (S2; Fig. 4m). Some biotites appear zoned petrographically, and chlorite replaces biotite. Some quartz grains show undulose extinction, chessboard texture and grain boundary migration, subgrain rotation, and

bulging recrystallization on grain boundaries. Long axes of elongate quartz are parallel to the biotite-defined alignment comprising the S2 foliation. The S2 alignment was probably formed by D3 Early Eocene extension. Aligned fluid inclusions in quartz and feldspar continue undeformed across grain boundaries (Fig. 4n), suggesting they were post-kinematic with respect to D3 extension, most likely syn-kinematic with respect to D5 exhumation.

ANALYTICAL RESULTS

Zircon U-Pb ages

A total of 48 zircons from six samples were dated at the Stanford-USGS SHRIMP-RG Lab: four gneisses (PC-1, -2, -3 and -21), one granitic dike (PC-22) and one foliated quartzite (PC-50). Zircon ages are summarized in Table 3, and Tera-Wasserburg concordia diagrams are shown in Fig. 5. Three zircons from PC-1 and -21 generated ages in the Late Cretaceous; one analysis was concordant at 83.9 ± 5 Ma (PC-1), and the other two were discordant at 85.6 ± 1 Ma and 109 ± 4 Ma (PC-21). The remaining zircons yielded Early Eocene ages. Six out of eight zircon ages from PC-1 were concordant; the younger group including three discordant analyses generated an intercept age of 44.9 ± 0.8 Ma; the older group including five concordant analyses yielded a weighted mean age of 52.4 ± 2.7 Ma (Figs. 5a-c). Out of eight analyses from PC-2 that generated intercept ages of 44.8 ± 1.6 Ma and 51.9 ± 1.1 Ma, three ages were concordant (Figs. 5d-f). Two analyses from PC-3 were discordant, yielding an intercept

age of 58 ± 14 Ma (Fig. 5g). Ages from PC-3 were excluded from further interpretation due to the large error. Eleven out of fourteen analyses for PC-21 zircons were concordant and gave intercept ages of 47.4 ± 0.7 Ma and 51.5 ± 0.8 Ma, respectively (Figs. 5h-j). One age of 61.7 ± 16 Ma from PC-21 was excluded because the error was too high; the youngest age was discordant at 44.2 ± 1.1 Ma. Three out of nine analyses from PC-22 were concordant; the oldest age was discordant at 51.5 ± 2 Ma; the rest of zircons yielded intercept ages of 43.2 ± 3.8 Ma and 47.1 ± 1.1 Ma, respectively (Figs. 5l-m). Two analyses from PC-50 were concordant that generated a weighted mean age of 51.4 ± 6.0 Ma (Fig. 5n).

Ti-in-zircon and Ti-in-biotite thermometry

Eight zircons from three gneisses (PC-1, -2 and -3) from the Lower plate were analyzed for Ti concentrations, and the calculated crystallization temperatures of zircons are summarized in Appendix II. One zircon from PC-1, six zircons from PC-2, and two zircons from PC-3 yielded average temperatures of 1,162°C, 1,038°C and 1,083°C, respectively. The average of all nine zircons was 1061°C.

A total of 207 biotite grains from four gneisses (PC-1, -2, -3 and -21) and one andalusite phyllite (PC-10) were analyzed, and the crystallization temperatures are resented in Appendix III. In the PC-1 gneiss sample, biotite temperatures ranged from 680°C to 722°C, and averaged 704°C. In PC-2 gneiss, biotite yielded temperatures ranging 650°-713°C. and the average was 676°C. In PC-3 gneiss, biotite grains yielded

temperatures from 487°C to 718°C, and one grain gave the highest temperature of 895°C. In PC-21 gneiss, biotite temperatures ranged from 608°C to 712°C. In PC-10 andalusite phyllite, temperatures of biotite ranged from 575°C to 653°C with an average of 590°C, and one grain yielded the highest temperature of 858°C.

DISCUSSION

Zircon U-Pb ages

U-Pb SHRIMP ages for zircons ranged from Late Cretaceous to Early Eocene. One zircon in sample PC-21 gneiss from the Lower plate gave an age of 109 ± 4 Ma, which may indicate D1 compression was ongoing by 109 Ma. Two zircons, each from PC-1 and PC-21 gneisses, generated ages of 83.9 ± 5 Ma and 85.6 ± 1 Ma, respectively. These ages are consistent with Silverberg's (1990) interpretation of pre-79 Ma D2 Sevier compression. Metamorphic suture zone rocks of the Seven Devils Arc terrane, which is west of the Idaho Batholith, gave $^{40}Ar/^{39}Ar$ cooling ages of ~82 Ma (Lund and Snee, 1988; Silverberg, 1990). Granodiorites, quartz diorites and tonalites from the Idaho Batholith yielded zircon U-Pb ages were dated between 98 and 82 Ma (Bennett and Knowles, 1985; Silverberg, 1990; Foster and Fanning, 1997; Foster et al., 2001; Gaschnig et al., 2010, 2011; Dumitru et al., 2013). The rocks in the Albion Mountains to the south of the PCC yielded $^{40}Ar/^{39}Ar$ cooling ages from 90 to 67 Ma (Silverberg, 1990; Hoisch et al., 2002). Thus, D2 Sevier compression of the PCC likely began before 86 Ma to 84 Ma. The Th/U ratio of zircons suggests that zircon yielding an age of 109 Ma was

igneous origin and zircons yielding ages of 85.6 Ma and 83.9 Ma were metamorphic origin. This supports the interpretation that they constrain two episodes of Sevier compression in the PCC. However, because of the limited Cretaceous data (3 zircon ages) and the lack of data between 109 Ma and ~86-84 Ma, further constraining the timing of D1 and D2 will require additional geochronology to determine the timing of D1, and whether D1 and D2 are truly separate tectonic events.

In the Lower plate, zircon ages fall into 2 groups at 44-43 Ma and 52-51 Ma. Zircons from PC-1 gneiss yield an intercept age of 44.9 ± 0.8 Ma and a weighted mean age of 52.4 ± 2.7 Ma (Figs. 5b and c). Zircons from PC-2 gneiss generated intercept ages of 44.8 ± 1.6 Ma and 51.9 ± 1.1 Ma (Figs. 5e and f). PC-21 gneiss generated a young age of 44.2 ± 1.1 Ma and an intercept age of 51.5 ± 0.8 Ma (Figs. 5h-j). PC-22 granitic dike yielded an intercept age of 43.2 ± 3.8 Ma and an oldest age of 51.5 ± 2 Ma (Figs. 5k and l). These age groupings suggest that D3 extension and magmatism was ongoing 52 Ma and ceased by ~43 Ma. This is consistent with the interpretation in Vogl et al. (2012) that stated D3 took place 50-46 Ma, but my data suggest D3 lasted from 52 Ma to 43 Ma that is consistent with Dumitru's (2013) interpretation of Challis magmatism at 51-43 Ma. In the Middle plate, zircons from PC-50 foliated quartzite yielded a weighted mean age of 51.4 ± 6.0 Ma, which further supports D3 starting 52 Ma.

Zircons from PC-21 and PC-22 yielded intercept ages of 47.4 ± 0.7 Ma and 47.1 ± 1.1 Ma, respectively (Figs. 5i and m). These ages of ~47 Ma are consistent with Silverberg's (1990) interpretation of the emplacement of PIS (intrusive granodiorite) at

48 Ma, and supports Dumitru's (2013) interpretation that Challis magmatism peaked at 47 Ma.

Ti-in-zircon and Ti-in-biotite thermometry

Average zircon crystallization temperature from gneisses (PC-1, -2, and -3) is 1061°C (Appendix II; Fig. 6a), assuming $a_{SiO2} = a_{TiO2} = 1$ which sets these temperatures as minimum temperatures. I interpret these zircons to have crystallized at peak metamorphic temperature during magma intrusion associated with D3. These temperatures indicate the late-stage crystallization temperature of zircon was around 1060°C (Hiess et al., 2008). These temperatures are much higher than the peak temperature of 687°C based on garnet-biotite thermobarometry in Silverberg (1990) and the highest biotite temperature of 895°C based on Ti-in-biotite thermometry from the same samples of gneiss in my study. Therefore, I did not consider these zircon temperatures in my thermodynamic modeling.

Biotite crystallization temperatures range from 487°C to 895°C for all analyzed grains (Appendix III; Fig. 6b). Zoned biotite in PC-3 gneiss yielded temperatures of 895°C and 690°C from core to rim, suggesting the grain may record peak temperature of 895°C and retrograded path to temperature of 690°C, or this outlier temperature of 895°C may simply demonstrate a lack of chemical equilibrium in the rock based on a mismatch of temperature range constrained by isopleths of X(Mg) and that constrained by Ti-in-biotite thermometry (Appendix IV-d). Unzoned biotites in all samples yielded

temperatures ranging from 487°C to 858°C, a much larger temperature range than for zoned biotite. In PC-3 gneiss, biotite temperatures range from 487° to 718°C, with a single high value of 895°C. The temperature of 895°C was possibly due to unequilibrium of the rock, so biotite temperatures may suggest PC-3 prograded to >700°C and then retrograded down to ~500°C. In PC-21 gneiss, calculated biotite temperatures are 608°C-712°C; it may suggest PC-21 prograded to ~700°C, followed by retrogression to ~600°C. Biotite temperatures from PC-1 and -2 gneisses yielded averages of 704°C, and 676°C, respectively. Because PC-1, -2, -3 and -21 are from the same unit, the temperatures of ~700°C may suggest the minimum peak temperature of gneisses in the Lower plate. In PC-10 andalusite phyllite, biotite temperatures yielded an average of 590°C and one high value of 858°C (Appendix III; Fig. 6b); it may suggest PC-10 prograded to peak temperature of 858°C and then retrograded down to ~590°C. Temperatures from four samples of gneisses suggest that peak temperature of biotite was probably >700°C and retrograded to ~500°C (Appendix III; Fig. 6b). This interpretation of peak temperature at >700°C from gneiss is close to Silverberg's (1990) interpretation of peak temperature at 687°C yielded from garnet-biotite thermobarometry from schist. But the final equilibrian temperature at ~500°C in this study is lower than 567°C indicated by garnet-biotite thermobarometry in Silverberg (1990). Biotites from andalusite phyllite yielded peak temperature at ~860°C, which is much higher than Silverberg's (1990) interpretation of 687°C. Due to the limited biotite temperatures at the range of >800°C (only one biotite temperature), the interpretation of peak temperature at 860°C is less reliable. However,

the final equilibrium temperature at 590°C from andalusite phyllite is consistent with Silverberg's (1990) interpretation of 567°C.

Thermodynamic modeling

Pseudosections of samples PC-1, -2, -3, -10 and -21 were generated using *Perple_X* for a pressure-temperature ranges of 0-7 kbar and 300-1300°C (Connolly and Petrini, 2002).

The general mineral assemblages for gneisses (PC-1, -2, -3, and -21) are identified as Qtz + Mc + Bt + Pl + Zrn + Ap + Rt + Chl + Ser + Ttn, and that of phyllite (PC-10) is Qz + Ms + Bt + And + Pl + Ksp + Chl + Ser + Sil + Ap. The P-T-t-d paths are compiled with temperature constraints from biotite in corresponding samples, and pressure constraint of 2-4.2 kbar inferred from Silverberg (1990). The relationships between mineral crystallization, overprinting and break-down reactions, and multiple (peak and retrograde) and metamorphic and tectonic deformation events (Fig. 7) were used to interpret the pseudosections and to generate a P-T-t-d path (Fig. 8).

Plotted isopleths of X(Mg) for biotite on pseudosections of gneisses (PC-1, -2, -3 and -21), lie in temperature ranges outside the temperature range constrained by Ti-in-biotite thermometry (Appendix IV). In PC-1 and -21, Mg concentrations for biotite plot above temperatures of 900°C (Appendix IV-b and -e). In PC-2 and -3, X(Mg) isopleths lie in temperatures lower than 500°C; and less than 450°C in the pressure range of 2-4.2 kbar (Appendix IV-c and -d). This mismatch of Mg concentration data for biotite and

calculated Ti-in-biotite temperatures in all four gneisses suggest that the gneisses probably did not reach equilibrium between biotite and the bulk gneiss. In the andalusite phyllite (PC-10), X(Mg) isopleths lie in a temperature range of ~450°C-950°C (Appendix IV-a). Ti temperatures of 575°C-653°C and 858°C fell in the temperature range constrained by Mg concentration data, suggesting the sample reached equilibrium (Appendix IV-a). So I used PC-10 andalusite phyllite to estimate the P-T-t-d history of the PCC.

The P-T-t-d path of an andalusite phyllite follows a clockwise path (Fig. 8). Deformation events D1 and D2 in the Late Cretaceous are considered to be a prograde phase of the PCC evolution at c. 109 Ma and 86-84 Ma, but P-T conditions are uncertain. The beginning of the D3 Early Eocene extension and Challis magmatism also took place during prograde processes at 52-47 Ma. The pre- to syn-kinematic growth of andalusite and syn-kinematic growth of sillimanite with respect to D3 suggest that the metamorphism prograded from andalusite field to sillimanite field en route to reaching peak temperature conditions (Figs. 4i, j and l). At c. 47 Ma, metamorphism reached peak conditions at ~860°C, 4 kbar, corresponding to the intrusion of the PIS during D3 (Silverberg, 1990). Exhumation and retrograde metamorphism of the PCC began at about the same time. We know this from $^{40}Ar/^{39}Ar$ cooling ages of 48 Ma in Silverberg (1990), and zircon U/Pb ages of 47.4 Ma from gneiss (PC-21) and 47.1 Ma from granitic dike (PC-22). The PCC experienced retrogression down to 590°C, 2 kbar at the end of D3 at c. 43 Ma based on Ti-in-biotite thermometry from andalusite phyllite (PC-10) and garnet-

biotite and hornblende thermobarometries in Silverberg (1990). The final stage of M3 retrograde metamorphism took place in the Late Eocene during D4 extension at 38-33 Ma based on $^{40}Ar/^{39}Ar$ cooling ages from Silverberg (1990); late-stage, low-grade P-T conditions for the PCC are not well-constrained, but reached chlorite stability below 500°C (see Fig. 8).

Regional tectonic events during the evolution of the Pioneer Core Complex

The shallow-dipping to flat subduction of the Farallon plate beneath the North American (NA) plate triggered the Sevier-Laramide orogenies that formed the Rocky Mountains in the Cretaceous to early Cenozoic (Bird, 1998; Bunge and Grand, 2000; DeCelles, 2004; DeCelles and Mitra, 1995; DeCelles et al., 1995; Liu et al., 2008; Tikoff and Maxson, 2001). The Sevier orogeny was a "thin-skinned" type of deformation with major décollements in the lower crust to accommodate the magnitude of shortening required in the Sevier thrust front, and the faulting and sediment deposition that follow the critical-taper theory (Armstrong, 1982; Bunge and Grand, 2000; DeCelles and Mitra, 1995; DeCelles, 2004; Dahlen, 1990; Tikoff and Maxson, 2001). In contrast, the Laramide orogeny was a "thick-skinned" type of deformation that required the entire lithosphere to be coupled and the contraction wss accommodated on moderately-dipping thrust faults; décollements were mainly absent during thick-skinned buckling but produced only as secondary structures (Allmendinger and Jordan, 1981; DeCelles et al., 1995; DeCelles and Mitra, 1995; Tikoff and Maxson, 2001). The Sevier orogeny

occurred in what is today the western Rockies in Montana/Idaho/Utah, initiating at 120-100 Ma and continuing to ~80 Ma as the Farallon plate subducted at a shallow angle (Liu et al., 2008; Tikoff and Maxson, 2001). The subducting Farallon plate flattened at 80-75 Ma initiating the Laramide orogeny that pushed the deformation front further inland to the eastern Rockies, east of Sevier thrust front (Bunge and Grand, 2000; Liu et al., 2008; Tikoff and Maxson, 2001; DeCelles, 2004). The Pioneer core complex is located west of the Sevier thrust front (Fig. 1). Both D1 and D2 events comprise NE-SW compression directions in the PCC are dated at c. 109 Ma and pre-86-84 Ma, respectively, consistent with the regional stress orientation and timing of the Sevier orogeny and thin-skinned tectonics. However, because of the lack of geochronology results between 109 Ma and 86 Ma, it is debatable whether D1 and D2 represent one continuous contractional event or two separate deformational episodes on a regional scale.

From the Late Cretaceous to Paleocene-Eocene (~80-50 Ma), the Sevier and Laramide deformation was synchronous through northern Utah to southwest Wyoming (Humphreys, 2009, 1995). At about 55 Ma, a piece of Farallon plate was torn off, creating a micro-oceanic lithospheric plate called Siletzia (Fig. 9; Schmandt and Humphreys, 2011; Gao et al., 2011; Schmandt and Humphreys, 2010). The microplate Siletzia segregated from the Farallon plate and stalled underneath the continent 55-53 Ma west of Idaho within the Columbia Embayment, while the Farallon plate rolled back (Fig. 8). The accretion of Siletzia ceased Laramide compression which finally ended 50 Ma. The roll-back of the Farallon plate opened a slab window under Idaho/western

Montana/northern Washington/southern British Columbia which allowed asthenospheric inflow into the opening mantle wedge, decompression melting of the North American lithosphere and melting of the stalled Farallon crust (Humphreys,1995; 2009; Thorkelson, 1996; Schmandt and Humphreys, 2011). This slab window initiated Challis magmatism and extension in the PCC.

Cordilleran metamorphic core complexes in proximity to the PCC

The initial magmatism related to the northern Cenozoic MCCs (e.g,. the Shuswap and Priest River core complexes) was during the Late Cretaceous to Early Eocene ~100-55 Ma in a Laramide contractional setting (Fig. 1; Haney, 2008; Dumitru et al., 2013; Stevens et al., 2015; Kruckenberg et al., 2008; Foster et al., 2001; Foster and Fanning, 1997; Kruckenberg et al., 2008; Johnson, 2006). Heating due to burial during crustal thickening produced partial melting of the North American crust, which initiated magmatism in the northern MCCs. At 55 Ma, the accreted microplate Siletzia opened a slab window that initiated synchronous Challis magmatism and high-rate extension in the PCC at ~51-43 Ma based on zircon U/Pb ages (Vogl et al., 2012; Schmandt and Humphreys, 2011, 2010; Dumitru et al., 2013). The melting triggered by the Siletzia slab window was concomitant with extension and enhanced magmatism jn the northern MCCs at ~50 Ma (Rey et al., 2009; Whitney et al., 2013; Schmandt and Humphreys, 2011). The slab window also triggered downward buckling of the Farallon plate beneath the southern MCCs in Basin and Range province, initiating magmatism in Basin-and-Range in Late

Eocene to Miocene(Humphreys, 2009, 1995). The rolled-back Farallon plate subducted at a steeper angle and initiated Cascades volcanism at 45-40 Ma (Schmandt and Humphreys, 2011). U-Pb zircon ages from this study indicate D3 extension and Challis volcanism in Pioneer region took place after 52-43 Ma, which is consistent with the formation of the slab window and the initiation of Cascades volcanism. The intrusion of granitoids (the PIS) into the PCC during Challis magmatism gave peak metamorphic temperature in Pioneer c. 47 Ma.

The Cordilleran core complexes north of Pioneer reached peak metamorphism in Late Cretaceous to Paleocene. Based on garnet-biotite thermobarometry and U/Pb geochronology on zircon and monazite, peak metamorphism in Shuswap core complex was at ~6-10 kbar and 620-820°C at c. 80-60 Ma; Priest River core complex reached peak metamorphism at 7-11 kbar and 770-930°C at 86-72 Ma; Bitterroot core complex reached peak metamorphic conditions at 6-8 kbar and 600-750°C at 80-70 Ma; Anaconda core complex reached peak metamorphism at 3.3-5.3 kbar and 590-665°C at 79 Ma (Haney, 2008; Stevens et al., 2015; Kruckenberg et al., 2008; Foster et al., 2001; Foster and Fanning, 1997; Norlander et al., 2002; Johnson, 2006; Vanderhaeghe et al., 2003; Foster et al., 2007). The core complexes south of Pioneer in close proximity, such as Albion-Raft River-Grouse Creek core complexes, Ruby Mountains core complex and Snake Range core complex, reached peak metamorphism in Late Cretaceous based on garnet-biotite thermoborametry and U/Pb geochronology on zircon and monazite; peak metamorphic conditions of Albion-Raft River-Grouse Creek core complexes were ~7

kbar and 575-635°C at c. 120 Ma; Ruby Mountains core complex reached peak metamorphism at ~9 kbar and 800°C at c. 84 Ma; peak metamorphism in Snake Range core complex was at ~8 kbar and >600°C at c. 84 Ma (Sullivan and Snoke, 2007; Cooper et al., 2010; Harris et al., 2007; Konstantinou et al., 2013, 2012; Strickland, Miller, and Wooden, 2011; Strickland, Miller, Wooden, et al., 2011; Hoisch et al., 2002; Kelly et al., 2015). The Pioneer core complex reached peak metamorphism at ~4 kbar and 860°C at c. 47 Ma in Early Eocene. The peak pressure in the PCC was 3.6 kbar based on garnet-biotite and hornblende thermobarometry (Silverberg, 1990), and inferred from Sliverberg (1990) as ~4 kbar in this study. This peak pressure was close to that of Anaconda core complex and it was the lowest peak pressure comparing to other core complexes near the PCC. The decreasing trend in pressure from the Shuswap core complex southward to the Pioneer core complex probably related to the width of the core complexes (Haney, 2008). The peak metamorphic temperature of 687°C of the PCC based on garnet-biotite thermobarometry from Silverberg (1990) was similar to other core complexes. However, the peak temperature of ~860°C based on Ti-in-biotite thermometry in this study was much higher than the other core complexes near the PCC. This may suggest the incredibility of the Ti temperature of 860°C in this study. Further geothermometry will be required to verify the peak metamorphic temperature in Pioneer. The peak metamorphism experienced by other core complexes near the PCC was due to crustal thickening and partial melting by burial during Sevier-Laramide orogeny in contractional setting, while the PCC reached peak metamorphic conditions during Challis magmatism in extensional

setting. The mechanism that produced peak metamorphism in the PCC was different than that in the other core complexes in close proximity.

CONCLUSIONS

The project better constrained two episodes of Sevier compression in the Pioneer core complex based on zircon U-Pb geochronology; D1 was onging by 109 Ma and D2 was c. 86-84 Ma. The Early Eocene extension and Challis magmatism (D3) were synchronous at c. 52-43 Ma based on zircon U-Pb ages in this study. The metamorphic history of the PCC started near the beginning of Sevier orogeny by 109 Ma (corresponding to D1). Progression continued in late-stage Sevier orogeny c. 86-84 Ma (corresponding to D2). In Early Eocene (corresponding to D3), the PCC prograded to peak conditions at ~4 kbar and 860°C at 52-47 Ma. The emplacement of the granitoid PIS gave peak metamorphic temperature of the PCC at c. 47 Ma. Retrogression (corresponding to D3) to ~2 kbar and 590°C immediately followed peak metamorphism at c. 47-43 Ma. In Late Eocene (corresponding to D4, the PCC continued retrogression at 38-33 Ma based on $^{40}Ar/^{39}Ar$ cooling aged from Silverberg (1990). My U-Pb geochronology data from zircons supports the "slab window" model proposed by Schmandt and Humphreys (2011) that the accreted micro-oceanic plate (Siletzia) under the North American lithosphere initiated extension and Challis magmatism in the Pioneer region.

REFERENCES

Allmendinger, R.W., and Jordan, T.E., 1981, Mesozoic evolution, hinterland of the Sevier orogenic belt: Geology, v. 9, p. 308–313, doi: 10.1130/0091-7613(1981)9<308:MEHOTS>2.0.CO;2.

Andersen, D.J., and Lindsley, D.H., 1988, Internally consistent solution models for Fe-Mg-Mn-Ti oxides: Fe-Ti oxides: The American mineralogist, v. 73, p. 714–726.

Armstrong, R.L., 1982, CORDILLERAN METAMORPHIC CORE COMPLEXES - From Arizona to Southern Canada: Annual Review of Earth and Planetary Sciences, v. 10, p. 129, doi: 10.1146/annurev.ea.10.050182.001021.

Auzanneau, E., Schmidt, M.W., Vielzeuf, D., and Connolly, J. a. D., 2009, Titanium in phengite: a geobarometer for high temperature eclogites: Contributions to Mineralogy and Petrology, v. 159, p. 1, doi: 10.1007/s00410-009-0412-7.

Barth, A.P., and Wooden, J.L., 2010, Coupled elemental and isotopic analyses of polygenetic zircons from granitic rocks by ion microprobe, with implications for melt evolution and the sources of granitic magmas: Chemical Geology, v. 277, p. 149–159, doi: 10.1016/j.chemgeo.2010.07.017.

Bennett, E.H., and Knowles, C.R., 1985, Tertiary plutons and related rocks in central Idaho, *in* Symposium on the geology and mineral deposits of the Challis, v. 1, p. 81–95.

Bird, P., 1998, Kinematic history of the Laramide orogeny in latitudes 35o-49oN, western United States: Tectonics, v. 17, p. 780–801.

Black, L.P., Kamo, S.L., Allen, C.M., Davis, D.W., Aleinikoff, J.N., Valley, J.W., Mundil, R., Campbell, I.H., Korsch, R.J., Williams, I.S., and Foudoulis, C., 2004, Improved 206Pb/238U microprobe geochronology by the monitoring of a trace-element-related matrix effect; SHRIMP, ID–TIMS, ELA–ICP–MS and oxygen isotope documentation for a series of zircon standards: Chemical Geology, v. 205, p. 115–140, doi: 10.1016/j.chemgeo.2004.01.003.

Breitsprecher, K., Thorkelson, D.J., Groome, W.G., and Dostal, J., 2003, Geochemical confirmation of the Kula-Farallon slab window beneath the Pacific Northwest in Eocene time: Geology, v. 31, p. 351–354, doi: 10.1130/0091-7613(2003)031<0351:GCOTKF>2.0.CO;2.

Bunge, H.-P., and Grand, S.P., 2000, Mesozoic plate-motion history below the northeast Pacific Ocean from seismic images of the subducted Farallon slab: Nature, v. 405, p. 337–340, doi: 10.1038/35012586.

Connolly, J. a. D., and Petrini, K., 2002, An automated strategy for calculation of phase diagram sections and retrieval of rock properties as a function of physical

conditions: Journal of Metamorphic Geology, v. 20, p. 697–708, doi: 10.1046/j.1525-1314.2002.00398.x.

Cooper, F.J., Platt, J.P., Anczkiewicz, R., and Whitehouse, M.J., 2010, Footwall dip of a core complex detachment fault: thermobarometric constraints from the northern Snake Range (Basin and Range, USA): Journal of Metamorphic Geology, v. 28, p. 997–1020, doi: 10.1111/j.1525-1314.2010.00907.x.

Dahlen, F.A., 1990, Critical taper model of fold-and-thrust belts and accretionary wedges: Annual Review of Earth and Planetary Sciences, v. 18, p. 55.

DeCelles, P.G., 2004, Late Jurassic to Eocene evolution of the Cordilleran thrust belt and foreland basin system, western U.S.A.: American Journal of Science, v. 304, p. 105–168, doi: 10.2475/ajs.304.2.105.

DeCelles, P.G., Lawton, T.F., and Mitra, G., 1995, Thrust timing, growth of structural culminations, and synorogenic sedimentation in the type Sevier orogenic belt, western United States: Geology, v. 23, p. 699–702, doi: 10.1130/0091-7613(1995)023<0699:TTGOSC>2.3.CO;2.

DeCelles, P.G., and Mitra, G., 1995, History of the Sevier orogenic wedge in terms of critical taper models, northeast Utah and southwest Wyoming: Geological Society of America Bulletin, v. 107, p. 454–462, doi: 10.1130/0016-7606(1995)107<0454:HOTSOW>2.3.CO;2.

Diener, J.F.A., Powell, R., White, R.W., and Holland, T.J.B., 2007, A new thermodynamic model for clino- and orthoamphiboles in the system Na2O–CaO–FeO–MgO–Al2O3–SiO2–H2O–O: Journal of Metamorphic Geology, v. 25, p. 631–656, doi: 10.1111/j.1525-1314.2007.00720.x.

Dumitru, T.A., Ernst, W.G., Wright, J.E., Wooden, J.L., Wells, R.E., Farmer, L.P., Kent, A.J.R., and Graham, S.A., 2013, Eocene extension in Idaho generated massive sediment floods into the Franciscan trench and into the Tyee, Great Valley, and Green River basins: Geology, v. 41, p. 187–190, doi: 10.1130/G33746.1.

Durk, K., and Link, P.K., 2007, Geochronology of part of the Wildhorse Gneiss Complex, Pioneer Mountains, Custer County, Idaho:

Ferry, J.M., and Watson, E.B., 2007, New thermodynamic models and revised calibrations for the Ti-in-zircon and Zr-in-rutile thermometers: Contributions to Mineralogy and Petrology, v. 154, p. 429–437, doi: 10.1007/s00410-007-0201-0.

Foster, D.A., Doughty, P.T., Kalakay, T.J., Fanning, C.M., Coyner, S., Grice, W.C., and Vogl, J., 2007, Kinematics and timing of exhumation of metamorphic core complexes along the Lewis and Clark fault zone, northern Rocky Mountains, USA: Geological Society of America Special Papers, v. 434, p. 207–232, doi: 10.1130/2007.2434(10).

Foster, D.A., and Fanning, C.M., 1997, Geochronology of the northern Idaho batholith and the Bitterroot metamorphic core complex: Magmatism preceding and contemporaneous with extension: Geological Society of America Bulletin, v. 109, p. 379–394, doi: 10.1130/0016-7606(1997)109<0379:GOTNIB>2.3.CO;2.

Foster, D.A., Schafer, C., Fanning, C.M., and Hyndman, D.W., 2001, Relationships between crustal partial melting, plutonism, orogeny, and exhumation: Idaho–Bitterroot batholith: Tectonophysics, v. 342, p. 313–350, doi: 10.1016/S0040-1951(01)00169-X.

Gao, H., Humphreys, E.D., Yao, H., and van der Hilst, R.D., 2011, Crust and lithosphere structure of the northwestern U.S. with ambient noise tomography: Terrane accretion and Cascade arc development: Earth and Planetary Science Letters, v. 304, p. 202–211, doi: 10.1016/j.epsl.2011.01.033.

Gaschnig, R.M., Vervoort, J.D., Lewis, R.S., and McClelland, W.C., 2010, Migrating magmatism in the northern US Cordillera: in situ U–Pb geochronology of the Idaho batholith: Contributions to Mineralogy and Petrology, v. 159, p. 863–883, doi: 10.1007/s00410-009-0459-5.

Gaschnig, R.M., Vervoort, J.D., Lewis, R.S., and Tikoff, B., 2011, Isotopic Evolution of the Idaho Batholith and Challis Intrusive Province, Northern US Cordillera: Journal of Petrology, v. 52, p. 2397–2429, doi: 10.1093/petrology/egr050.

Green, E., Holland, T., and Powell, R., 2007, An order-disorder model for omphacitic pyroxenes in the system jadeite-diopsidehedenbergite- acmite, with applications to eclogitic rocks: American Mineralogist, v. 92, p. 1181–1189, doi: 10.2138/am.2007.2401.

Haney, E.M., 2008, Pressure-temperature Evolution of Metapelites Within the Anaconda Metamorphic Core Complex, Southwestern Montana: Citeseer, http://citeseerx.ist.psu.edu/viewdoc/download?doi=10.1.1.510.9990&rep=rep1&type=pdf (accessed December 2016).

Harris, C.R., Hoisch, T.D., and Wells, M.L., 2007, Construction of a composite pressure–temperature path: revealing the synorogenic burial and exhumation history of the Sevier hinterland, USA: Journal of Metamorphic Geology, v. 25, p. 915–934, doi: 10.1111/j.1525-1314.2007.00733.x.

Hayden, L.A., Watson, E.B., and Wark, D.A., 2007, A thermobarometer for sphene (titanite): Contributions to Mineralogy and Petrology, v. 155, p. 529–540, doi: 10.1007/s00410-007-0256-y.

Henry, D.J., and Guidotti, C.V., 2002, Titanium in biotite from metapelitic rocks: Temperature effects, crystal-chemical controls, and petrologic applications: American Mineralogist, v. 87, p. 375–382, doi: 10.2138/am-2002-0401.

Henry, D.J., Guidotti, C.V., and Thomson, J.A., 2005, The Ti-saturation surface for low-to-medium pressure metapelitic biotites: Implications for geothermometry and Ti-substitution mechanisms: American Mineralogist, v. 90, p. 316–328, doi: 10.2138/am.2005.1498.

Hiess, J., Nutman, A.P., Bennett, V.C., and Holden, P., 2008, Ti-in-zircon thermometry applied to contrasting Archean metamorphic and igneous systems: Chemical Geology, v. 247, p. 323–338, doi: 10.1016/j.chemgeo.2007.10.012.

Hoisch, T.D., Wells, M.L., and Hanson, L.M., 2002, Pressure-temperature paths from garnet-zoning: Evidence for multiple episodes of thrust burial in the hinterland of the Sevier orogenic belt: American Mineralogist, v. 87, p. 115–131.

Holland, T., Baker, J., and Powell, R., 1998, Mixing properties and activity-composition relationships of chlorites in the system MgO-FeO-Al2O3-SiO2-H2O: European Journal of Mineralogy, p. 395–406.

Holland, T.J.B., and Powell, R., 1998, An internally consistent thermodynamic data set for phases of petrological interest: Journal of Metamorphic Geology, v. 16, p. 309–343, doi: 10.1111/j.1525-1314.1998.00140.x.

Humphreys, E.D., 1995, Post-Laramide removal of the Farallon slab, western USA: Geology, v. 23, doi: 10.1130/0091-7613(1995)023<0987:PLROTF>2.3.CO;2.

Humphreys, E., 2009, Relation of flat subduction to magmatism and deformation in the western USA: Geological Society of America Memoirs, v. 204, p. 85–98, doi: 10.1130/2009.1204(04).

Ireland, T.R., and Williams, I.S., 2003, Considerations in Zircon Geochronology by SIMS: Reviews in Mineralogy and Geochemistry, v. 53, p. 215–241, doi: 10.2113/0530215.

Janecke, S.U., 1992, Kinematics and timing of three superposed extensional systems, east central Idaho: Evidence for an Eocene tectonic transition: Tectonics, v. 11, p. 1121–1138, doi: 10.1029/92TC00334.

Janecke, S.U., 1994, Sedimentation and paleogeography of an Eocene to Oligocene rift zone, Idaho and Montana: Geological Society of America Bulletin, v. 106, p. 1083–1095, doi: 10.1130/0016-7606(1994)106<1083:SAPOAE>2.3.CO;2.

Johnson, B.J., 2006, Extensional shear zones, granitic melts, and linkage of overstepping normal faults bounding the Shuswap metamorphic core complex, British Columbia: Geological Society of America Bulletin, v. 118, p. 366–382, doi: 10.1130/B25800.1.

Kelly, E.D., Hoisch, T.D., Wells, M.L., Vervoort, J.D., and Beyene, M.A., 2015, An Early Cretaceous garnet pressure–temperature path recording synconvergent

burial and exhumation from the hinterland of the Sevier orogenic belt, Albion Mountains, Idaho: Contributions to Mineralogy and Petrology, v. 170, p. 20, doi: 10.1007/s00410-015-1171-2.

Konstantinou, A., Strickland, A., Miller, E.L., and Wooden, J.P., 2012, Multistage Cenozoic extension of the Albion–Raft River–Grouse Creek metamorphic core complex: Geochronologic and stratigraphic constraints: Geosphere, p. GES00778.1, doi: 10.1130/GES00778.1.

Konstantinou, A., Valley, J., Strickland, A., Miller, E.L., Fisher, C., Vervoort, J., and Wooden, J., 2013, Geochemistry and geochronology of the Jim Sage volcanic suite, southern Idaho: Implications for Snake River Plain magmatism and its role in the history of Basin and Range extension: Geosphere, v. 9, p. 1681–1703, doi: 10.1130/GES00948.1.

Kruckenberg, S.C., Whitney, D.L., Teyssier, C., Fanning, C.M., and Dunlap, W.J., 2008, Paleocene-Eocene migmatite crystallization, extension, and exhumation in the hinterland of the northern Cordillera: Okanogan dome, Washington, USA: Geological Society of America Bulletin, v. 120, p. 912–929, doi: 10.1130/B26153.1.

Lee Armstrong, R., and Ward, P., 1991, Evolving geographic patterns of Cenozoic magmatism in the North American Cordillera: The temporal and spatial association of magmatism and metamorphic core complexes: Journal of Geophysical Research: Solid Earth, v. 96, p. 13201–13224, doi: 10.1029/91JB00412.

Liu, L., Spasojević, S., and Gurnis, M., 2008, Reconstructing Farallon Plate Subduction Beneath North America Back to the Late Cretaceous: Science, v. 322, p. 934–938, doi: 10.1126/science.1162921.

Ludwig, K.R., 2009, SQUID 2 (rev. 2.50): A User's Manual: Berkeley Geochronology Center. Spec. Pub, v. 5, p. 104p.

Ludwig, K.R., 2003, User's manual for Isoplot 3.00: a geochronological toolkit for Microsoft Excel: Kenneth R. Ludwig, 4.

Lund, K., and Snee, L.W., 1988, Metamorphism, structural development, and age of the continent-island arc juncture in west-central Idaho: Metamorphism and crustal evolution of the western United States, Rubey, v. 3, p. 297–331.

Newton, R.C., Charlu, T.V., and Kleppa, O.J., 1980, Thermochemistry of the high structural state plagioclases: Geochimica et Cosmochimica Acta, v. 44, p. 933–941, doi: 10.1016/0016-7037(80)90283-5.

Norlander, B.H., Whitney, D.L., Teyssier, C., and Vanderhaeghe, O., 2002, Partial melting and decompression of the Thor-Odin dome, Shuswap metamorphic core

complex, Canadian Cordillera: Lithos, v. 61, p. 103–125, doi: 10.1016/S0024-4937(02)00075-0.

O'neill, R.L., and Pavlis, T.L., 1988, Superposition of Cenozoic extension on Mesozoic compressional structures in the Pioneer Mountains metamorphic core complex, central Idaho: Geological Society of America Bulletin, v. 100, p. 1833–1845, doi: 10.1130/0016-7606(1988)100<1833:SOCEOM>2.3.CO;2.

Passchier, C.W., and Trouw, R.A., 1996, Microtectonics: Springer, v. 256, http://link.springer.com/content/pdf/10.1007/3-540-29359-0.pdf (accessed December 2016).

Rey, P.F., Teyssier, C., and Whitney, D.L., 2009, The role of partial melting and extensional strain rates in the development of metamorphic core complexes: Tectonophysics, v. 477, p. 135–144, doi: 10.1016/j.tecto.2009.03.010.

Schmandt, B., and Humphreys, E., 2010, Complex subduction and small-scale convection revealed by body-wave tomography of the western United States upper mantle: Earth and Planetary Science Letters, v. 297, p. 435–445, doi: 10.1016/j.epsl.2010.06.047.

Schmandt, B., and Humphreys, E., 2011, Seismically imaged relict slab from the 55 Ma Siletzia accretion to the northwest United States: Geology, v. 39, p. 175–178, doi: 10.1130/G31558.1.

Silverberg, D.S., 1990, The tectonic evolution of the pioneer metamorphic core complex, south-central Idaho [Thesis]: Massachusetts Institute of Technology, http://dspace.mit.edu/handle/1721.1/17274 (accessed April 2016).

Stacey, J.S., and Kramers, J.D., 1975, Approximation of terrestrial lead isotope evolution by a two-stage model: Earth and Planetary Science Letters, v. 26, p. 207–221, doi: 10.1016/0012-821X(75)90088-6.

Stevens, L.M., Baldwin, J.A., Cottle, J.M., and Kylander-Clark, A.R.C., 2015, Phase equilibria modelling and LASS monazite petrochronology: P–T–t constraints on the evolution of the Priest River core complex, northern Idaho: Journal of Metamorphic Geology, v. 33, p. 385–411, doi: 10.1111/jmg.12125.

Strickland, A., Miller, E.L., and Wooden, J.L., 2011, The Timing of Tertiary Metamorphism and Deformation in the Albion–Raft River–Grouse Creek Metamorphic Core Complex, Utah and Idaho: The Journal of Geology, v. 119, p. 185–206, doi: 10.1086/658294.

Strickland, A., Miller, E.L., Wooden, J.L., Kozdon, R., and Valley, J.W., 2011, Syn-extensional plutonism and peak metamorphism in the Albion–Raft River–Grouse Creek metamorphic core complex: American Journal of Science, v. 311, p. 261–314, doi: 10.2475/04.2011.01.

Sullivan, W.A., and Snoke, A.W., 2007, Comparative anatomy of core-complex development in the northeastern Great Basin, U.S.A.: Rocky Mountain Geology, v. 42, p. 1–29, doi: 10.2113/gsrocky.42.1.1.

Tajčmanová, L., Connolly, J. a. D., and Cesare, B., 2009, A thermodynamic model for titanium and ferric iron solution in biotite: Journal of Metamorphic Geology, v. 27, p. 153–165, doi: 10.1111/j.1525-1314.2009.00812.x.

Thorkelson, D.J., 1996, Subduction of diverging plates and the principles of slab window formation: Tectonophysics, v. 255, p. 47–63, doi: 10.1016/0040-1951(95)00106-9.

Tikoff, B., and Maxson, J., 2001, Lithospheric buckling of the Laramide foreland during Late Cretaceous and Paleogene, western United States: Rocky Mountain Geology, v. 36, p. 13–35, doi: 10.2113/gsrocky.36.1.13.

Vanderhaeghe, O., Teyssier, C., McDougall, I., and Dunlap, W.J., 2003, Cooling and exhumation of the Shuswap Metamorphic Core Complex constrained by 40Ar/39Ar thermochronology: Geological Society of America Bulletin, v. 115, p. 200–216, doi: 10.1130/0016-7606(2003)115<0200:CAEOTS>2.0.CO;2.

Vogl, J.J., Foster, D.A., Fanning, C.M., Kent, K.A., Rodgers, D.W., and Diedesch, T., 2012, Timing of extension in the Pioneer metamorphic core complex with implications for the spatial-temporal pattern of Cenozoic extension and exhumation in the northern U.S. Cordillera: Tectonics, v. 31, p. TC1008, doi: 10.1029/2011TC002981.

Vogl, J.J., Min, K., Carmenate, A., Foster, D.A., and Marsellos, A., 2014, Miocene regional hotspot-related uplift, exhumation, and extension north of the Snake River Plain: Evidence from apatite (U-Th)/He thermochronology: Lithosphere, v. 6, p. 108–123, doi: 10.1130/L308.1.

White, Powell, Holland, and Worley, 2000, The effect of TiO2 and Fe2O3 on metapelitic assemblages at greenschist and amphibolite facies conditions: mineral equilibria calculations in the system K2O–FeO–MgO–Al2O3–SiO2–H2O–TiO2–Fe2O3: Journal of Metamorphic Geology, v. 18, p. 497–511, doi: 10.1046/j.1525-1314.2000.00269.x.

Whitney, D.L., and Evans, B.W., 2010, Abbreviations for names of rock-forming minerals: American mineralogist, v. 95, p. 185.

Whitney, D.L., Teyssier, C., Rey, P., and Buck, W.R., 2013, Continental and oceanic core complexes: Geological Society of America Bulletin, v. 125, p. 273–298, doi: 10.1130/B30754.1.

Williams, I.S., 1997, Th-P geochronology by ion microprobe: not just ages but histories: Reviews in Economic Geology, v. 7, p. 1–35.

Wust, S.L., 1986, Extensional deformation with northwest vergence, Pioneer core complex, central Idaho: Geology, v. 14, p. 712–714, doi: 10.1130/0091-7613(1986)14<712:EDWNVP>2.0.CO;2.

Table 1. PCC sample locations

Sample No.	Rock type	PCC unit	Sample location	Latitude	Longitude
PC-1	Qfp gneiss	Lower plate (gneiss core)	Wildhorse Cr	43.75911 N	114.103483 W
PC-2	Qfp gneiss			43.795275 N	114.094245 W
PC-3	Qfp gneiss			43.792891 N	114.093303 W
PC-21	Qfp gneiss		Kane Lake (in Kane Cr)	43.789836 N	114.156386 W
PC-22	Non-deformed granitic dike			43.787155 N	114.159005 W
PC-8	Andalusite phyllite	Middle plate (metapellite) boundary	E Fork Wood River	43.707483 N	114.090923 W
PC-10	Andalusite phyllite			43.707691 N	114. 092243 W
PC-50	Foliated quartzite			43.707483 N	114.090923 W
PC-51	Phyllite			43.707483 N	114.090923 W

Note: Qfp, quartzofeldspathic.

Table 2. Whole-rock chemistry data for PCC samples.

	PC-1	PC-2	PC-3	PC-8	PC-10	PC-21	PC-50	PC-51
SiO_2	74.28	74.16	74.24	59.16	61.84	73.41	92.43	62.12
TiO_2	0.128	0.105	0.089	0.993	0.993	0.697	0.081	0.896
Al_2O_3	14.49	14.60	14.21	21.19	18.99	9.67	3.23	16.37
FeO_{Tot}	0.96	1.04	1.01	7.44	7.10	7.95	0.58	9.81
MnO	0.016	0.031	0.024	0.116	0.079	0.126	0.011	0.112
MgO	0.24	0.19	0.21	2.37	2.23	0.51	0.91	3.27
CaO	1.42	1.51	1.53	0.80	0.25	1.16	1.31	0.81
Na_2O	4.77	4.87	4.46	1.89	0.67	2.14	0.10	0.78
K_2O	3.26	3.24	3.50	3.10	4.97	3.57	0.44	4.18
P_2O_5	0.034	0.029	0.024	0.100	0.066	0.054	0.037	0.079
Sum	99.61	99.77	99.30	97.15	97.20	99.30	99.12	98.43
LOI %	0.25	0.14	0.13	2.35	2.05	0.13	0.30	1.27

Note: values are in oxide wt%. LOI, loss on ignition.

Table 3. U-Th-Pb zircon data for PCC samples.

Spot	U (ppm)	Th (ppm)	Th/U	M/I	Com ^{206}Pb (%)	$^{238}U/^{206}Pb$	err (%)	$^{207}Pb/^{206}Pb$	err (%)	Corr $^{206}Pb/^{238}U$ age (Ma)	1σ err (Ma)
PC-1 Gneiss											
13.1	1019	41	0.041	M	2.28	140	1.4	0.065	4.0	44.7	0.6
12.1	414	9	0.021	M	1.93	141	1.7	0.062	8.7	44.7	0.8
8.1	2470	39	0.016	M	0.40	141	1.7	0.050	3.6	45.4	0.8
2.1	2189	95	0.043	M	0.39	125	1.3	0.050	2.6	51.1	0.6
1.1	2852	33	0.012	M	0.93	124	1.4	0.054	4.0	51.4	0.7
4.1	2025	77	0.038	M	0.47	124	2.3	0.051	2.1	51.6	1
9.1	1522	39	0.026	M	2.54	116	18.5	0.067	31.5	53.8	10
7.1	546	6	0.010	M	1.13	113	1.4	0.056	8.0	56.0	0.8
3.1	1219	51	0.042	M	3.03	74	5.7	0.072	35.0	83.9	5
PC-2 Gneiss											
4.1	1677	60	0.036	M	0.46	143	2.0	0.051	4.2	44.7	0.9
7.1	324	13	0.039	M	3.88	136	5.1	0.078	10.5	45.4	2
11.1	1678	38	0.023	M	4.80	120	1.2	0.085	3.4	51.0	0.6
12.1	196	54	0.278	I	12.97	109	4.0	0.150	29.1	51.3	4
2.1	1535	61	0.040	M	3.59	117	6.9	0.076	9.4	53.0	4
1.1	187	2	0.013	M	11.73	106	4.1	0.140	6.8	53.5	2
3.1	1311	86	0.066	M	1.56	115	3.2	0.059	2.5	55.1	2
9.1	1441	9	0.006	M	1.06	108	6.3	0.056	8.5	58.5	4
PC-3 Gneiss											
7.1	1358	18	0.013	M	1.46	109	12.9	0.059	3.7	58.1	7
11.1	96	22	0.228	I	7.91	97	33.7	0.110	10.5	61.2	21
PC-21 Gneiss											
16.1	368	105	0.286	I	3.24	140	2.4	0.073	6.1	44.2	1
5.1	353	223	0.634	I	0.86	138	1.4	0.054	7.3	46.3	0.7
21.1	281	137	0.487	I	0.74	136	1.6	0.053	7.4	47.0	0.8
1.1	305	35	0.115	I	12.23	120	2.8	0.144	5.4	47.0	1
18.1	889	125	0.141	I	0.37	135	1.4	0.050	3.8	47.5	0.7
14.1	635	88	0.138	I	-0.20	135	10.6	0.045	5.5	47.7	5
22.1	254	118	0.465	I	4.18	127	2.2	0.080	7.2	48.4	1
15.1	762	121	0.158	I	1.13	130	1.9	0.056	7.9	48.7	1.0
13.1	860	111	0.129	I	0.11	128	1.7	0.048	6.3	50.3	0.9
3.1	287	141	0.491	I	1.02	126	1.6	0.055	5.5	50.6	0.9
4.1	595	155	0.261	I	0.52	126	7.1	0.051	6.2	50.6	4
10.1	430	70	0.163	I	0.22	124	1.7	0.049	5.2	51.7	0.9

17.1	1830	326	0.178	I	0.45	122	1.6	0.051	4.3	52.2	0.8
11.1	366	212	0.578	I	-0.03	122	2.7	0.047	10.6	52.5	1
12.1	253	121	0.480	I	4.12	113	3.6	0.080	7.3	54.3	2
6.1	945	69	0.073	M	0.65	103	26.2	0.052	4.5	61.7	16
8.1	429	39	0.091	M	4.70	71	1.2	0.085	5.7	85.6	1
7.1	600	121	0.202	I	8.44	54	3.0	0.115	11.8	109	4
PC-22 Granitic dike											
1.1	1592	89	0.056	M	45.73	86	13.9	0.409	20.1	40.4	10
6.1	938	46	0.049	M	22.96	119	5.8	0.229	11.5	41.7	3
2.1	1075	126	0.117	I	20.32	117	7.5	0.208	25.3	43.9	5
3.1	3198	279	0.087	M	22.69	112	5.7	0.227	14.8	44.2	3
5.1	2383	76	0.032	M	35.14	92	8.1	0.325	14.8	45.4	6
11.1	3844	184	0.048	M	2.12	136	1.6	0.064	2.5	46.1	0.8
12,1	2453	140	0.057	M	9.86	126	3.9	0.125	21.8	46.1	3
7.1	1784	75	0.042	M	1.10	132	1.6	0.056	7.7	48.2	0.8
4.1	4348	197	0.045	M	4.42	119	2.8	0.082	22.4	51.5	2
PC-50 Quartzite											
9.1	1252	116	0.092	M	0.53	125	6.8	0.051	7.6	51.2	3
1.1	2796	21	0.008	M	0.98	122	10.9	0.055	9.3	52.0	6

Note: M-metamorphic origin; I-igneous origin; Com ^{206}Pb (%)-percent of common ^{206}Pb; err-error; Corr $^{206}Pb/^{238}U$ age (Ma)-calculated $^{206}Pb/^{238}U$ age (Ma) after ^{206}Pb correction. The threshold of M/I origin is Th/U=0.1.

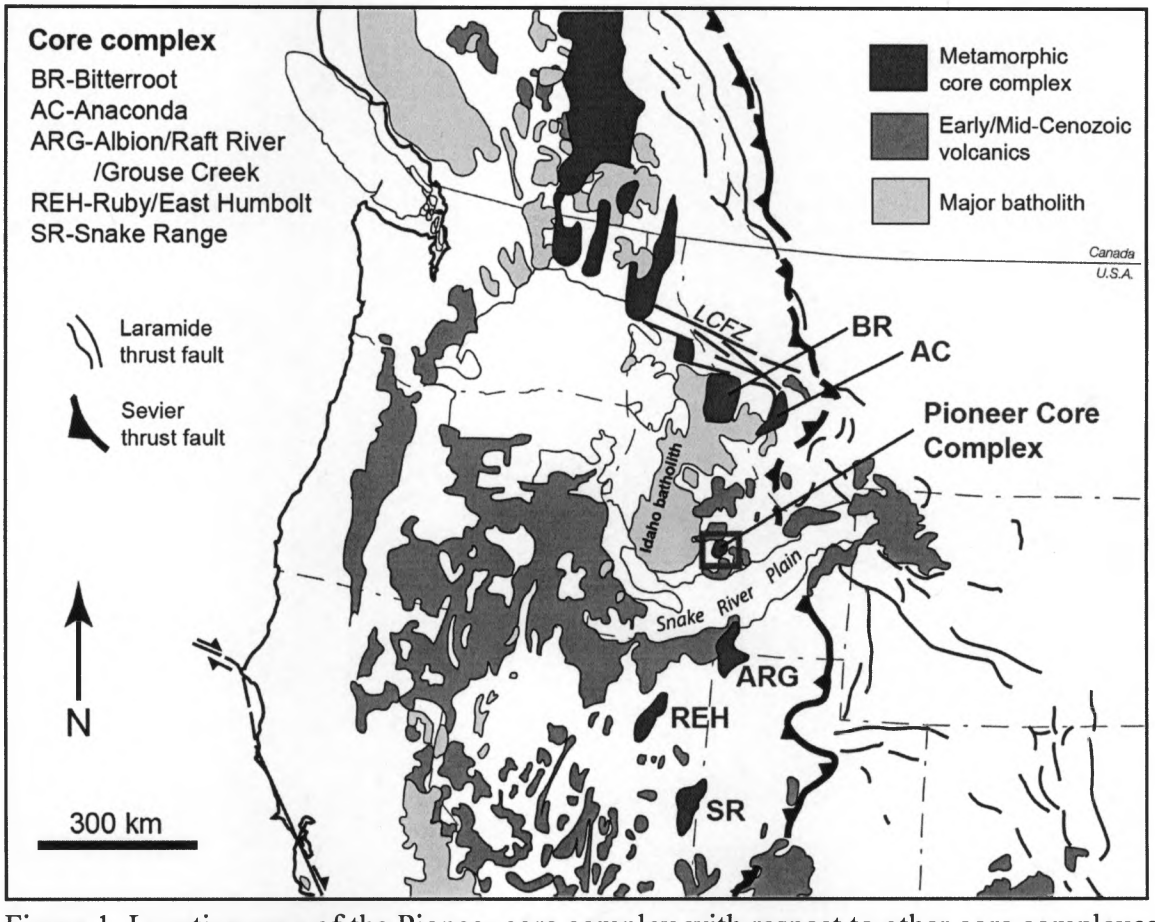

Figure 1. Location map of the Pioneer core complex with respect to other core complexes and major tectonic features in the western Cordillera (modified from Vogl et al., 2012). LCFZ is Lewis and Clark fault zone.

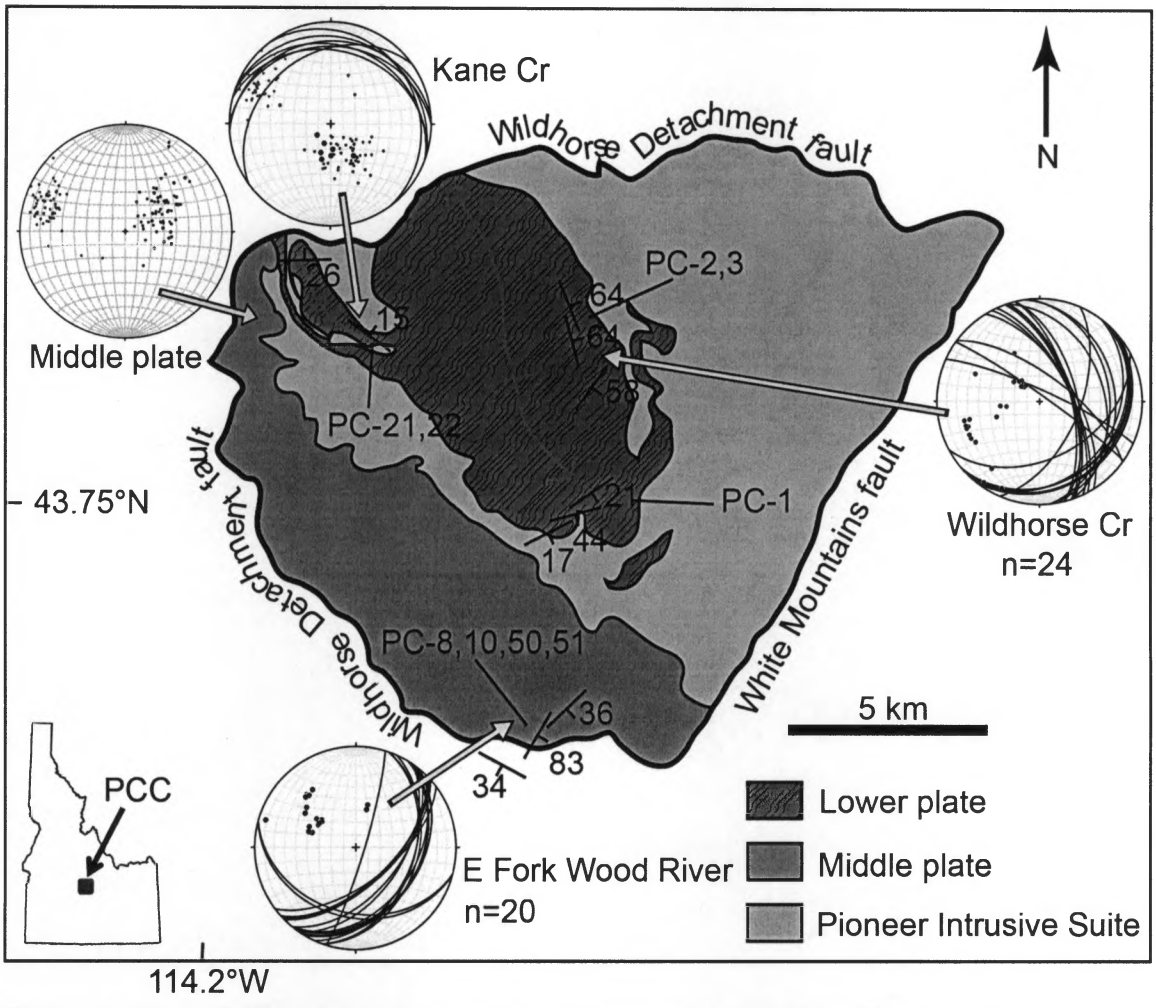

Figure 2. Simplified geological map of the Pioneer core complex. The Lower plate consists of high-grade paragneisses and orthogneisses; the Middle plate consists of metapelites, quartzites, marbles, and calc-silicates; and the Pioneer Intrusive Suite (PIS) consists of granodioritic rocks. Structural data were collected in Wildhorse Creek and Kane Creek in the Lower plate, and the E Fork Wood River area of the Middle plate. Stereonets show structural data combined data from Vogl et al (2012) from Kane Creek and Boulder Lake of the Lower plate and the NW part of the Middle plate. Black dots are poles to foliations. Red dots are lineations.


(a)
(b)
(c)
N
S
(d)
(e)
(f)

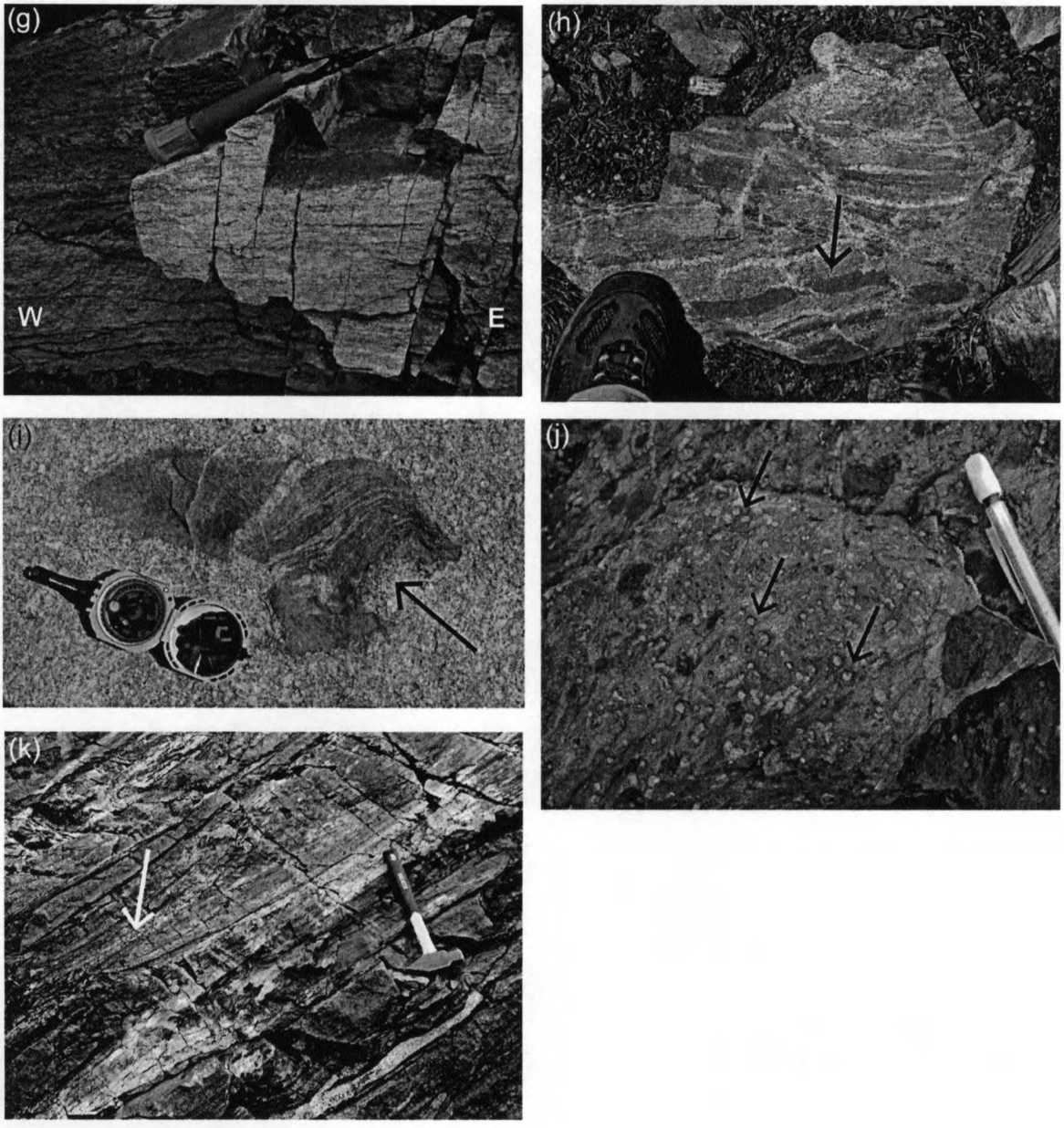

Figure 3. Field photos of lithologies and structures in the Lower and Middle plates in the Pioneer core complex. (a) Well-foliated paragneiss (float) with chevron folds in the Lower plate in Wildhorse Creek; the arrow points to chevron folds. (b) Leucogranite in Wildhorse Creek. (c) Conjugate fractures in calc-silicates, oriented at 169°, 32° NE and 122°, 78° NE, in Wildhorse Creek. Arrows point to fractures. (d) Enclaves of paragneiss and calc-silicate in granite in Wildhorse Creek. (e) Leucogranitic dikes intruded paragneisses. Arrow is pointing to the enclave of calc-silicate. (f) Weakly-foliated orthogneiss in Wildhorse Creek. (g) Well-foliated orthogneiss in the Lower plate in Kane

Creek. (h) Mafic boudinage in orthogneiss (float) in Kane Creek. (i) A mafic boudin of paragneiss in orthogneiss (float) in Kane Creek shows deformed veins after fracturing. The arrow points to the boudin. (j) Phyllite with andalusite porphyroblasts in the Middle plate in E Fork Wood River. Arrows point to andalusite porphyroblasts. (k) Isoclinal folds in foliated quartzite. The arrow points to the folds.

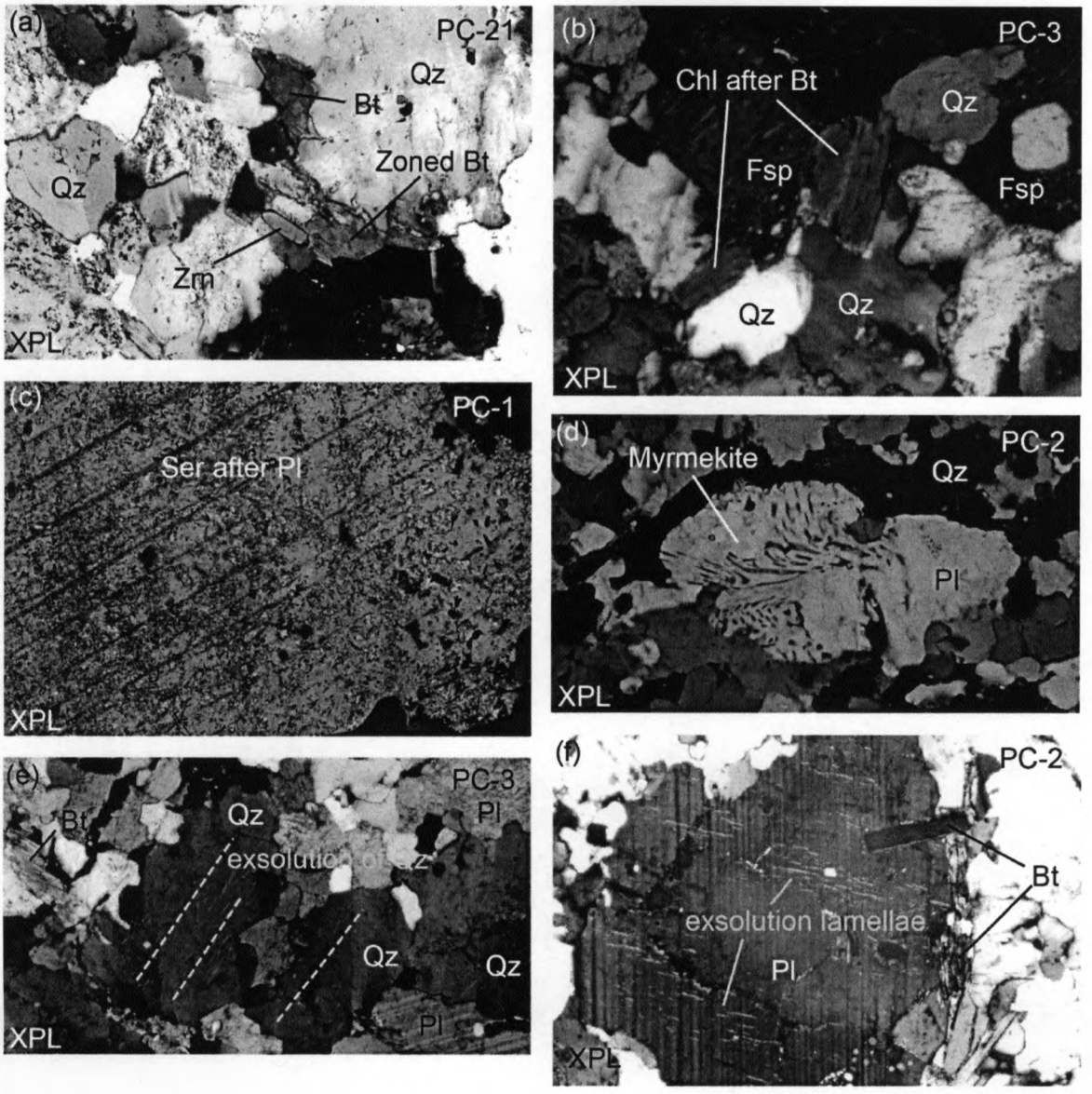
(a)
PC-21
Qz
Bt
Zoned Bt
Qz
Zm
XPL
(b)
PC-3
Chl after Bt
Qz
Fsp
Fsp
Qz
Qz
XPL
(c)
PC-1
Ser after Pl
XPL
(d)
PC-2
Myrmekite
Qz
Pl
XPL
(e)
PC-3
Pl
Bt
Qz
Qz
Qz
Pl
XPL
(f)
PC-2
Bt
exsolution lamellae
Pl
XPL

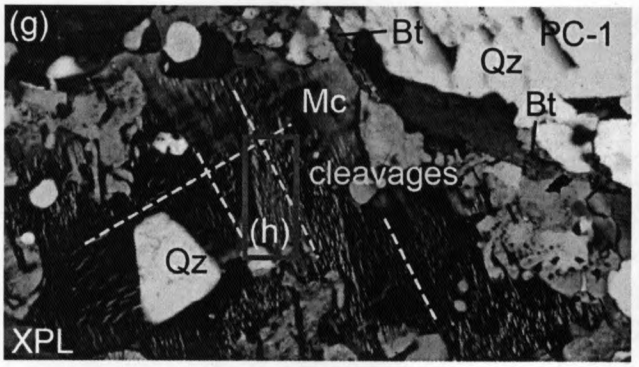
(g)
Bt
PC-1
Qz
Mc
Bt
cleavages
(h)
Qz
XPL

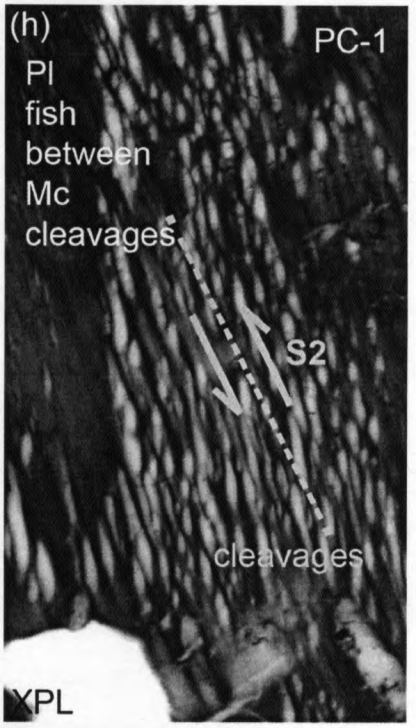
(h)
PC-1
Pl
fish
between
Mc
cleavages
S2
cleavages
XPL

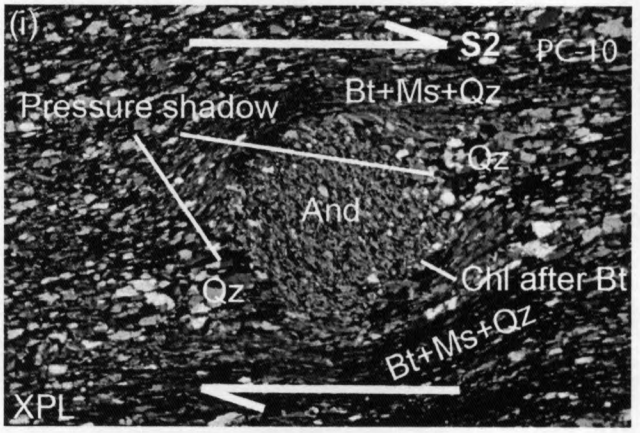
(i)
S2
PC-10
Bt+Ms+Qz
Pressure shadow
Qz
And
Qz
Chl after Bt
Bt+Ms+Qz
XPL

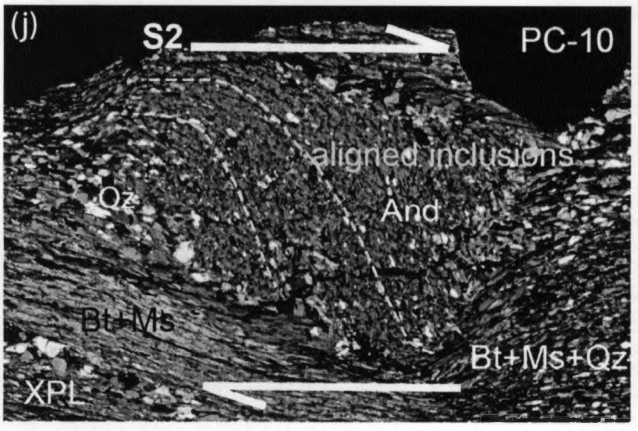
(j)
S2
PC-10
aligned inclusions
Qz
And
Bt+Ms
Bt+Ms+Qz
XPL

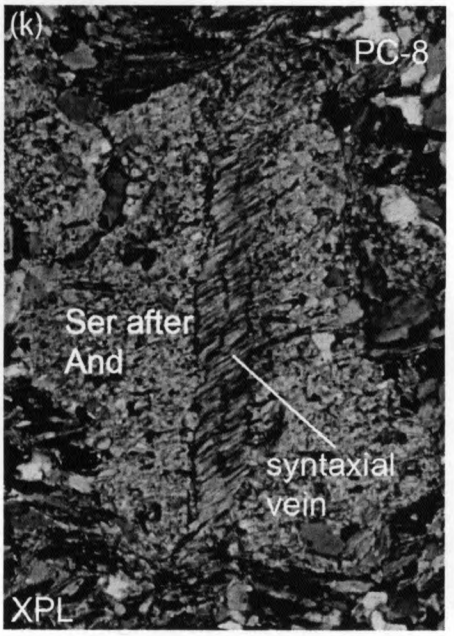
(k)
PC-8
Ser after
And
syntaxial
vein
XPL

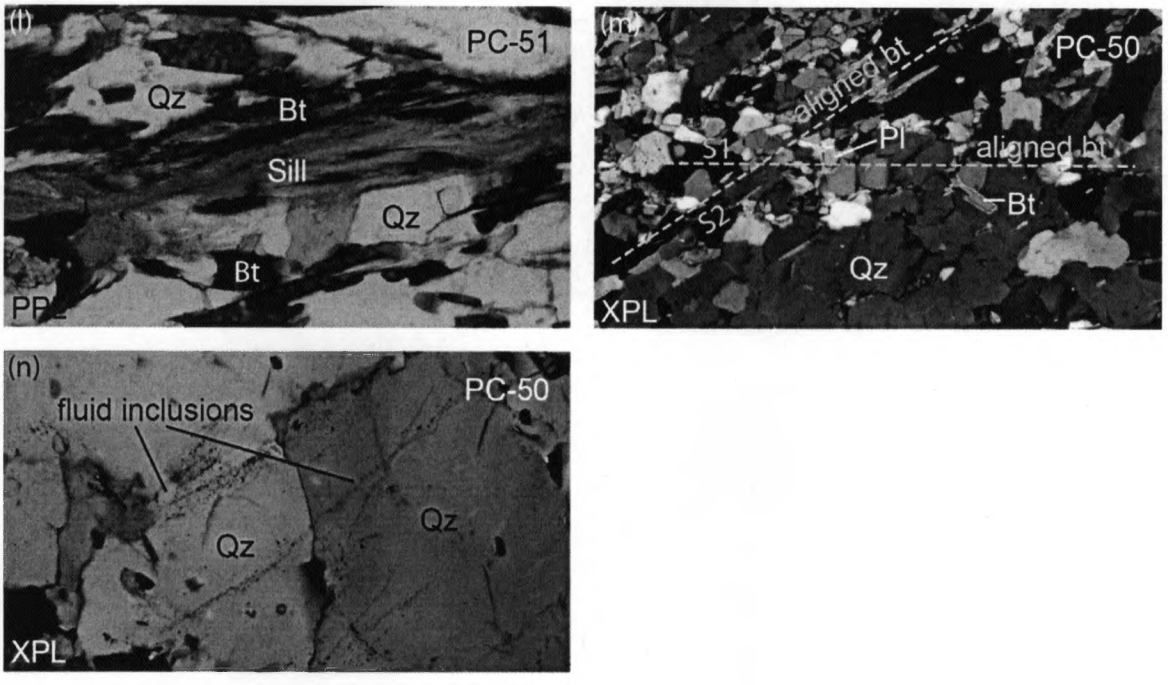

Figure 4. Petrographic photomicrographs of Lower plate gneiss (PC-1, -2, -3 and -21), andalusite phyllite (PC-10, -8), phyllite (PC-51) and quartzite (PC-50) from the Middle plate. (a) Zircons and biotite are common inclusions in quartz in gneiss (PC-21). Some biotites are zoned. (b) Biotites in PC-3 gneiss were altered to chlorite during retrogression. (c) Sericite replaced plagioclase in PC-1 gneiss indicating retrogression. (d) Myrmekite texture in plagioclase in PC-3 gneiss indicating retrogression. (e) Alignment of quartz blebs exsolved from quartz in PC-2 gneiss. (f) Exsolution lamellae (perthite) in plagioclase in PC-2 gneiss. (g) Perthite in microcline in PC-1 gneiss. A magnified photo of microcline is shown in (h). (h) Plagioclase recrystallized between microcline cleavages resembling S-C fabrics. (i) Phyllite with andalusite porphyroblasts shows well-defined foliation defined by Bt + Ms + Qz (PC-10). Some biotites around andalusite were altered to chlorite during retrogression. Pressure shadows formed around andalusite indicating S2 shear stress during D3. Andalusite prophyroblasts have a poikiloblastic texture with inclusions of quartz, biotite, and muscovite. The aligned inclusions were not deformed suggesting pre-kinematic growth of andalusite. (j) Inclusions in andalusite porphyroblast (PC-10) show distinct curvature suggesting syn-kinematic growth of andalusite. (k) Sericite replaced andalusite during retrogression in PC-8 andalusite phyllite. Fractures in andalusite created syntaxial vein with a median line. Fibers of quartz and sericite in the vein are the same minerals as along the vein walls. (l) Fibrous sillimanite grew on biotite in PC-51 phyllite. (m) Biotites aligned in two directions in PC-50 quartzite. One direction (S1) is parallel to foliation and the other foliation (S2) is at ~30°C to S1. Elongate quartz is parallel to S2. (n) Fluid inclusions in quartz in PC-50 transect with minor deflections across grain boundaries.

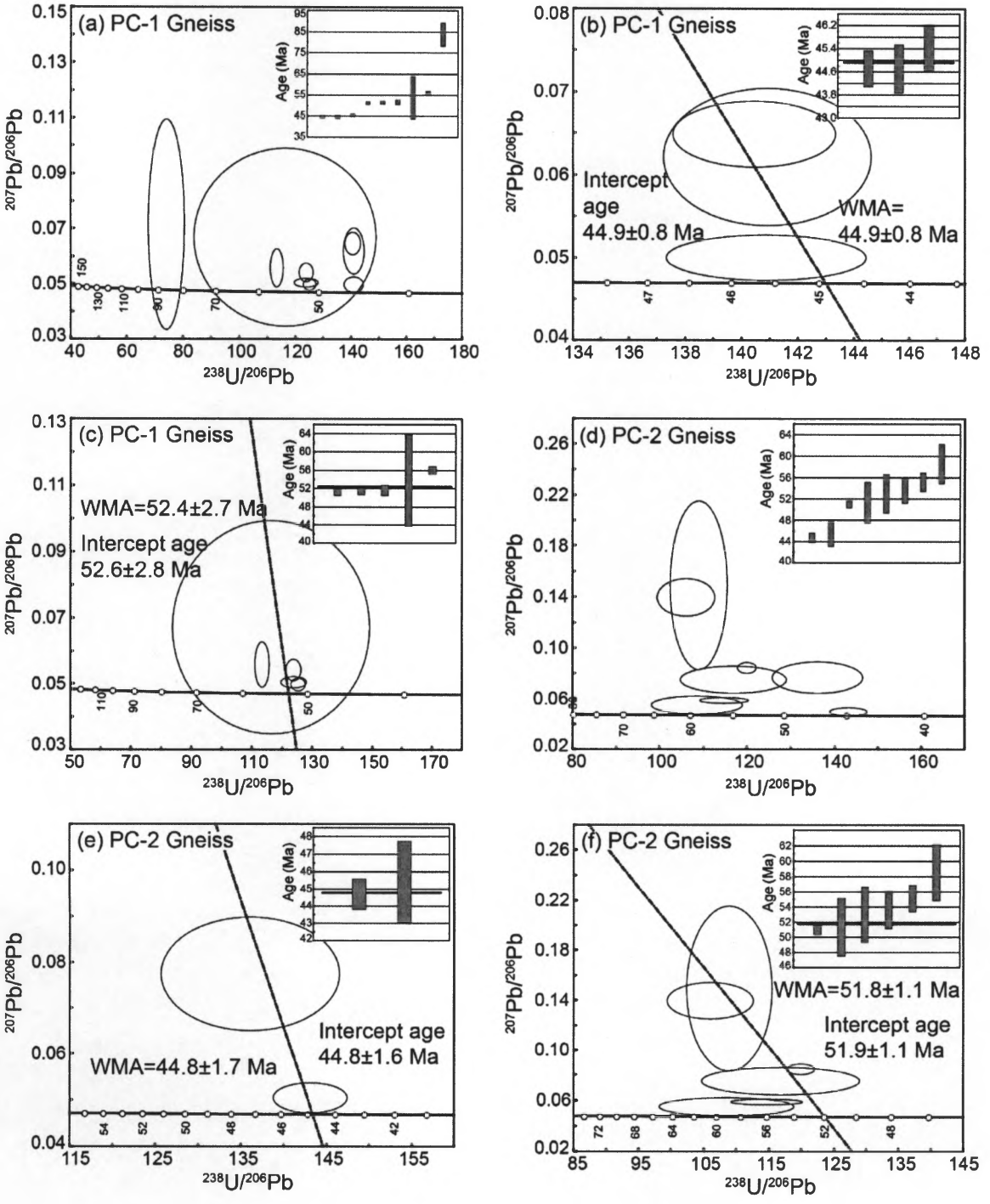
(a) PC-1 Gneiss
(b) PC-1 Gneiss
Intercept age 44.9±0.8 Ma
WMA= 44.9±0.8 Ma
(c) PC-1 Gneiss
WMA=52.4±2.7 Ma
Intercept age 52.6±2.8 Ma
(d) PC-2 Gneiss
(e) PC-2 Gneiss
WMA=44.8±1.7 Ma
Intercept age 44.8±1.6 Ma
(f) PC-2 Gneiss
WMA=51.8±1.1 Ma
Intercept age 51.9±1.1 Ma
Age (Ma)
207Pb/206Pb
238U/206Pb

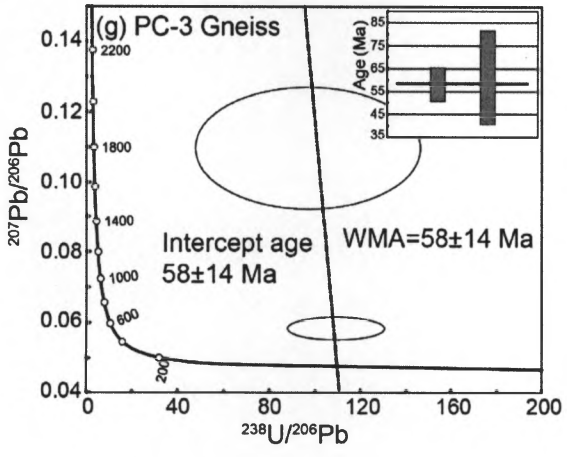
(g) PC-3 Gneiss
Intercept age
58±14 Ma
WMA=58±14 Ma
Age (Ma)
$^{207}Pb/^{206}Pb$
$^{238}U/^{206}Pb$

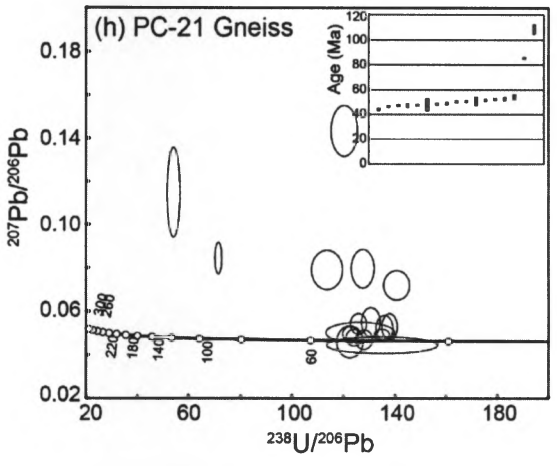
(h) PC-21 Gneiss
Age (Ma)
$^{207}Pb/^{206}Pb$
$^{238}U/^{206}Pb$

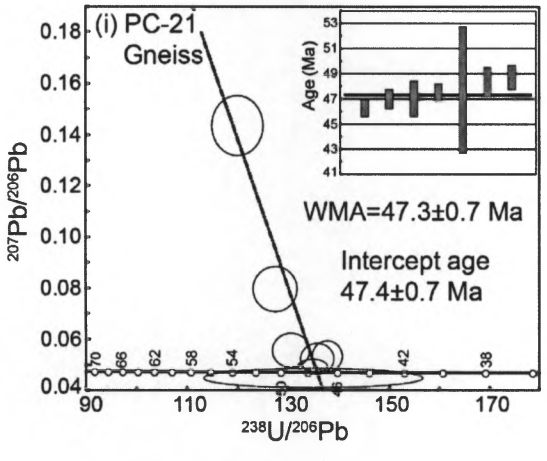
(i) PC-21
Gneiss
WMA=47.3±0.7 Ma
Intercept age
47.4±0.7 Ma
Age (Ma)
$^{207}Pb/^{206}Pb$
$^{238}U/^{206}Pb$

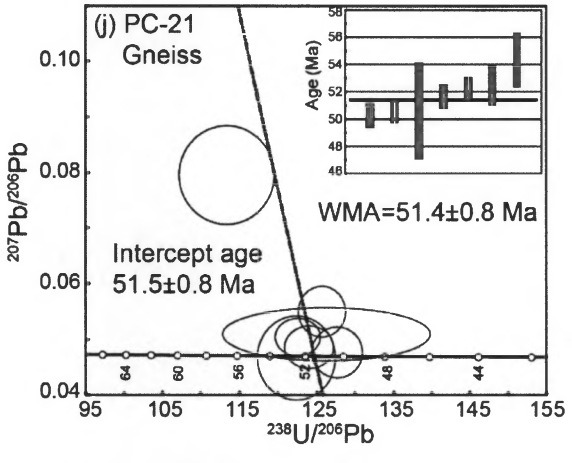
(j) PC-21
Gneiss
WMA=51.4±0.8 Ma
Intercept age
51.5±0.8 Ma
Age (Ma)
$^{207}Pb/^{206}Pb$
$^{238}U/^{206}Pb$

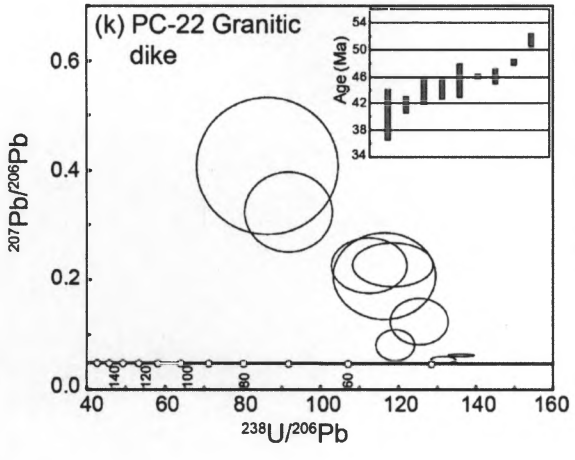
(k) PC-22 Granitic
dike
Age (Ma)
$^{207}Pb/^{206}Pb$
$^{238}U/^{206}Pb$

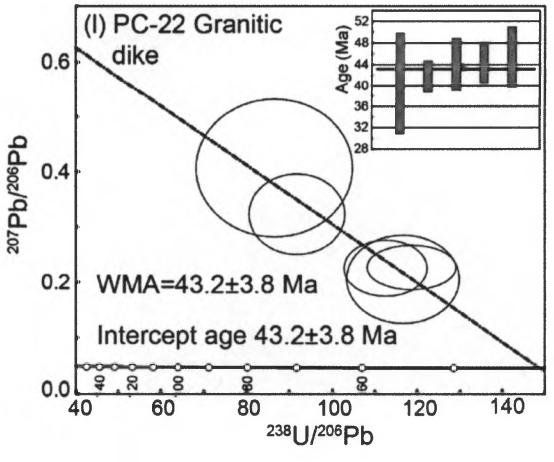
(l) PC-22 Granitic
dike
WMA=43.2±3.8 Ma
Intercept age 43.2±3.8 Ma
Age (Ma)
$^{207}Pb/^{206}Pb$
$^{238}U/^{206}Pb$

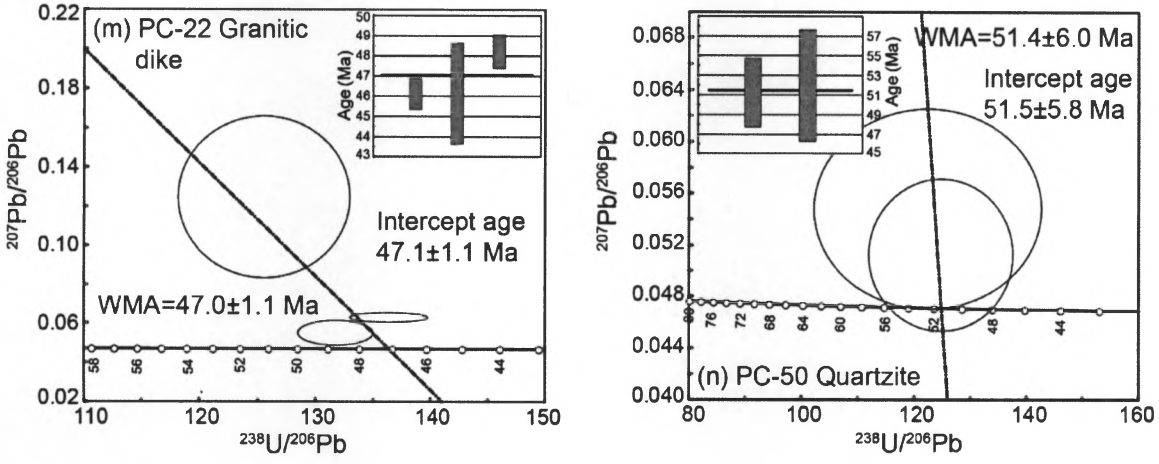

Figure 5. U-Pb concordia diagrams for zircons from samples PC-1, -2, -3, -21, -22 from the Lower plate, and PC-50 from the Middle plate. Weighted mean ages (WMA) of different age populations are shown in inset histograms (bar heights are 2σ). (a) Late Cretaceous to Early Eocene ages from all 9 zircons from sample PC-1 gneiss. Histograms suggest 3 populations: a younger group of 3 ages and an older group of 5 ages of Early Eocene, and a single, old Late Cretaceous age. (b) Three analyses fall into the younger age group from PC-1. (c) Five analyses from PC-1 fall into the older group. (d) Early Eocene ages from all 8 zircons from sample PC-2 gneiss. Histograms suggest 2 populations: a younger group of 2 ages, and an older group of 6 ages. (e) Two analyses fall into the younger age group from PC-2. (f) Six analyses from PC-2 fall into the older group. (g) Paleocene ages from all 2 zircons from sample PC-3 gneiss. (h) Late Cretaceous to Early Eocene ages from all 17 zircons from sample PC-21 gneiss. The age of 61.7 ± 16 Ma was excluded from the diagram. Histograms suggest 5 populations: a youngest group of 1 age, a younger group of 7 ages, and an older group of 7 ages of Early Eocene, and 2 oldest Late Cretaceous ages that fall into 2 groups. (i) Seven analyses fall into the younger group from PC-21. (j) Seven analyses fall into the older group from PC-21. (k) Early Eocene ages from all 9 zircons from sample PC-22 granitic dike. Histograms suggest 3 populations: a younger group of 5 ages, an older group of 3 ages, and an oldest group of 1 age. (l) Five analyses fall into the younger group from PC-22. (m) Three analyses fall into the older group from PC-22. (n) Early Eocene ages from all 2 zircons from sample PC-50 quartzite.

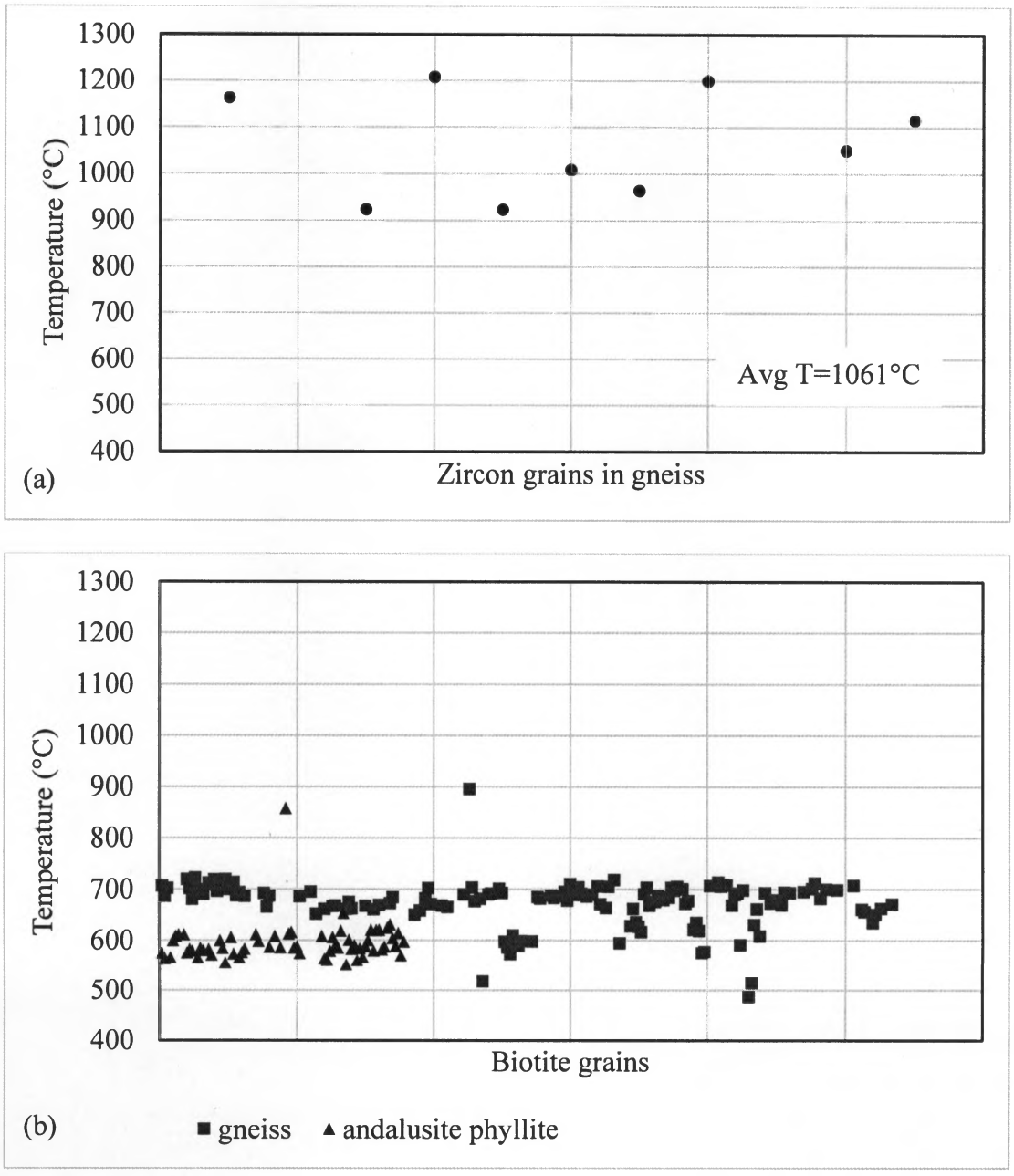

Figure 6. Plots of Ti-in-zircon and Ti-in-biotite thermometries. (a) Temperatures calculated from Ti-in-zircon thermometry. Zircons were from gneisses (PC-1, -2, and -3) from the Lower plate. The average temperature of all 9 zircons is 1061°C. (b) Temperatures calculated from Ti-in-biotite thermometry. Biotites were from the Lower plate gneisses (PC-1, -2, -3 and -21) and andalusite phyllite (PC-10) from the Middle plate.

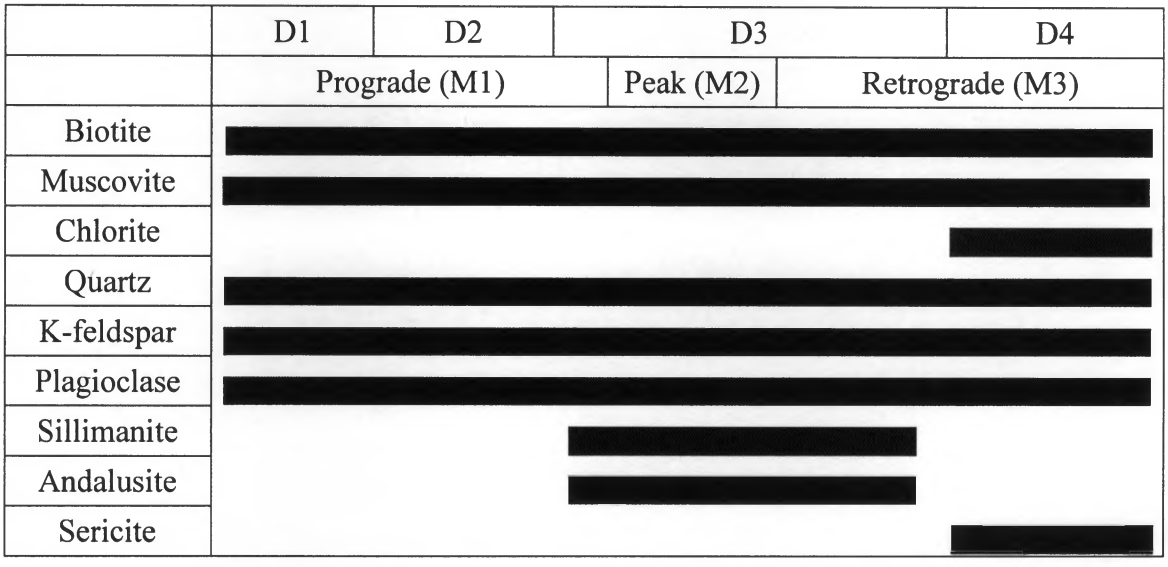

Figure 7. Relationship between mineral crystallization, metamorphic phases (prograde, peak and retrograde). and deformation events. D1 is related to Cretaceous compression ~109 Ma; D2 is Late Cretaceous compression c. 86-84 Ma; D3 corresponds to Early Eocene extension 52-44 Ma; and D4 is Late Eocene extension 36-33 Ma inferred from Silverberg (1990).

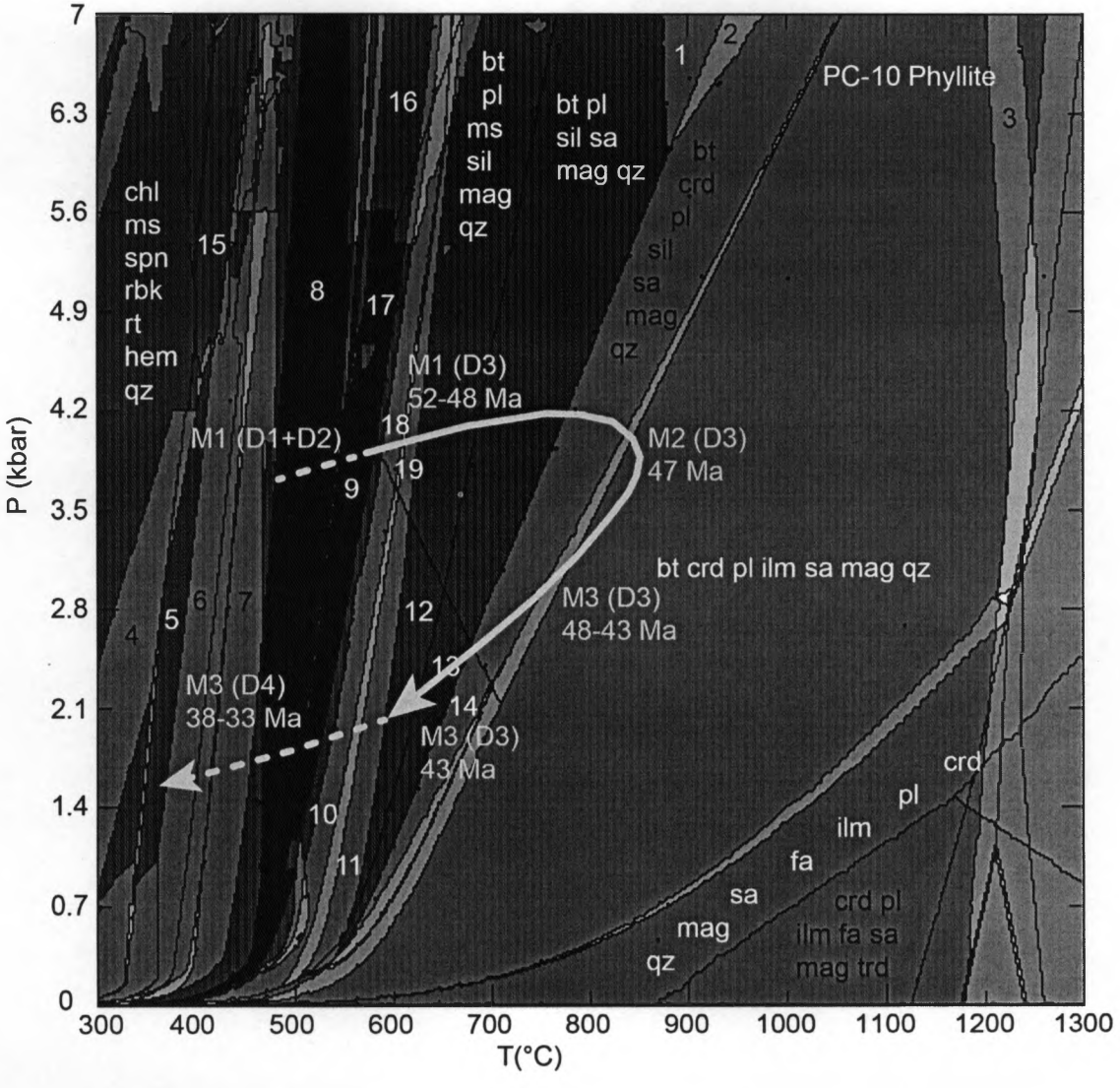

1 - bt pl grt sil sa mag qz
2 - bt crd pl grt sil sa mag qz
3 - bt crd pl ilm grt sa mag qz
4 - chl ms spn rbk ab rt hem qz
5 - chl ms spn ab rt mag qz
6 - bt chl ms spn ab rt mag qz
7 - bt chl pl ms ilm rt mag qz
8 - bt chl ms ilm mag qz
9 - bt ms ilm and mag qz
10 - bt pl ms ilm and mag qz
11 - bt pl ms and rt mag qz
12 - bt pl ms and mag qz
13 - bt pl and sa mag qz
14 - bt crd pl and sa mag qz
15 - chl ms amp spn rt mag qz
16 - bt ms ilm grt ky mag qz
17 - bt ms ilm sil mag qz
18 - bt pl ms ilm sil mag qz
19 - bt pl ms sil ru mag qz

Figure 8. Pseudosection of PC-10 andalusite phyllite. Each field with different shades of gray represents a mineral assemblage that is stable under specific P-T conditions. Temperature constraints are taken from Ti-Bt thermobarometry. Pressure constraints are inferred from Silverberg (1990). The clockwise P-T path is estimated based on mineral assemblages. ab-albite; abL-albite liquid; amp-amphibole; and-andalusite; bt-biotite; chl-chlorite; cpx-clinopyroxene; crd-cordierite; ep-epidote; fa-fayalite; grt-garnet; hem-hematite; ilm-ilmenite; ky-kyanite; lc-leucite; mc-microline; ms-muscovite; mag-magnetite; pl-plagioclase; qz-quartz; rbk-riebeckite; rt-rutile; sa-sanidine; sil-sillimanite; spn-sphene (titanite).

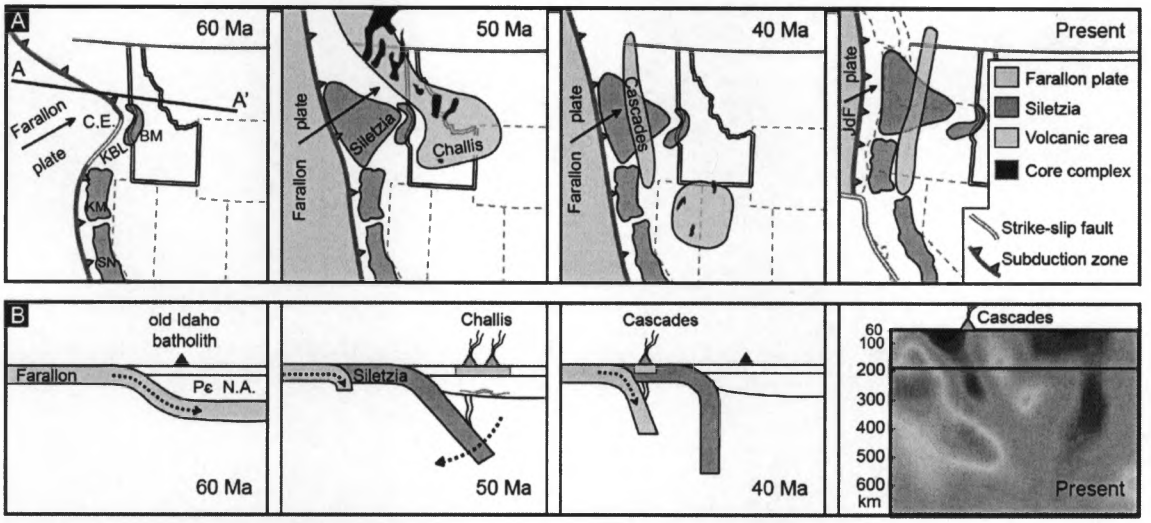

Figure 9. Maps and cross sections of the northwestern U.S. at 60, 50, 40, and 0 Ma. The border of Idaho is highlighted. (A) Maps illustrating the regional tectonic and magmatic evolution. Coherent units defined by the presence of Mesozoic to Cretaceous plutons and associated arc-related rocks are shown in pink—Klamath Mountains (KM), Blue Mountains (BM), and Sierra Nevada (SN). Prior to accretion at 60 Ma, the Klamath–Blue Mountains lineament (KBL) is shown as a transform boundary. At 60 Ma, the Farallon plate was subducting to the northeast in the Columbia Embayment (C.E.). The Siletzia micro-ocean plate accretion and subduction stepped west c. 55–53 Ma, and by 50 Ma the Challis magmatism was going strong (JdF—Juan de Fuca). (B) Cross-section A–A′ (shown in A, first panel) shows the interpreted subduction history. At 60 Ma, the Farallon plate subducted flat against Precambrian North America (Pc N.A.). Shortly after Siletzia accretion (c. 50 Ma), Cascadia subduction initiated, and the abandoned, previously flat Farallon plate rolled back, exposing basal North America and Farallon crust to inflowing asthenosphere, causing Cascades volcanism. That magmatic event ended by 40 Ma, and little has changed to present, represented by the seismic tomography cross section, A–A′ (Modified from Schmandt and Humphreys, 2011).

Appendix I. Summary of ages in the Pioneer core complex from the literature.

Age (Ma)	Rock type	Dating method	Mineral	Pioneer region	Reference
5.2 to 13.6	Granitic rocks	U-Th/He	Ap	Summit Creek Stock	Vogl et al (2014)
7.7±1.3	Granitic rocks	U-Th/He	Ap	Summit Creek Stock	
7.7 to 9.8	Granitic rocks	U-Th/He	Ap	PIS	
8.7 to 11.9	Granitic rocks	U-Th/He	Ap	Lower plate	
9.6±1.8	Granitic rocks	U-Th/He	Ap	Garfield Stock	
12.4	Granitic rocks	U-Th/He	Ap	Lower plate	
16.6±2.1	Granitic rocks	U-Th/He	Ap	Garfield Stock	
29.6±0.9	Granitic rocks	U-Th/He	Ap	Lake Creek Stock	
34.0±1.1	Granitic rocks	U-Th/He	Ap	Lake Creek Stock	
44.0±6.6	Granitic rocks	U-Th/He	Ap	Mackay Stock	
42±1.0 to 47.1±1.4	quartz monzonite	K-Ar	Bt	PIS	Armstrong (1975) [cited by O'Neill & Pavlis (1988)]
43±1.3 to 50.4±1.85	Challis volcanics	K-Ar		adjacent to PCC	
53.9±1.3	quartz monzonite	K-Ar	Hbl	PIS	Dover (1983) [cited by O'Neill & Pavlis (1988)]
67.6±1.6	granodiorite	K-Ar	Hbl	PIS	
2 Ga	gneiss	Rb-Sr		Lower plate	
33.0±0.6	quartz monzonite	Ar/Ar	Kfs	PIS	Silverberg (1990)
34.7±0.5	psammitic schist	Ar/Ar	Bt	Lower plate	
35.2±0.4	granodioritic gneiss	Ar/Ar	Bt	PIS	
35.9±0.6	psammitic schist	Ar/Ar	Ms	Lower plate	
36.1±0.4	psammitic schist	Ar/Ar	Bt	Lower plate	
36.4±0.3	quartzite	Ar/Ar	Ms	Middle plate	
36.6±0.3	mica schist	Ar/Ar	Ms	Middle plate	
36.8±0.4	granodioritic gneiss	Ar/Ar	Bt	PIS	
37.5±0.4	dioritic gneiss	Ar/Ar	Bt	PIS	

37.8±0.4	hypabyssal mafic dike	Ar/Ar	Bt	PIS	
37.9±0.4	mafic schist	Ar/Ar	Bt	Middle plate	
42.9±0.8	mafic schist	Ar/Ar	Hbl	Middle plate	
44.2±0.5	Qfp gneiss	Ar/Ar	Kfs	Lower plate	
44.5±0.5	quartz monzonite	Ar/Ar	Kfs	Summit Creek Stock	
44.6±0.3	granodioritic gneiss	Ar/Ar	Hbl	PIS	
44.7±0.8	granodioritic gneiss	Ar/Ar	Hbl	PIS	
46.8±3.4	hypabyssal mafic dike	Ar/Ar	Hbl	PIS	
47.1±0.6	quartz monzonite	Ar/Ar	Bt	Summit Creek Stock	
49.5±0.8	mafic schist	Ar/Ar	Hbl	Lower plate	
50.3±0.3	granodiorite	Ar/Ar	Hbl	PIS	
53.2±7.0	amphibolitic schist	Ar/Ar	Hbl	Lower plate	
55.6±10.0	amphibolitic schist	Ar/Ar	Hbl	Lower plate	
79.3±1.1	amphibolitic schist	Ar/Ar	Hbl	Lower plate	
45.7±0.8	leucogranite	U/Pb	Zrn	Middle plate	Vogl et al (2012)
45.9±0.3	granitic dike	U/Pb	Zrn	Middle plate	
47.1±0.7	leucogranite dike	U/Pb	Zrn	Middle plate	
47.1±0.8	leucogranite	U/Pb	Zrn	Lower plate	
48.3±0.6	quartz monzonite	U/Pb	Zrn	PIS	Dover (1981) [cited by Vogl et al (2012)]
48.6±0.4	granodiorite	U/Pb	Zrn	PIS	Vogl et al (2012)
48.9±1.2	leucogranite	U/Pb	Zrn	Lower plate	
49.0±0.4	syenite	U/Pb	Zrn	PIS	Link & Fanning (2006) [cited by Vogl et al (2012)]
49.4±0.4	Bt granite	U/Pb	Zrn	PIS	Vogl et al (2012)
49.4±0.5	leucogranite	U/Pb	Zrn	Lower plate	
52.3±1.8	migmatite	U/Pb	Zrn	Lower plate	

54.8±0.8 to 60.8±0.8	leucogranite	U/Pb	Zrn	Lower plate	
695 Ma	orthogneiss	U/Pb	Zrn	Lower plate	Durk (2007) [cited by Vogl et al (2012)]
1.0 Ga	quartzite, calc-silicate	U/Pb	Zrn	Middle plate	Link et al (2010) [cited by Vogl et al (2012)]
2.6 Ga	orthogneiss	U/Pb	Zrn	Lower plate	Durk (2007) [cited by Vogl et al (2012)]

Appendix II. Ti-in-zircon thermometry results for samples PC-1, -2 and -3.

Sample	Grain No.	SiO_2	TiO_2	ZrO_2	Total (%)	Ti (ppm)	T(°C)	Avg T(°C)
PC-1 Gneiss	Zrn-1	23.082	0.039	63.229	86.350	233	1162	1162
PC-2 Gneiss	Zrn-1	32.408	0.008	66.215	98.631	50	923	1038
	Zrn-2	33.073	0.049	65.897	99.019	295	1208	
	Zrn-3	27.691	0.008	63.217	90.917	50	923	
	Zrn-4	32.456	0.015	66.522	98.993	92	1009	
	Zrn-5	32.620	0.011	65.439	98.070	68	964	
	Zrn-6	31.684	0.047	66.065	97.796	283	1199	
PC-3 Gneiss	Zrn-1	32.986	0.020	66.537	99.543	121	1050	1083
	Zrn-2	32.033	0.030	65.471	97.534	179	1115	

Note: Temperatures are calculated using the formulation of (Ferry and Watson, 2007). Oxides are given in units of weight percent.

Appendix III. Ti-in-biotite thermometry results for samples PC-1, -2, -3, -10 and -21.

Grain No.	SiO_2	TiO_2	Al_2O_3	FeO	MnO	MgO	CaO	Na_2O	K_2O	Cl	Cr_2O_3	Total (%)	Ti (apfu)	X (Mg)	Mg (apfu)	Fe (apfu)	T (°C)	Avg T (°C)
PC-10 Andalusite phyllite																		
Bt-1	34.878	1.744	18.592	21.276	0.231	8.362	0.013	0.215	9.563	0.014	0.013	94.897	0.203	0.412	1.931	2.756	575	575
Bt-2	33.545	1.592	18.662	22.440	0.259	9.047	0.019	0.164	8.082	0.017	0.051	93.874	0.188	0.418	2.115	2.943	560	563
	35.235	1.692	18.533	21.541	0.186	8.388	0.000	0.195	9.583	0.026	0.012	95.384	0.196	0.410	1.927	2.776	567	
Bt-3	34.511	1.657	18.624	21.114	0.197	8.454	0.035	0.215	9.443	0.000	0.030	94.279	0.194	0.417	1.965	2.752	566	566
Bt-4	34.213	1.946	18.207	21.750	0.220	8.327	0.000	0.205	9.582	0.001	0.032	94.484	0.229	0.406	1.942	2.845	599	599
Bt-5	34.541	2.050	18.477	21.668	0.204	8.236	0.029	0.223	9.330	0.015	0.053	94.823	0.24	0.404	1.908	2.815	608	608
Bt-6	34.680	2.261	17.461	23.177	0.238	7.079	0.042	0.096	9.181	0.024	0.041	94.273	0.268	0.353	1.661	3.051	622	611
	34.499	1.951	18.247	21.296	0.238	8.351	0.024	0.260	9.437	0.013	0.031	94.345	0.229	0.411	1.943	2.78	600	
Bt-7	34.979	2.110	19.064	21.194	0.208	7.824	0.012	0.153	9.571	0.014	0.038	95.164	0.245	0.397	1.799	2.733	611	611
Bt-8	34.745	1.735	18.568	21.176	0.216	8.293	0.000	0.165	9.444	0.013	0.031	94.383	0.203	0.411	1.924	2.756	575	575
Bt-9	34.286	1.784	18.135	21.485	0.221	8.155	0.000	0.227	9.202	0.032	0.040	93.558	0.211	0.404	1.914	2.829	582	582
Bt-10	34.331	1.717	18.755	21.772	0.195	8.095	0.008	0.117	8.128	0.024	0.028	93.165	0.203	0.399	1.894	2.858	573	579
	36.775	1.898	20.296	20.138	0.189	7.546	0.031	0.194	9.062	0.018	0.019	96.159	0.214	0.401	1.689	2.528	585	
Bt-11	34.800	1.655	18.686	20.861	0.188	8.414	0.000	0.191	9.557	0.004	0.000	94.354	0.193	0.418	1.949	2.712	566	566
Bt-12	34.594	1.804	18.518	21.324	0.228	8.524	0.000	0.122	9.564	0.018	0.002	94.693	0.211	0.416	1.974	2.771	584	584
Bt-13	34.700	1.771	18.672	20.863	0.196	8.414	0.040	0.224	9.437	0.002	0.000	94.320	0.207	0.418	1.95	2.713	581	580
	34.021	1.698	18.197	20.425	0.184	9.074	0.033	0.199	9.540	0.017	0.031	93.416	0.201	0.442	2.128	2.687	579	
Bt-14	34.183	1.777	18.382	21.130	0.205	8.206	0.012	0.193	9.319	0.010	0.026	93.439	0.21	0.409	1.926	2.782	582	582
Bt-15	34.893	1.644	18.895	21.156	0.216	8.842	0.033	0.237	9.369	0.017	0.029	95.325	0.19	0.427	2.028	2.723	564	571
	33.790	1.693	18.557	21.533	0.185	8.680	0.012	0.206	8.844	0.003	0.030	93.531	0.2	0.418	2.035	2.832	573	
	34.690	1.745	18.805	21.460	0.249	8.264	0.016	0.232	9.424	0.005	0.036	94.925	0.203	0.407	1.909	2.781	575	
Bt-16	34.228	1.969	18.757	21.750	0.236	7.967	0.025	0.205	9.183	0.010	0.034	94.361	0.231	0.395	1.854	2.84	599	599
Bt-17	33.760	1.792	18.436	21.551	0.214	8.243	0.026	0.230	9.117	0.010	0.019	93.394	0.213	0.405	1.94	2.845	584	584
Bt-18	34.558	1.525	18.983	21.085	0.224	8.097	0.018	0.303	9.231	0.004	0.039	94.065	0.179	0.406	1.882	2.75	546	555
	34.009	1.641	18.785	21.103	0.228	8.243	0.048	0.273	9.252	0.000	0.030	93.612	0.194	0.410	1.93	2.773	565	
Bt-19	34.495	2.017	18.448	21.257	0.249	8.083	0.003	0.261	9.575	0.019	0.026	94.429	0.237	0.404	1.88	2.773	606	606
Bt-20	34.682	1.820	18.646	21.450	0.254	8.529	0.037	0.300	9.290	0.020	0.041	95.065	0.212	0.415	1.967	2.776	585	573
	34.824	1.633	18.607	21.282	0.192	8.237	0.021	0.244	9.423	0.010	0.062	94.534	0.191	0.408	1.909	2.767	561	

Bt-21	34.937	1.695	19.344	21.176	0.165	7.538	0.042	0.191	9.489	0.008	0.030	94.612	0.198	0.388	1.741	2.744	566	566
Bt-22	34.880	1.734	18.500	20.911	0.137	8.124	0.057	0.262	8.961	0.006	0.046	93.615	0.204	0.409	1.892	2.732	576	576
Bt-23	34.610	1.860	18.978	21.399	0.301	8.163	0.010	0.234	9.309	0.000	0.035	94.900	0.217	0.405	1.884	2.771	588	583
	34.357	1.753	18.758	21.225	0.254	7.868	0.010	0.259	9.158	0.020	0.031	93.689	0.207	0.398	1.839	2.783	577	
	34.528	1.822	18.680	21.209	0.222	8.223	0.014	0.285	9.347	0.008	0.012	94.348	0.213	0.409	1.909	2.762	585	
	34.303	1.789	18.374	21.355	0.238	7.804	0.047	0.224	9.221	0.005	0.039	93.396	0.212	0.394	1.833	2.814	582	
Bt-24	34.779	2.106	18.712	21.441	0.268	7.862	0.013	0.253	9.311	0.005	0.037	94.786	0.246	0.395	1.817	2.78	612	612
Bt-25	34.789	2.028	18.462	21.481	0.256	8.131	0.040	0.261	9.241	0.010	0.037	94.732	0.237	0.403	1.881	2.788	606	598
	34.681	1.943	18.461	22.055	0.206	8.116	0.019	0.233	8.960	0.017	0.021	94.708	0.227	0.396	1.88	2.866	596	
	34.929	1.875	18.547	21.317	0.230	7.999	0.036	0.239	9.312	0.018	0.042	94.540	0.219	0.401	1.852	2.769	589	
	34.843	1.978	18.663	20.787	0.159	8.085	0.029	0.292	9.185	0.024	0.044	94.083	0.231	0.409	1.875	2.705	602	
Bt-26	35.396	1.824	19.117	20.886	0.174	8.351	0.085	0.189	9.065	0.014	0.028	95.126	0.21	0.416	1.909	2.679	583	587
	34.399	1.876	18.463	21.861	0.229	8.276	0.064	0.224	8.830	0.006	0.005	94.232	0.22	0.403	1.925	2.853	591	
Bt-27	34.844	2.035	18.593	21.635	0.207	8.068	0.013	0.234	8.931	0.015	0.029	94.602	0.237	0.399	1.865	2.806	605	608
	34.253	2.088	18.099	22.143	0.236	7.757	0.034	0.245	9.058	0.014	0.024	93.948	0.247	0.384	1.817	2.911	611	
Bt-28	34.553	1.751	18.398	21.726	0.226	8.005	0.011	0.191	9.010	0.024	0.016	93.906	0.206	0.396	1.869	2.845	576	586
	35.874	1.954	18.812	20.832	0.221	7.719	0.023	0.191	9.133	0.009	0.041	94.807	0.226	0.398	1.769	2.678	595	
Bt-29	31.246	13.797	16.034	19.028	0.191	7.001	0.072	0.134	7.035	0.007	0.029	94.572	1.599	0.396	1.608	2.452	858	858
Bt-30	35.425	2.099	18.199	21.072	0.212	8.260	0.009	0.228	9.399	0.011	0.000	94.910	0.244	0.411	1.901	2.72	613	613
Bt-31	34.646	2.144	17.995	22.200	0.200	7.982	0.010	0.140	9.237	0.021	0.006	94.575	0.252	0.391	1.857	2.897	616	616
Bt-32	34.969	1.836	19.058	20.707	0.188	7.902	0.004	0.195	9.705	0.017	0.000	94.577	0.214	0.405	1.825	2.682	585	585
Bt-33	34.498	1.851	18.760	21.276	0.192	8.070	0.031	0.221	9.214	0.015	0.023	94.148	0.217	0.403	1.876	2.775	588	588
Bt-34	36.009	1.661	18.603	20.873	0.194	7.524	0.021	0.202	9.180	0.014	0.026	94.305	0.193	0.391	1.734	2.699	560	574
	34.791	1.809	18.585	21.098	0.269	7.515	0.000	0.191	9.266	0.026	0.087	93.630	0.213	0.388	1.756	2.766	582	
	35.002	1.662	18.921	20.873	0.263	8.195	0.017	0.234	9.488	0.012	0.027	94.690	0.193	0.412	1.891	2.702	564	
	34.258	1.659	18.380	21.457	0.279	7.921	0.005	0.171	9.338	0.037	0.058	93.553	0.197	0.397	1.861	2.827	566	
	35.226	1.706	18.563	21.175	0.244	7.529	0.027	0.122	8.606	0.021	0.042	93.256	0.201	0.388	1.756	2.771	569	
	34.788	1.809	18.429	21.016	0.223	7.720	0.024	0.122	9.599	0.021	0.046	93.793	0.213	0.396	1.803	2.754	583	
	34.874	1.946	18.540	21.565	0.218	7.809	0.033	0.162	9.413	0.011	0.061	94.630	0.228	0.392	1.81	2.804	596	
	34.836	1.755	18.608	21.643	0.234	7.867	0.025	0.166	9.419	0.002	0.051	94.606	0.205	0.393	1.824	2.815	574	
Bt-35	34.855	2.041	18.371	21.019	0.226	8.165	0.044	0.258	9.349	0.011	0.049	94.385	0.239	0.409	1.893	2.734	608	608
Bt-36	33.891	1.619	18.551	21.806	0.230	8.787	0.046	0.209	8.387	0.029	0.038	93.586	0.191	0.418	2.056	2.863	563	563

Bt-37	34.197	1.592	18.294	21.054	0.171	8.377	0.026	0.208	9.164	0.015	0.047	93.142	0.189	0.415	1.97	2.778	560	560
Bt-38	35.081	1.779	18.233	21.428	0.200	7.885	0.004	0.236	8.977	0.007	0.031	93.857	0.209	0.396	1.836	2.799	579	579
Bt-39	35.113	2.035	18.316	21.502	0.197	8.131	0.000	0.266	9.324	0.010	0.012	94.903	0.237	0.403	1.876	2.783	606	606
Bt-40	35.196	1.884	19.121	21.304	0.204	8.417	0.003	0.251	9.240	0.012	0.051	95.679	0.217	0.413	1.921	2.728	590	590
Bt-41	35.124	1.839	19.067	20.453	0.208	7.621	0.019	0.149	9.539	0.025	0.027	94.066	0.215	0.399	1.765	2.657	585	585
Bt-42	34.666	2.169	18.634	21.094	0.208	8.088	0.057	0.223	9.303	0.023	0.007	94.467	0.253	0.406	1.873	2.74	619	619
Bt-43	34.823	2.685	18.851	21.102	0.227	7.545	0.000	0.255	9.500	0.016	0.048	95.050	0.312	0.389	1.738	2.726	653	653
Bt-44	35.463	1.588	20.578	19.321	0.211	7.421	0.022	0.313	9.321	0.014	0.059	94.306	0.183	0.406	1.698	2.48	551	551
Bt-45	34.062	1.965	18.840	21.320	0.252	7.880	0.002	0.232	9.514	0.023	0.028	94.114	0.232	0.397	1.84	2.792	601	601
Bt-46	33.860	1.770	18.199	21.341	0.209	8.404	0.004	0.245	9.467	0.019	0.021	93.534	0.21	0.412	1.977	2.817	583	583
Bt-47	34.333	1.869	18.445	21.529	0.250	8.080	0.000	0.216	9.330	0.015	0.017	94.081	0.22	0.401	1.886	2.819	590	590
Bt-48	33.450	1.621	18.273	23.237	0.294	8.325	0.026	0.158	8.040	0.019	0.007	93.445	0.193	0.390	1.964	3.075	560	560
Bt-49	34.189	1.804	18.752	21.499	0.260	8.334	0.011	0.232	9.101	0.013	0.027	94.220	0.212	0.409	1.94	2.807	584	584
Bt-50	34.553	1.690	19.349	20.961	0.244	7.587	0.014	0.172	9.357	0.014	0.024	93.962	0.198	0.392	1.764	2.734	566	566
Bt-51	34.804	1.864	18.551	21.547	0.258	8.008	0.026	0.193	9.498	0.022	0.069	94.833	0.218	0.398	1.854	2.799	588	588
Bt-52	33.879	2.002	18.151	23.435	0.262	7.736	0.058	0.155	9.318	0.027	0.036	95.052	0.236	0.370	1.808	3.072	600	600
Bt-53	34.126	2.164	18.118	21.679	0.207	8.372	0.011	0.188	9.288	0.023	0.040	94.211	0.255	0.408	1.955	2.84	620	620
Bt-54	34.286	1.765	18.284	21.456	0.208	8.044	0.020	0.213	8.815	0.031	0.063	93.178	0.209	0.401	1.891	2.83	580	580
Bt-55	34.423	2.165	17.829	21.596	0.209	8.051	0.023	0.238	9.281	0.018	0.011	93.840	0.256	0.399	1.886	2.837	620	620
Bt-56	35.156	2.197	18.493	21.314	0.194	8.211	0.008	0.221	9.273	0.018	0.015	95.094	0.255	0.407	1.887	2.748	620	620
Bt-57	35.528	1.824	18.755	21.362	0.223	8.173	0.012	0.210	9.633	0.004	0.036	95.757	0.21	0.405	1.867	2.738	581	581
Bt-58	34.909	1.837	18.455	21.231	0.175	8.298	0.045	0.204	9.194	0.018	0.033	94.394	0.215	0.411	1.922	2.759	587	587
Bt-59	34.781	2.234	18.139	21.277	0.163	8.045	0.013	0.202	9.390	0.000	0.040	94.285	0.262	0.403	1.87	2.774	625	625
Bt-60	34.620	2.316	18.142	21.636	0.209	8.113	0.001	0.250	9.420	0.008	0.016	94.728	0.271	0.401	1.882	2.815	630	630
Bt-61	35.081	2.010	18.623	21.117	0.226	8.312	0.000	0.239	9.415	0.016	0.013	95.049	0.233	0.412	1.912	2.725	604	604
Bt-62	34.639	1.851	19.510	20.923	0.229	8.391	0.019	0.175	9.116	0.012	0.030	94.891	0.215	0.417	1.928	2.697	589	589
Bt-63	34.427	2.117	18.722	21.313	0.239	7.996	0.047	0.212	9.079	0.000	0.023	94.174	0.248	0.401	1.858	2.779	614	614
Bt-64	35.221	1.685	19.024	20.572	0.221	8.365	0.016	0.198	9.403	0.015	0.061	94.778	0.196	0.420	1.923	2.653	569	569
Bt-65	34.377	1.915	18.285	21.642	0.219	8.522	0.007	0.218	9.204	0.008	0.006	94.399	0.225	0.412	1.982	2.823	597	597
PC-1 Gneiss																		
Bt-1	35.988	3.782	14.363	22.922	0.543	7.322	0.026	0.058	9.513	0.095	0.000	94.590	0.448	0.363	1.718	3.018	706	706
Bt-2	36.049	3.284	14.268	23.496	0.617	7.842	0.000	0.064	9.670	0.115	0.000	95.379	0.387	0.373	1.832	3.08	686	686

Bt-3	36.237	3.914	15.044	20.281	0.582	8.457	0.030	0.075	9.419	0.106	0.002	94.122	0.459	0.426	1.965	2.644	717	701
	35.742	3.500	14.263	21.212	0.662	8.401	0.047	0.075	9.433	0.105	0.000	93.416	0.417	0.414	1.983	2.809	702	
	36.425	3.601	14.871	21.155	0.634	8.137	0.060	0.039	9.447	0.123	0.013	94.476	0.423	0.407	1.892	2.76	703	
	36.899	4.129	14.936	20.876	0.619	8.347	0.058	0.037	9.504	0.091	0.000	95.476	0.478	0.416	1.914	2.686	721	
	36.868	3.385	14.786	21.476	0.586	8.441	0.011	0.037	9.570	0.121	0.000	95.252	0.394	0.412	1.947	2.779	693	
	35.290	3.186	13.982	22.161	0.661	8.324	0.031	0.061	9.426	0.089	0.000	93.191	0.383	0.401	1.983	2.961	688	
	36.540	3.258	14.813	21.670	0.626	7.577	0.045	0.039	9.562	0.115	0.000	94.219	0.384	0.384	1.771	2.842	686	
Bt-4	36.361	4.083	13.937	22.095	0.744	7.865	0.042	0.030	9.506	0.102	0.028	94.769	0.481	0.388	1.836	2.894	719	719
Bt-5	35.754	3.599	14.538	22.579	0.625	7.648	0.007	0.065	9.583	0.120	0.000	94.490	0.427	0.376	1.796	2.975	701	701
Bt-6	36.686	3.198	16.593	21.099	0.619	6.639	0.051	0.079	8.116	0.108	0.000	93.163	0.376	0.359	1.545	2.755	680	680
Bt-7	36.440	4.345	14.599	23.305	0.678	6.514	0.003	0.070	9.444	0.106	0.000	95.479	0.51	0.333	1.514	3.039	722	722
Bt-8	35.235	3.403	14.193	24.390	0.580	7.123	0.092	0.044	8.651	0.117	0.001	93.803	0.409	0.342	1.695	3.255	691	691
Bt-9	36.641	3.601	14.683	22.524	0.577	7.575	0.000	0.013	9.710	0.094	0.004	95.401	0.421	0.375	1.756	2.929	699	699
Bt-10	35.827	3.319	14.118	23.746	0.521	7.720	0.000	0.109	9.567	0.091	0.000	94.998	0.393	0.367	1.813	3.129	688	690
	35.848	3.414	14.196	23.820	0.596	7.979	0.000	0.109	9.445	0.101	0.000	95.485	0.403	0.374	1.864	3.122	692	
Bt-11	35.462	3.959	14.127	23.928	0.666	7.368	0.018	0.077	9.649	0.100	0.000	95.331	0.469	0.354	1.73	3.152	712	712
Bt-12	35.022	3.816	14.184	23.847	0.587	7.519	0.021	0.072	9.504	0.090	0.000	94.640	0.455	0.360	1.778	3.164	708	708
Bt-13	35.166	4.126	14.395	23.530	0.644	7.318	0.009	0.090	9.478	0.083	0.000	94.821	0.49	0.357	1.723	3.109	719	719
Bt-14	37.408	3.616	14.985	23.635	0.581	7.705	0.007	0.051	9.161	0.078	0.000	97.209	0.415	0.367	1.75	3.012	696	696
Bt-15	35.702	3.972	14.193	23.441	0.640	7.371	0.037	0.094	9.160	0.099	0.000	94.687	0.471	0.359	1.732	3.09	713	713
Bt-16	36.124	3.896	14.152	23.138	0.632	7.607	0.000	0.051	9.562	0.100	0.000	95.239	0.459	0.370	1.776	3.03	711	711
Bt-17	36.402	4.184	14.156	23.583	0.636	7.650	0.008	0.077	9.506	0.092	0.000	96.275	0.488	0.366	1.768	3.057	719	719
PC-2 Gneiss																		
Bt-1	35.183	3.687	14.801	23.205	0.820	6.085	0.211	0.091	9.077	0.038	0.000	93.190	0.444	0.319	1.453	3.108	701	699
	36.816	3.688	15.390	23.285	0.824	6.480	0.025	0.093	9.587	0.031	0.000	96.212	0.429	0.332	1.492	3.007	697	
Bt-2	35.359	3.994	15.149	22.485	0.938	6.713	0.050	0.121	9.521	0.052	0.000	94.371	0.474	0.347	1.58	2.969	713	713
Bt-3	35.533	3.377	14.776	23.895	0.807	6.375	0.000	0.131	9.540	0.045	0.000	94.469	0.403	0.322	1.508	3.171	687	687
Bt-4	35.619	3.647	15.150	23.237	0.705	6.480	0.030	0.065	9.692	0.041	0.052	94.708	0.433	0.332	1.524	3.065	699	694
	35.632	3.394	15.162	23.143	0.813	6.453	0.022	0.067	9.597	0.046	0.000	94.319	0.404	0.332	1.522	3.062	688	
Bt-5	35.783	3.689	15.036	23.561	0.704	6.000	0.021	0.107	9.639	0.038	0.000	94.569	0.439	0.312	1.414	3.114	699	686
	36.378	3.365	15.219	23.785	0.821	5.923	0.038	0.085	9.476	0.042	0.001	95.124	0.397	0.308	1.385	3.119	684	
	35.365	3.485	15.112	24.034	0.730	6.215	0.072	0.123	8.798	0.037	0.000	93.962	0.417	0.316	1.472	3.193	692	

	36.051	3.475	15.491	24.029	0.808	6.042	0.003	0.130	9.649	0.044	0.026	95.739	0.409	0.310	1.408	3.14	688	
	35.355	3.320	15.191	24.500	0.764	6.190	0.024	0.113	8.991	0.046	0.000	94.483	0.396	0.311	1.463	3.248	684	
	36.114	3.547	14.956	24.071	0.831	5.861	0.004	0.083	9.609	0.047	0.000	95.113	0.42	0.303	1.375	3.168	692	
	35.719	2.962	15.115	24.941	0.824	6.359	0.035	0.110	9.062	0.018	0.016	95.155	0.351	0.312	1.494	3.288	665	
Bt-6	35.495	3.500	14.867	24.249	0.836	6.423	0.045	0.121	9.548	0.043	0.009	95.125	0.416	0.321	1.512	3.202	692	692
Bt-7	36.361	2.982	15.177	24.137	0.907	6.472	0.000	0.085	9.672	0.049	0.000	95.829	0.35	0.323	1.507	3.152	665	665
Bt-8	35.168	3.282	14.794	23.472	0.855	6.728	0.069	0.099	9.267	0.038	0.000	93.763	0.394	0.338	1.6	3.132	685	687
	35.701	3.352	14.966	23.511	0.852	6.429	0.049	0.109	9.545	0.038	0.000	94.543	0.399	0.328	1.516	3.109	686	
	36.372	3.530	15.185	23.622	0.855	6.767	0.036	0.037	9.690	0.041	0.000	96.127	0.412	0.338	1.566	3.067	692	
	36.905	3.428	15.523	23.242	0.830	6.686	0.036	0.084	9.595	0.038	0.000	96.358	0.397	0.339	1.536	2.995	686	
	35.627	3.449	15.099	23.105	0.854	6.731	0.046	0.121	9.535	0.037	0.000	94.596	0.409	0.342	1.583	3.048	691	
	36.740	3.506	15.436	23.029	0.877	6.885	0.043	0.056	9.469	0.035	0.001	96.067	0.407	0.348	1.585	2.974	691	
	36.168	3.473	15.103	23.210	0.918	6.572	0.005	0.076	9.605	0.034	0.002	95.159	0.409	0.336	1.535	3.04	691	
	36.305	3.376	15.021	23.369	0.891	6.700	0.000	0.104	9.718	0.050	0.009	95.533	0.397	0.338	1.56	3.053	686	
	35.428	3.368	14.797	23.211	0.863	6.487	0.058	0.024	9.604	0.040	0.000	93.871	0.404	0.332	1.54	3.092	688	
	36.343	3.188	15.064	23.655	0.857	6.627	0.008	0.077	9.643	0.029	0.000	95.482	0.375	0.333	1.544	3.093	677	
	36.044	3.180	14.733	23.503	0.956	6.476	0.007	0.071	9.357	0.042	0.000	94.359	0.378	0.329	1.527	3.109	678	
Bt-9	35.616	3.514	14.922	22.819	0.861	6.683	0.000	0.089	9.584	0.044	0.000	94.122	0.419	0.343	1.578	3.023	695	686
	35.921	3.455	15.207	23.137	0.808	6.822	0.014	0.082	9.580	0.050	0.000	95.063	0.407	0.344	1.594	3.033	691	
	35.544	3.318	14.908	23.129	0.801	6.974	0.000	0.114	9.526	0.041	0.012	94.358	0.395	0.350	1.645	3.061	687	
	36.008	2.996	15.325	22.700	0.772	6.984	0.000	0.024	9.634	0.047	0.008	94.488	0.355	0.354	1.638	2.987	670	
Bt-10	35.126	3.238	14.927	22.679	0.803	6.773	0.017	0.134	9.464	0.036	0.000	93.187	0.39	0.347	1.616	3.036	684	694
	35.345	3.740	14.840	22.835	0.787	6.830	0.012	0.092	9.531	0.025	0.000	94.031	0.446	0.348	1.615	3.03	704	
Bt-11	35.486	2.852	15.567	24.900	0.810	6.740	0.017	0.076	10.569	0.000	0.014	97.029	0.334	0.326	1.566	3.245	658	651
	35.488	2.662	15.594	24.834	0.872	6.975	0.005	0.087	10.626	0.000	0.031	97.166	0.312	0.334	1.619	3.233	647	
	35.656	2.709	15.600	24.918	0.806	7.030	0.004	0.079	10.448	0.000	0.031	97.275	0.316	0.335	1.627	3.235	649	
Bt-12	35.398	2.872	15.537	25.428	0.943	6.457	0.209	0.261	10.427	0.043	0.078	97.635	0.336	0.312	1.498	3.309	657	661
	35.936	3.143	15.763	25.308	0.831	6.670	0.038	0.097	10.493	0.033	0.047	98.348	0.363	0.320	1.529	3.254	671	
	35.730	2.822	15.559	25.833	0.882	6.493	0.000	0.091	10.493	0.000	0.049	97.941	0.329	0.309	1.499	3.347	654	
Bt-13	35.353	3.038	16.699	23.715	0.846	5.624	0.201	0.090	9.883	0.000	0.028	95.471	0.358	0.297	1.314	3.109	667	667
Bt-14	34.606	2.957	16.027	25.042	0.898	5.842	0.092	0.079	10.329	0.000	0.073	95.929	0.352	0.294	1.377	3.311	664	667
	33.792	3.131	15.706	23.852	0.812	5.784	0.063	0.054	10.160	0.000	0.084	93.420	0.381	0.302	1.396	3.229	677	

	34.946	3.003	15.960	24.151	0.797	6.417	0.004	0.067	10.427	0.000	0.072	95.828	0.356	0.321	1.506	3.179	668	
	35.211	2.907	15.713	25.045	0.860	6.606	0.018	0.066	10.432	0.000	0.056	96.901	0.342	0.320	1.538	3.272	661	
Bt-15	35.419	2.918	16.272	24.405	0.854	6.094	0.053	0.060	10.406	0.007	0.057	96.533	0.343	0.308	1.418	3.185	661	661
Bt-16	34.387	3.084	15.594	23.349	0.775	6.014	0.043	0.113	10.092	0.013	0.089	93.533	0.373	0.315	1.443	3.142	675	675
Bt-17	35.012	2.919	16.450	23.266	0.778	5.988	0.024	0.111	10.121	0.004	0.068	94.728	0.347	0.315	1.412	3.077	663	662
	34.374	2.871	16.160	23.045	0.819	5.932	0.046	0.056	10.137	0.000	0.097	93.517	0.347	0.315	1.42	3.094	663	
	35.391	2.872	16.444	22.741	0.777	6.132	0.058	0.111	10.016	0.000	0.091	94.612	0.341	0.325	1.441	2.998	661	
	35.306	2.908	16.048	23.579	0.864	6.366	0.068	0.125	10.075	0.008	0.099	95.423	0.344	0.325	1.492	3.101	662	
	35.468	2.843	15.959	23.556	0.861	6.275	0.040	0.127	10.095	0.001	0.078	95.285	0.336	0.322	1.472	3.1	658	
Bt-18	35.513	3.118	15.979	25.067	0.839	6.742	0.021	0.133	10.363	0.008	0.040	97.814	0.362	0.324	1.552	3.238	671	667
	35.502	2.963	15.675	25.363	0.858	6.194	0.070	0.120	10.376	0.000	0.068	97.173	0.347	0.303	1.439	3.306	662	
	35.647	3.083	15.624	25.218	0.859	6.292	0.035	0.065	10.427	0.016	0.069	97.319	0.361	0.308	1.458	3.279	669	
Bt-19	35.678	2.939	15.910	25.413	0.869	6.272	0.007	0.013	10.595	0.000	0.061	97.743	0.342	0.305	1.448	3.292	660	660
	35.491	2.900	15.804	24.446	0.780	6.135	0.028	0.030	10.366	0.000	0.065	96.031	0.342	0.309	1.435	3.208	660	
Bt-20	35.944	3.022	16.486	24.048	0.767	6.600	0.034	0.028	10.235	0.000	0.056	97.207	0.35	0.328	1.516	3.099	666	669
	35.456	3.055	16.069	24.584	0.754	6.270	0.043	0.106	10.274	0.012	0.062	96.670	0.358	0.313	1.457	3.204	668	
	35.815	3.107	16.472	24.536	0.801	6.224	0.068	0.110	10.184	0.012	0.066	97.378	0.361	0.311	1.432	3.166	669	
	35.272	3.151	15.981	24.439	0.778	5.957	0.010	0.070	10.409	0.000	0.068	96.121	0.372	0.303	1.393	3.206	673	
Bt-21	36.415	3.160	16.383	23.984	0.799	7.045	0.061	0.085	10.279	0.007	0.046	98.254	0.362	0.344	1.599	3.054	672	672
Bt-22	34.922	3.165	15.947	24.036	0.823	6.459	0.048	0.070	10.321	0.000	0.051	95.831	0.374	0.324	1.514	3.16	676	684
	35.434	3.470	15.887	24.546	0.856	6.716	0.017	0.074	10.550	0.000	0.046	97.587	0.404	0.328	1.548	3.175	688	
	35.105	3.536	15.739	24.043	0.837	6.382	0.038	0.099	10.518	0.014	0.036	96.339	0.416	0.321	1.489	3.148	692	
	35.173	3.727	15.617	23.345	0.847	6.049	0.073	0.081	10.130	0.011	0.046	95.088	0.442	0.316	1.423	3.08	700	
	35.367	3.160	15.469	24.508	0.834	6.795	0.002	0.070	10.647	0.004	0.057	96.900	0.371	0.331	1.58	3.197	675	
	35.509	3.187	15.635	24.758	0.905	6.590	0.002	0.056	10.704	0.000	0.037	97.374	0.372	0.322	1.526	3.216	675	
	35.833	3.216	15.670	24.570	0.871	6.505	0.000	0.055	10.584	0.015	0.052	97.360	0.375	0.321	1.502	3.184	676	
	34.521	3.380	15.393	24.281	0.873	5.923	0.068	0.100	10.284	0.013	0.041	94.866	0.406	0.303	1.408	3.239	687	
Bt-23	35.211	3.071	15.931	24.860	0.799	6.330	0.000	0.107	10.645	0.007	0.058	97.007	0.361	0.312	1.472	3.244	669	650
	34.699	2.408	15.469	25.354	0.790	6.574	0.000	0.105	10.641	0.021	0.050	96.099	0.287	0.316	1.552	3.358	631	
Bt-24	34.261	3.000	15.622	24.812	0.861	5.916	0.007	0.088	10.470	0.000	0.044	95.071	0.361	0.298	1.409	3.315	668	658
	34.178	2.669	16.422	25.611	0.867	6.492	0.068	0.107	8.980	0.000	0.055	95.438	0.317	0.311	1.53	3.387	648	
Bt-25	35.754	3.330	16.089	23.998	0.857	6.379	0.000	0.074	10.507	0.000	0.064	97.036	0.388	0.321	1.473	3.109	681	681

Bt-26	37.238	3.916	16.748	23.505	0.944	6.796	0.028	0.156	10.458	0.000	0.041	99.821	0.44	0.340	1.512	2.934	702	702
Bt-27	35.290	2.992	15.668	24.628	0.814	6.240	0.000	0.089	10.494	0.000	0.057	96.260	0.353	0.311	1.46	3.233	666	670
	35.240	3.127	15.476	25.191	0.785	6.294	0.000	0.048	10.708	0.003	0.063	96.920	0.368	0.308	1.469	3.298	672	
	35.348	3.190	15.591	24.787	0.837	6.308	0.000	0.073	10.529	0.000	0.079	96.724	0.375	0.312	1.47	3.242	675	
	35.372	3.046	15.402	25.001	0.832	6.178	0.012	0.061	10.538	0.013	0.061	96.501	0.36	0.306	1.445	3.282	668	
Bt-28	35.247	2.986	15.479	25.178	0.800	6.494	0.000	0.063	10.542	0.000	0.040	96.819	0.352	0.315	1.515	3.296	665	668
	35.536	3.073	15.478	24.648	0.769	6.301	0.000	0.109	10.564	0.000	0.058	96.521	0.362	0.313	1.47	3.226	670	
Bt-29	34.766	2.952	15.446	25.039	0.913	6.313	0.009	0.082	10.538	0.002	0.023	96.077	0.351	0.310	1.487	3.309	665	665
	34.330	2.967	15.239	25.169	0.932	6.153	0.014	0.056	10.507	0.000	0.036	95.394	0.356	0.304	1.464	3.359	666	
	34.525	3.076	15.269	24.930	0.889	6.223	0.016	0.065	10.418	0.000	0.025	95.430	0.368	0.308	1.476	3.317	672	
	34.713	2.992	15.506	25.257	0.861	6.269	0.003	0.069	10.355	0.000	0.033	96.051	0.356	0.307	1.477	3.338	667	
	35.784	3.031	15.908	24.546	0.956	6.505	0.000	0.086	10.243	0.018	0.062	97.126	0.354	0.321	1.503	3.183	667	
	34.187	2.695	14.979	25.166	0.828	6.306	0.047	0.071	10.316	0.012	0.041	94.638	0.326 0	0.309	1.512	3.386	652	
PC-3 Gneiss																		
Bt-1	36.362	3.586	15.568	22.833	0.802	6.525	0.042	0.232	9.459	0.028	0.010	95.440	0.42	0.337	1.513	2.97	695	690
	36.229	3.321	15.266	22.766	0.771	6.621	0.069	0.078	9.599	0.025	0.000	94.739	0.392	0.341	1.548	2.986	685	
	23.319	21.887	14.956	23.396	6.178	3.183	0.110	0.179	3.469	0.017	0.000	96.690	2.624	0.195	0.756	3.118	895	895
Bt-2	35.639	3.737	15.617	23.529	0.733	6.770	0.233	0.115	8.413	0.029	0.009	94.817	0.44	0.339	1.579	3.078	702	703
Bt-3	36.503	3.305	15.438	24.208	0.831	6.471	0.082	0.113	9.379	0.026	0.005	96.356	0.385	0.323	1.494	3.136	680	676
	36.654	3.119	15.308	23.849	0.770	6.816	0.044	0.141	9.577	0.027	0.005	96.302	0.363	0.337	1.573	3.088	672	
Bt-4	35.671	3.226	15.230	23.524	0.864	6.673	0.035	0.098	9.343	0.027	0.016	94.699	0.383	0.336	1.568	3.101	681	681
Bt-5	36.055	1.209	16.949	21.042	0.942	9.625	0.133	0.135	7.348	0.014	0.012	93.461	0.141	0.449	2.229	2.734	493	517
	36.320	1.450	15.961	20.190	0.983	8.737	0.025	0.137	9.514	0.026	0.013	93.349	0.171	0.436	2.047	2.653	541	
Bt-6	35.811	3.420	15.447	22.589	0.629	6.247	0.166	0.245	9.208	0.027	0.011	93.792	0.407	0.330	1.473	2.988	689	689
Bt-7	36.884	3.538	15.655	22.611	0.704	6.656	0.001	0.148	9.678	0.015	0.007	95.894	0.411	0.344	1.532	2.919	692	691
	37.086	3.494	15.673	22.922	0.781	6.814	0.023	0.141	9.562	0.015	0.005	96.513	0.403	0.346	1.559	2.941	689	
	36.851	3.505	15.642	22.129	0.738	6.951	0.035	0.158	9.613	0.024	0.003	95.644	0.407	0.359	1.6	2.858	692	
Bt-8	36.677	3.739	15.838	22.285	0.745	6.659	0.081	0.166	9.656	0.023	0.000	95.865	0.434	0.348	1.532	2.876	700	700
Bt-9	36.634	3.521	15.115	22.977	0.820	6.714	0.024	0.108	9.541	0.031	0.000	95.478	0.412	0.342	1.557	2.989	692	692
Bt-10	36.165	1.961	15.382	22.552	0.706	7.485	0.051	0.138	9.420	0.027	0.036	93.917	0.233	0.372	1.762	2.979	597	597
Bt-11	36.979	1.869	16.044	21.915	0.737	7.466	0.009	0.077	9.595	0.019	0.036	94.741	0.219	0.378	1.731	2.851	586	586

Bt-12	38.115	1.806	16.820	22.234	0.761	7.671	0.035	0.144	9.517	0.035	0.000	97.129	0.205	0.381	1.728	2.81	572	572
Bt-13	36.739	2.146	16.247	21.885	0.745	7.449	0.023	0.164	9.596	0.029	0.009	95.025	0.25	0.378	1.723	2.84	612	609
	36.383	2.059	16.088	21.818	0.720	7.646	0.055	0.186	9.563	0.034	0.000	94.545	0.242	0.385	1.78	2.849	607	
Bt-14	36.340	1.906	15.868	22.795	0.735	7.510	0.052	0.149	9.548	0.038	0.000	94.932	0.224	0.370	1.75	2.979	589	589
Bt-15	36.420	2.318	15.971	22.341	0.744	7.460	0.000	0.169	9.532	0.035	0.000	94.981	0.272	0.373	1.732	2.91	627	599
	36.321	1.802	15.643	22.797	0.720	7.446	0.030	0.085	9.548	0.027	0.000	94.413	0.213	0.368	1.745	2.996	578	
	36.733	1.921	15.742	22.905	0.702	7.681	0.032	0.131	9.559	0.020	0.000	95.420	0.224	0.374	1.778	2.975	590	
	36.962	2.028	16.102	22.770	0.735	7.589	0.032	0.114	9.535	0.027	0.000	95.886	0.235	0.373	1.745	2.937	599	
Bt-16	36.258	2.072	15.623	22.675	0.777	7.290	0.029	0.160	9.576	0.022	0.000	94.478	0.245	0.364	1.707	2.979	606	598
	36.383	1.914	15.701	22.876	0.794	7.424	0.035	0.199	9.605	0.029	0.000	94.954	0.225	0.366	1.731	2.993	590	
Bt-17	36.733	3.373	15.743	22.927	0.657	6.269	0.038	0.153	9.609	0.026	0.000	95.522	0.394	0.328	1.45	2.975	684	684
Bt-18	36.776	3.332	15.324	23.163	0.756	6.648	0.033	0.080	9.712	0.033	0.000	95.850	0.389	0.338	1.537	3.004	683	682
	36.204	3.231	14.845	23.572	0.767	6.618	0.025	0.066	9.661	0.033	0.000	95.013	0.382	0.333	1.55	3.098	680	
	35.929	3.252	14.827	23.459	0.737	6.788	0.034	0.122	9.617	0.045	0.000	94.799	0.386	0.340	1.595	3.091	682	
	36.192	3.248	15.162	23.198	0.800	6.895	0.041	0.187	9.468	0.033	0.000	95.218	0.382	0.346	1.607	3.034	681	
Bt-19	36.736	3.438	15.437	23.247	0.871	6.641	0.055	0.116	9.445	0.024	0.000	96.006	0.4	0.337	1.532	3.008	687	687
Bt-20	36.618	3.318	15.679	22.568	0.756	6.489	0.006	0.065	9.669	0.020	0.000	95.184	0.388	0.339	1.505	2.937	683	683
Bt-21	35.323	3.382	15.055	22.970	0.771	6.833	0.050	0.174	9.480	0.039	0.000	94.068	0.404	0.346	1.616	3.048	690	686
	37.020	3.270	15.971	22.805	0.820	6.710	0.050	0.104	9.607	0.023	0.000	96.375	0.378	0.344	1.536	2.929	679	
	36.258	3.451	15.686	22.651	0.770	6.684	0.036	0.145	9.586	0.028	0.003	95.294	0.404	0.345	1.552	2.95	690	
Bt-22	36.615	3.616	15.733	22.812	0.811	6.396	0.191	0.356	8.957	0.028	0.000	95.509	0.421	0.333	1.477	2.955	695	695
Bt-23	34.664	3.147	15.777	24.457	0.713	6.903	0.073	0.139	7.960	0.025	0.000	93.850	0.376	0.335	1.634	3.247	678	678
Bt-24	35.912	3.927	15.396	22.753	0.725	6.913	0.202	0.120	8.839	0.014	0.000	94.797	0.461	0.351	1.609	2.972	709	709
Bt-25	35.167	3.725	14.998	23.029	0.802	6.419	0.123	0.147	9.369	0.020	0.000	93.796	0.446	0.332	1.523	3.066	703	703
Bt-26	35.869	3.422	15.513	23.137	0.784	6.517	0.046	0.101	9.308	0.034	0.014	94.735	0.404	0.334	1.525	3.038	689	689
Bt-27	36.036	3.791	15.312	23.008	0.847	6.414	0.048	0.049	9.602	0.018	0.018	95.138	0.446	0.332	1.496	3.011	703	703
Bt-28	36.995	3.573	15.675	23.478	0.849	6.592	0.065	0.144	9.372	0.021	0.032	96.793	0.412	0.334	1.507	3.011	691	691
Bt-29	36.373	3.473	15.318	23.583	0.893	6.633	0.001	0.162	9.662	0.037	0.007	96.132	0.406	0.334	1.535	3.061	689	689
Bt-30	36.732	3.122	15.419	23.758	0.816	7.317	0.057	0.246	9.418	0.020	0.017	96.916	0.361	0.354	1.676	3.053	673	685
	35.359	3.615	14.738	23.664	0.812	6.373	0.060	0.162	9.383	0.036	0.028	94.223	0.432	0.324	1.51	3.146	698	
Bt-31	36.840	3.301	15.300	23.659	0.816	6.708	0.000	0.103	9.599	0.044	0.008	96.368	0.384	0.336	1.545	3.057	681	689
	34.625	3.538	14.613	23.619	0.847	6.298	0.046	0.150	9.551	0.043	0.014	93.334	0.429	0.322	1.513	3.182	697	

Bt-32	35.795	3.800	15.242	22.722	0.818	6.561	0.075	0.094	9.272	0.030	0.013	94.415	0.45	0.340	1.539	2.99	705	705
Bt-33	36.402	3.058	15.026	23.816	0.745	6.708	0.066	0.149	9.390	0.027	0.000	95.381	0.36	0.334	1.563	3.114	671	671
	36.619	3.076	15.381	23.751	0.683	6.596	0.071	0.113	9.566	0.036	0.000	95.884	0.36	0.331	1.527	3.086	670	
Bt-34	36.703	2.967	15.842	23.874	0.717	6.598	0.000	0.079	9.675	0.029	0.014	96.490	0.344	0.330	1.518	3.082	663	663
Bt-35	36.489	3.727	15.173	23.069	0.833	6.861	0.031	0.101	9.628	0.029	0.000	95.933	0.435	0.347	1.586	2.991	701	705
	36.542	3.928	15.016	22.785	0.872	6.700	0.009	0.093	9.441	0.024	0.000	95.404	0.46	0.344	1.554	2.964	709	
Bt-36	35.261	4.104	15.264	23.039	0.950	6.340	0.063	0.150	9.545	0.023	0.000	94.733	0.487	0.329	1.49	3.039	715	718
	35.760	4.287	15.253	23.200	0.901	6.529	0.041	0.116	9.515	0.009	0.005	95.613	0.503	0.334	1.518	3.026	720	
Bt-37	35.761	1.802	15.525	22.406	0.755	7.572	0.117	0.068	9.008	0.039	0.048	93.091	0.216	0.376	1.796	2.981	583	594
	35.887	2.037	14.775	23.035	0.846	7.846	0.074	0.137	9.333	0.044	0.000	94.003	0.243	0.378	1.854	3.053	607	
	36.426	1.958	15.433	22.378	0.821	7.568	0.067	0.083	9.323	0.046	0.000	94.092	0.232	0.376	1.774	2.944	597	
	35.629	2.072	15.130	22.595	0.758	7.494	0.087	0.098	9.422	0.042	0.000	93.318	0.248	0.372	1.781	3.012	610	
Bt-38	36.243	2.301	15.010	22.458	0.837	7.519	0.083	0.155	9.362	0.044	0.011	94.011	0.273	0.374	1.769	2.964	628	628
Bt-39	36.491	2.869	16.117	22.482	0.671	7.008	0.060	0.085	9.504	0.027	0.000	95.308	0.335	0.357	1.621	2.917	661	661
Bt-40	36.647	2.448	15.264	23.168	0.758	7.349	0.006	0.129	9.661	0.036	0.000	95.459	0.287	0.361	1.707	3.018	635	635
Bt-41	36.294	2.301	15.192	22.551	0.772	7.238	0.027	0.123	9.531	0.026	0.014	94.063	0.273	0.364	1.702	2.976	627	627
Bt-42	36.344	2.188	15.302	23.110	0.710	7.226	0.068	0.148	9.470	0.042	0.017	94.614	0.259	0.358	1.693	3.037	616	616
Bt-43	35.541	3.446	15.372	23.443	0.846	6.627	0.065	0.175	9.458	0.024	0.000	94.991	0.408	0.335	1.553	3.083	690	690
Bt-44	35.397	3.757	15.574	22.991	0.795	6.450	0.024	0.149	9.431	0.035	0.000	94.595	0.445	0.333	1.514	3.028	703	703
Bt-45	35.460	2.988	15.268	23.195	0.815	6.427	0.052	0.157	9.430	0.035	0.014	93.832	0.358	0.331	1.524	3.086	669	667
	36.730	3.005	15.630	23.729	0.860	6.422	0.034	0.174	9.463	0.021	0.005	96.069	0.35	0.325	1.483	3.074	665	
Bt-46	35.606	3.129	15.377	23.677	0.755	6.435	0.000	0.000	9.547	0.027	0.000	94.547	0.372	0.326	1.516	3.129	675	675
Bt-47	35.947	3.365	15.029	23.517	0.830	6.672	0.042	0.000	9.464	0.033	0.000	94.891	0.398	0.336	1.564	3.092	686	686
Bt-48	35.833	3.305	15.060	23.524	0.814	6.803	0.011	0.109	9.588	0.022	0.000	95.064	0.391	0.340	1.594	3.092	684	684
Bt-49	35.683	3.218	15.298	24.367	0.785	6.701	0.027	0.111	9.508	0.022	0.003	95.718	0.379	0.329	1.564	3.191	678	678
Bt-50	35.646	3.295	15.476	23.425	0.747	6.671	0.060	0.180	9.382	0.025	0.008	94.908	0.389	0.337	1.563	3.079	683	683
Bt-51	35.554	3.287	15.050	23.916	0.818	6.706	0.068	0.160	9.386	0.030	0.031	94.998	0.39	0.333	1.576	3.153	683	683
Bt-52	36.016	3.771	15.271	23.300	0.882	6.762	0.013	0.128	9.593	0.032	0.010	95.771	0.442	0.341	1.57	3.035	702	702
Bt-53	35.986	3.636	15.212	23.407	0.905	6.660	0.037	0.148	9.512	0.025	0.000	95.522	0.427	0.337	1.551	3.057	697	697
Bt-54	35.742	3.685	15.125	23.130	0.816	6.622	0.023	0.045	9.498	0.028	0.000	94.707	0.436	0.338	1.554	3.044	700	704
	36.086	3.908	15.332	22.684	0.848	6.787	0.003	0.026	9.736	0.028	0.012	95.443	0.458	0.348	1.576	2.956	708	
Bt-55	36.121	3.707	15.287	23.164	0.860	6.658	0.041	0.056	9.659	0.030	0.000	95.577	0.435	0.339	1.547	3.02	700	700

Bt-56	36.073	3.060	14.919	23.792	0.867	6.728	0.000	0.100	9.581	0.024	0.018	95.156	0.362	0.335	1.576	3.127	672	672
Bt-57	34.795	3.015	14.771	23.773	0.837	6.530	0.010	0.112	9.579	0.028	0.008	93.451	0.365	0.329	1.566	3.198	672	677
	35.417	3.245	15.284	23.867	0.833	6.394	0.054	0.092	9.536	0.016	0.000	94.734	0.386	0.323	1.507	3.155	681	
Bt-58	36.269	2.182	15.830	21.446	0.883	8.090	0.104	0.156	9.327	0.024	0.000	94.307	0.257	0.402	1.885	2.803	621	621
Bt-59	36.490	2.350	15.909	21.338	0.872	8.506	0.073	0.176	9.500	0.032	0.013	95.251	0.273	0.415	1.962	2.761	634	634
Bt-60	35.945	2.156	15.604	21.677	0.884	8.012	0.076	0.195	9.614	0.024	0.000	94.180	0.255	0.397	1.878	2.85	619	619
Bt-61	36.040	1.712	15.724	21.924	0.839	8.651	0.054	0.189	9.309	0.027	0.000	94.461	0.202	0.413	2.018	2.869	575	575
Bt-62	35.427	1.771	14.933	22.671	0.860	8.113	0.067	0.086	9.450	0.027	0.010	93.406	0.213	0.390	1.93	3.025	582	577
	34.886	1.676	15.321	22.315	0.851	8.443	0.079	0.089	9.523	0.020	0.000	93.197	0.202	0.403	2.013	2.984	573	
Bt-63	36.162	3.703	15.232	22.739	0.868	6.799	0.063	0.137	9.551	0.029	0.000	95.277	0.435	0.348	1.581	2.967	701	706
	35.543	3.846	15.039	22.133	0.775	6.885	0.043	0.130	9.345	0.028	0.000	93.759	0.458	0.357	1.624	2.929	709	
	35.884	3.866	15.312	22.323	0.878	7.126	0.051	0.163	9.497	0.030	0.002	95.124	0.454	0.363	1.658	2.914	708	
Bt-64	35.894	4.074	15.309	23.361	0.854	6.588	0.021	0.065	9.802	0.016	0.010	95.990	0.477	0.335	1.528	3.04	713	713
Bt-65	36.282	3.872	15.120	23.368	0.884	6.327	0.051	0.118	9.517	0.028	0.026	95.586	0.454	0.326	1.471	3.047	705	705
Bt-66	35.440	3.902	15.284	22.626	0.866	6.316	0.058	0.178	9.405	0.022	0.000	94.089	0.464	0.332	1.489	2.993	709	709
Bt-67	36.320	3.868	15.860	21.990	0.904	6.725	0.020	0.140	9.533	0.030	0.005	95.388	0.451	0.353	1.554	2.851	706	708
	36.069	3.937	15.213	22.813	0.957	6.478	0.045	0.110	9.492	0.036	0.024	95.164	0.463	0.336	1.51	2.983	709	
Bt-68	35.684	2.933	15.367	22.649	0.871	7.204	0.049	0.148	9.613	0.026	0.000	94.537	0.348	0.362	1.691	2.983	668	668
Bt-69	36.183	3.481	14.983	23.962	0.931	6.147	0.093	0.148	9.514	0.025	0.023	95.484	0.41	0.314	1.436	3.14	689	689
Bt-70	35.982	3.509	15.156	23.578	0.837	6.452	0.002	0.071	9.623	0.021	0.025	95.250	0.414	0.328	1.508	3.092	692	692
Bt-71	36.411	1.877	15.396	22.158	0.881	8.449	0.025	0.121	9.464	0.020	0.003	94.799	0.22	0.405	1.966	2.893	591	591
Bt-72	36.323	3.784	15.292	23.338	0.963	6.423	0.088	0.128	9.501	0.018	0.043	95.899	0.442	0.329	1.488	3.033	701	698
	36.623	3.633	15.519	23.908	0.869	6.640	0.044	0.153	9.493	0.019	0.031	96.927	0.42	0.331	1.523	3.075	694	
Bt-73	36.881	1.185	15.834	20.581	1.063	9.139	0.037	0.116	9.578	0.020	0.000	94.429	0.139	0.442	2.118	2.675	487	487
Bt-74	36.991	1.300	15.694	20.046	1.005	9.172	0.030	0.094	9.445	0.031	0.000	93.800	0.152	0.449	2.132	2.614	514	514
PC-21 Gneiss																		
Bt-1	33.488	2.383	15.542	26.827	0.522	5.547	0.293	0.150	8.424	0.000	0.091	93.246	0.292	0.269	1.347	3.656	630	630
Bt-2	32.946	2.843	15.625	26.211	0.698	5.157	0.148	0.085	9.865	0.000	0.058	93.623	0.35	0.260	1.257	3.585	661	661
Bt-3	37.098	2.041	16.728	25.419	0.519	5.364	0.364	1.063	8.791	0.014	0.077	97.461	0.235	0.273	1.225	3.258	588	608
	33.755	2.377	15.475	27.273	0.569	5.582	0.310	0.088	8.351	0.000	0.152	93.897	0.29	0.267	1.348	3.695	629	
Bt-4	34.745	3.653	15.537	26.446	0.764	5.844	0.073	0.159	10.086	0.020	0.054	97.368	0.43	0.283	1.363	3.461	694	692
	34.852	3.570	15.593	26.568	0.717	6.075	0.057	0.161	10.125	0.000	0.038	97.747	0.418	0.290	1.411	3.462	690	

Bt-5	33.453	2.954	15.397	26.820	0.669	5.957	0.039	0.122	9.447	0.000	0.022	94.874	0.3580	0.284	1.43	3.611	666	672
	34.724	3.309	15.562	26.919	0.736	6.248	0.034	0.121	10.307	0.000	0.038	97.988	0.388	0.293	1.452	3.51	679	
Bt-6	35.406	3.302	15.821	27.055	0.674	6.006	0.053	0.128	10.137	0.000	0.035	98.609	0.383	0.284	1.382	3.492	676	679
	35.363	3.367	15.545	26.683	0.703	6.073	0.028	0.118	10.222	0.007	0.053	98.149	0.393	0.289	1.404	3.46	681	
Bt-7	35.796	3.109	16.236	25.456	0.651	6.678	0.129	0.258	9.688	0.000	0.051	98.041	0.359	0.319	1.528	3.268	669	669
Bt-8	34.599	3.792	15.384	25.764	0.622	5.596	0.058	0.127	10.205	0.000	0.035	96.173	0.451	0.279	1.318	3.405	701	694
	35.473	3.503	15.816	26.150	0.665	5.663	0.061	0.068	10.090	0.006	0.051	97.534	0.409	0.278	1.311	3.397	686	
Bt-9	33.848	3.333	14.988	27.256	0.673	5.482	0.000	0.133	10.279	0.010	0.024	96.021	0.401	0.264	1.308	3.649	682	692
	34.151	3.597	14.720	26.906	0.642	5.606	0.000	0.102	10.335	0.000	0.079	96.121	0.432	0.271	1.334	3.592	694	
	34.165	3.747	14.961	27.173	0.689	5.442	0.004	0.107	10.458	0.000	0.072	96.802	0.447	0.263	1.288	3.607	699	
	33.932	3.483	14.980	26.906	0.661	5.569	0.000	0.065	10.352	0.000	0.071	96.002	0.419	0.269	1.327	3.597	689	
	33.772	3.693	14.864	27.238	0.748	5.582	0.000	0.116	10.375	0.001	0.057	96.432	0.443	0.268	1.328	3.636	698	
Bt-10	33.098	3.679	14.771	27.197	0.750	5.519	0.044	0.088	10.188	0.010	0.050	95.382	0.447	0.266	1.33	3.677	699	695
	33.365	3.497	14.935	27.487	0.664	5.633	0.031	0.160	10.051	0.000	0.070	95.877	0.423	0.268	1.349	3.693	691	
	33.762	3.620	14.939	27.521	0.684	5.627	0.017	0.171	10.206	0.010	0.075	96.613	0.434	0.267	1.337	3.668	695	
Bt-11	33.238	3.711	14.912	26.949	0.662	5.324	0.054	0.102	9.890	0.000	0.054	94.883	0.452	0.260	1.285	3.648	700	700
Bt-12	33.770	3.939	15.191	27.370	0.659	5.545	0.000	0.103	10.239	0.000	0.052	96.856	0.47	0.265	1.311	3.632	706	712
	33.329	4.238	15.094	27.106	0.701	5.345	0.008	0.152	10.295	0.000	0.047	96.302	0.509	0.260	1.273	3.623	717	
Bt-13	33.808	3.221	15.897	27.152	0.709	5.513	0.025	0.093	10.380	0.000	0.058	96.843	0.384	0.266	1.302	3.598	676	682
	33.273	3.424	15.451	26.922	0.714	5.625	0.042	0.087	10.158	0.000	0.058	95.739	0.413	0.271	1.345	3.612	687	
Bt-14	33.770	3.904	15.052	25.676	0.657	5.586	0.024	0.107	10.148	0.010	0.064	94.984	0.472	0.279	1.337	3.449	708	699
	34.034	3.645	15.110	25.701	0.671	5.715	0.011	0.117	10.309	0.017	0.023	95.349	0.439	0.284	1.363	3.438	697	
	34.636	3.579	15.376	26.037	0.672	5.963	0.012	0.166	10.136	0.000	0.039	96.607	0.424	0.290	1.4	3.429	692	
	34.141	3.684	15.056	25.417	0.681	5.779	0.029	0.132	10.089	0.000	0.063	95.057	0.444	0.288	1.379	3.401	699	
Bt-15	33.022	3.628	14.512	26.237	0.664	5.265	0.041	0.134	10.137	0.000	0.081	93.702	0.448	0.263	1.287	3.598	699	698
	33.758	3.696	14.846	26.195	0.677	5.490	0.032	0.157	10.161	0.000	0.082	95.075	0.448	0.272	1.318	3.527	700	
	34.970	3.767	15.598	26.589	0.671	5.821	0.035	0.176	10.345	0.000	0.059	98.017	0.441	0.281	1.349	3.458	698	
	33.240	3.602	14.590	26.574	0.628	5.551	0.029	0.090	10.057	0.016	0.054	94.420	0.441	0.271	1.346	3.615	697	
	33.510	3.667	15.065	26.680	0.700	5.627	0.040	0.096	10.282	0.011	0.048	95.715	0.442	0.273	1.346	3.579	698	
	33.756	3.661	14.976	26.229	0.683	5.686	0.037	0.132	10.057	0.012	0.054	95.273	0.442	0.279	1.361	3.521	698	
Bt-16	34.675	3.702	16.213	26.167	0.744	5.572	0.017	0.138	10.203	0.000	0.048	97.467	0.434	0.275	1.295	3.413	695	707
	34.760	4.315	16.154	25.724	0.703	5.382	0.023	0.118	10.396	0.000	0.056	97.618	0.505	0.272	1.248	3.346	717	

	36.627	4.215	17.137	24.831	0.650	4.931	0.029	0.149	10.374	0.007	0.050	98.990	0.48	0.262	1.113	3.143	709	
Bt-17	34.466	2.896	15.932	26.136	0.563	6.291	0.051	0.079	10.188	0.052	0.077	96.713	0.343	0.300	1.476	3.44	660	660
Bt-18	35.221	2.766	15.980	27.225	0.563	6.231	0.031	0.129	10.466	0.017	0.072	98.684	0.322	0.290	1.437	3.522	649	
	34.708	2.801	16.178	26.810	0.560	6.185	0.014	0.116	10.386	0.017	0.061	97.824	0.329	0.291	1.438	3.496	652	655
	35.020	3.043	16.057	26.639	0.593	5.973	0.032	0.123	10.271	0.015	0.058	97.810	0.356	0.286	1.385	3.466	665	
Bt-19	35.343	2.546	16.269	26.783	0.447	6.308	0.010	0.166	10.347	0.000	0.062	98.266	0.296	0.296	1.455	3.465	634	634
Bt-20	34.911	2.915	16.093	26.637	0.555	6.156	0.016	0.179	10.406	0.000	0.069	97.921	0.341	0.292	1.428	3.466	658	650
	34.883	2.645	16.584	26.622	0.528	6.263	0.021	0.134	10.369	0.000	0.071	98.104	0.309	0.296	1.448	3.452	642	
Bt-21	35.623	3.120	16.566	26.109	0.471	5.796	0.057	0.163	10.208	0.000	0.079	98.175	0.362	0.284	1.331	3.363	668	
	33.982	2.785	16.495	26.225	0.564	6.198	0.039	0.153	9.197	0.000	0.064	95.688	0.332	0.296	1.462	3.471	654	662
	34.931	3.060	16.077	25.890	0.553	6.402	0.000	0.141	10.381	0.002	0.085	97.503	0.358	0.306	1.486	3.371	667	
	34.407	2.843	15.704	25.869	0.449	6.234	0.007	0.080	9.933	0.000	0.067	95.579	0.34	0.300	1.475	3.434	659	
Bt-22	35.013	3.135	16.219	26.235	0.505	6.063	0.010	0.090	10.338	0.010	0.061	97.664	0.367	0.292	1.405	3.411	670	670

Appendix IV. Isopleths of X(Mg) for andalusite phyllite (PC-10) and gneisses (PC-1, -2, -3, 21)

(a) Isopleths of X(Mg) for PC-10 andalusite phyllite.

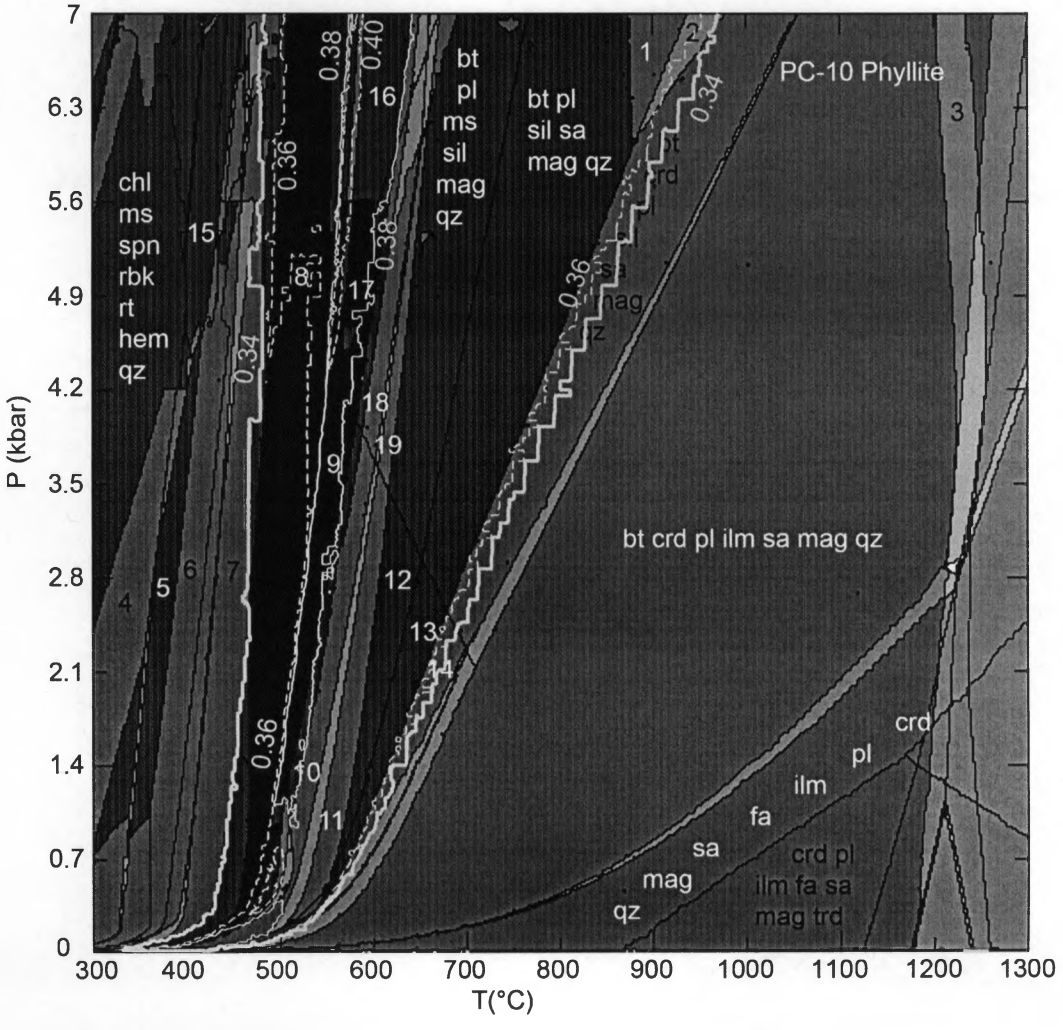

1 - bt pl grt sil sa mag qz
2 - bt crd pl grt sil sa mag qz
3 - bt crd pl ilm grt sa mag qz
4 - chl ms spn rbk ab rt hem qz
5 - chl ms spn ab rt mag qz
6 - bt chl ms spn ab rt mag qz
7 - bt chl pl ms ilm rt mag qz
8 - bt chl ms ilm mag qz
9 - bt ms ilm and mag qz
10 - bt pl ms ilm and mag qz
11 - bt pl ms and rt mag qz
12 - bt pl ms and mag qz
13 - bt pl and sa mag qz
14 - bt crd pl and sa mag qz
15 - chl ms amp spn rt mag qz
16 - bt ms ilm grt ky mag qz
17 - bt ms ilm sil mag qz
18 - bt pl ms ilm sil mag qz
19 - bt pl ms sil ru mag qz

(b) Isopleths of X(Mg) for PC-1 gneiss.

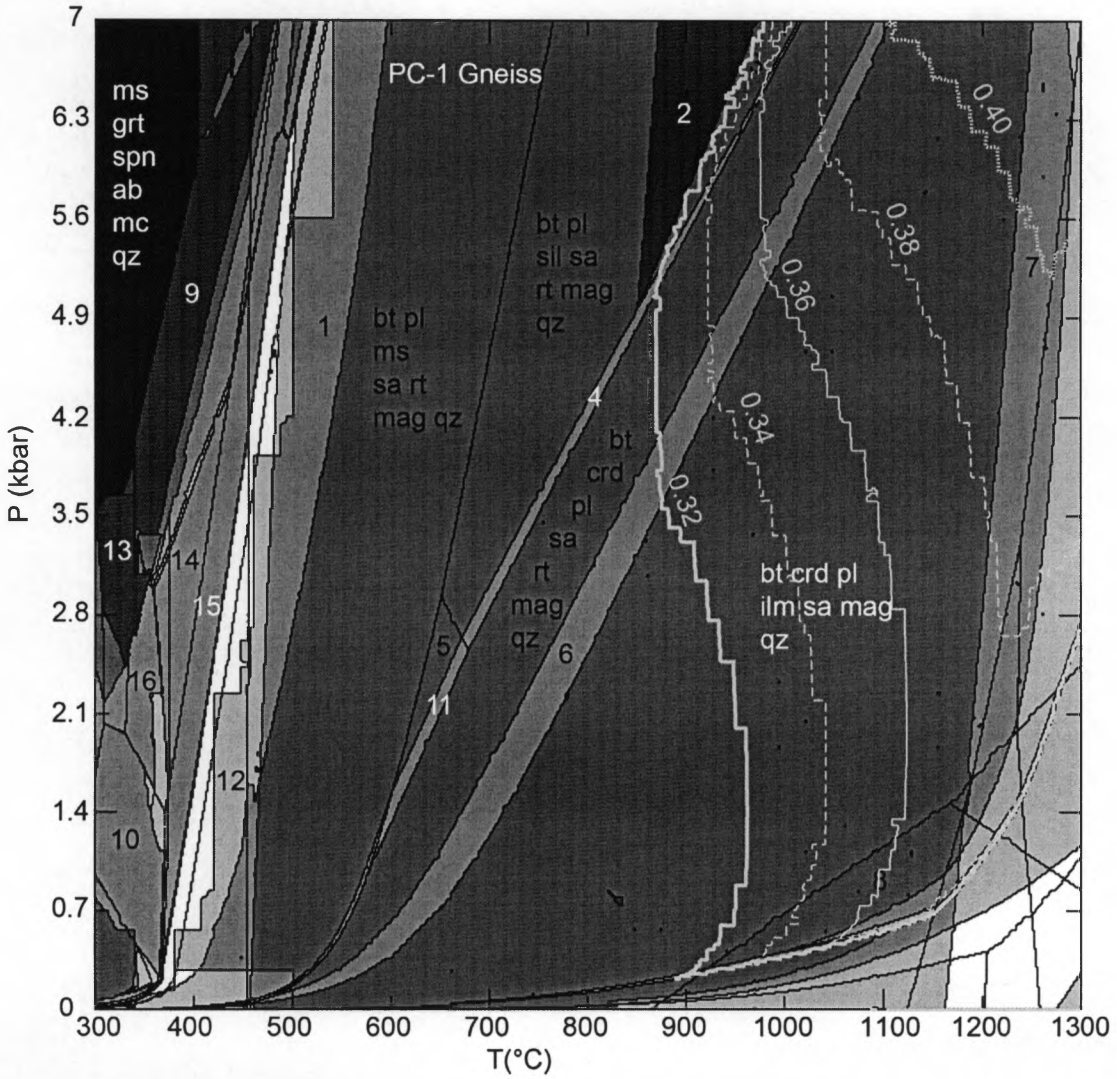

1 - bt pl ms sa rt hem mag qz
2 - bt pl sil sa mag qz
3 - bt crd pl sil sa mag qz
4 - bt crd pl sil sa rt mag qz
5 - bt pl and sa rt mag qz
6 - bt crd pl ilm sa rt mag qz
7 - bt crd pl ilm sa mag abL qz
8 - bt crd pl ilm sa mag trd
9 - ms grt cpx spn ab mc qz
10 - chl ms grt ep spn ab mc wrk qz
11 - bt crd pl and sa rt mag qz
12 - bt pl ms ab mc rt hem mag qz
13 - chl ms grt spn ab mc qz
14 - bt ms grt zo ep spn ab mc qz
15 - bt pl ms grt ep spn ab mc qz
16 - chl ms grt czo ep spn ab mc qz

(c) Isopleths of X(Mg) for PC-2 gneiss.

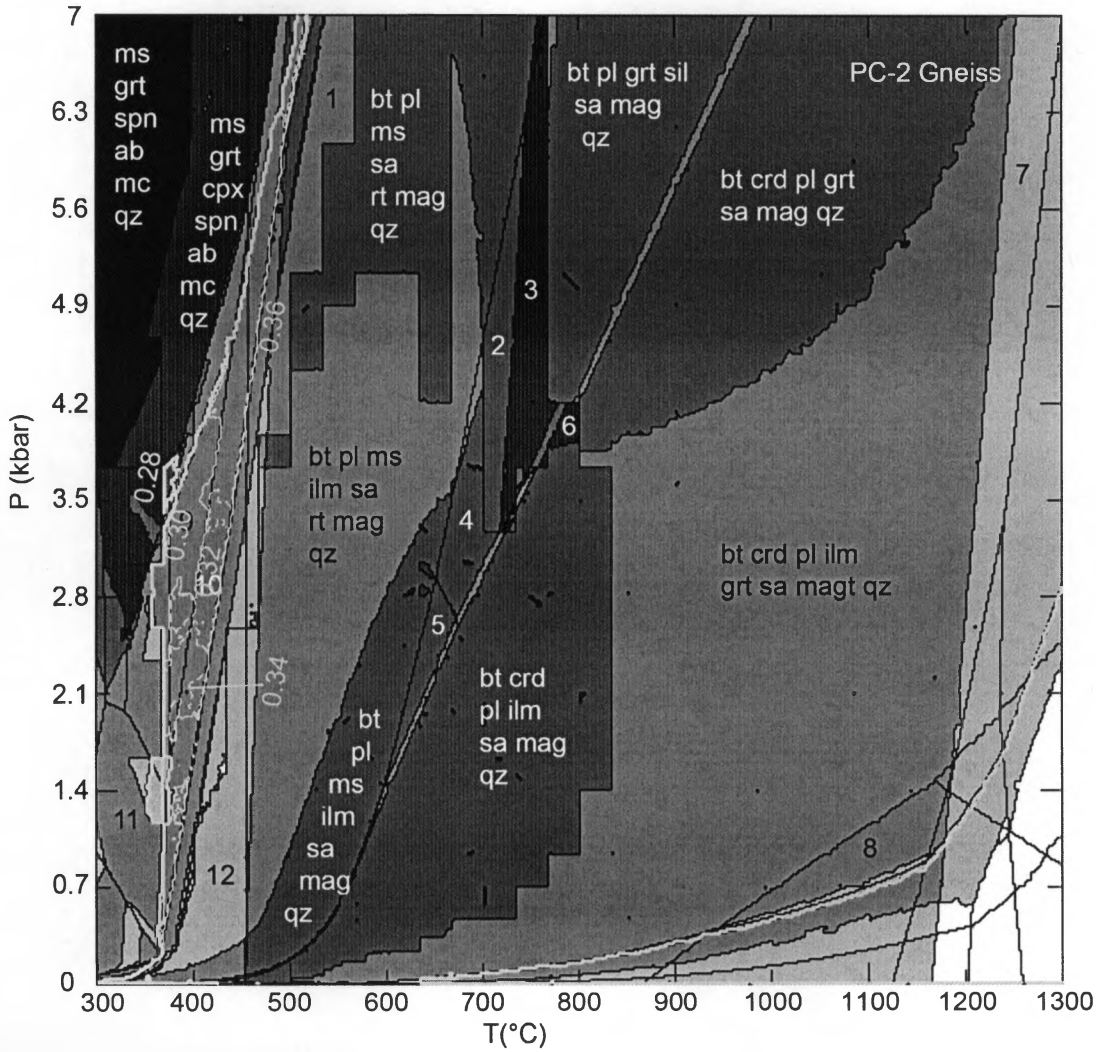

1 - bt pl ms grt sa rt mag qz
2 - bt pl sil sa rt mag qz
3 - bt pl sil sa mag qz
4 - bt pl ilm sil sa mag qz
5 - bt pl ilm and sa mag qz
6 - bt crd pl sa mag qz
7 - bt crd pl ilm grt sa mag abL qz
8 - bt crd pl ilm grt sa mag trd
9 - bt ms grt zo ep spn ab mc qz
10 - bt pl ms grt ep spn ab mc qz
11 - chl ms grt ep spn ab mc wrk qz
12 - bt pl ms ilm ab mc rt mag qz

(d) Isopleths of X(Mg) for PC-3 gneiss.

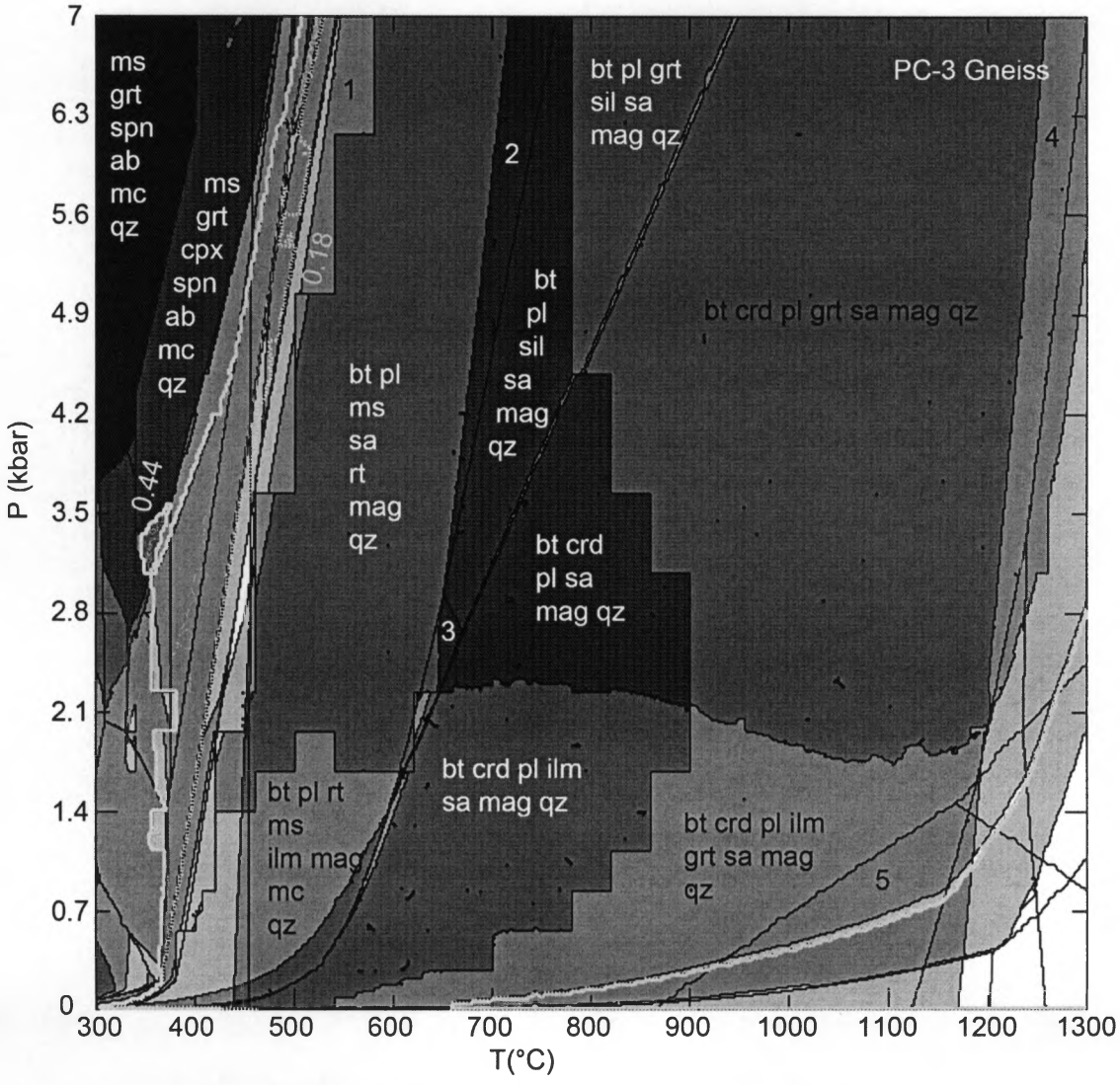

1 - bt pl ms grt sa rt mag qz
2 - bt pl ms sa mag qz
3 - bt pl and sa mag qz
4 - bt crd pl grt sa mag abL qz
5 - bt crd pl ilm grt sa mag trd

(e) Isopleths of X(Mg) for PC-21 gneiss.

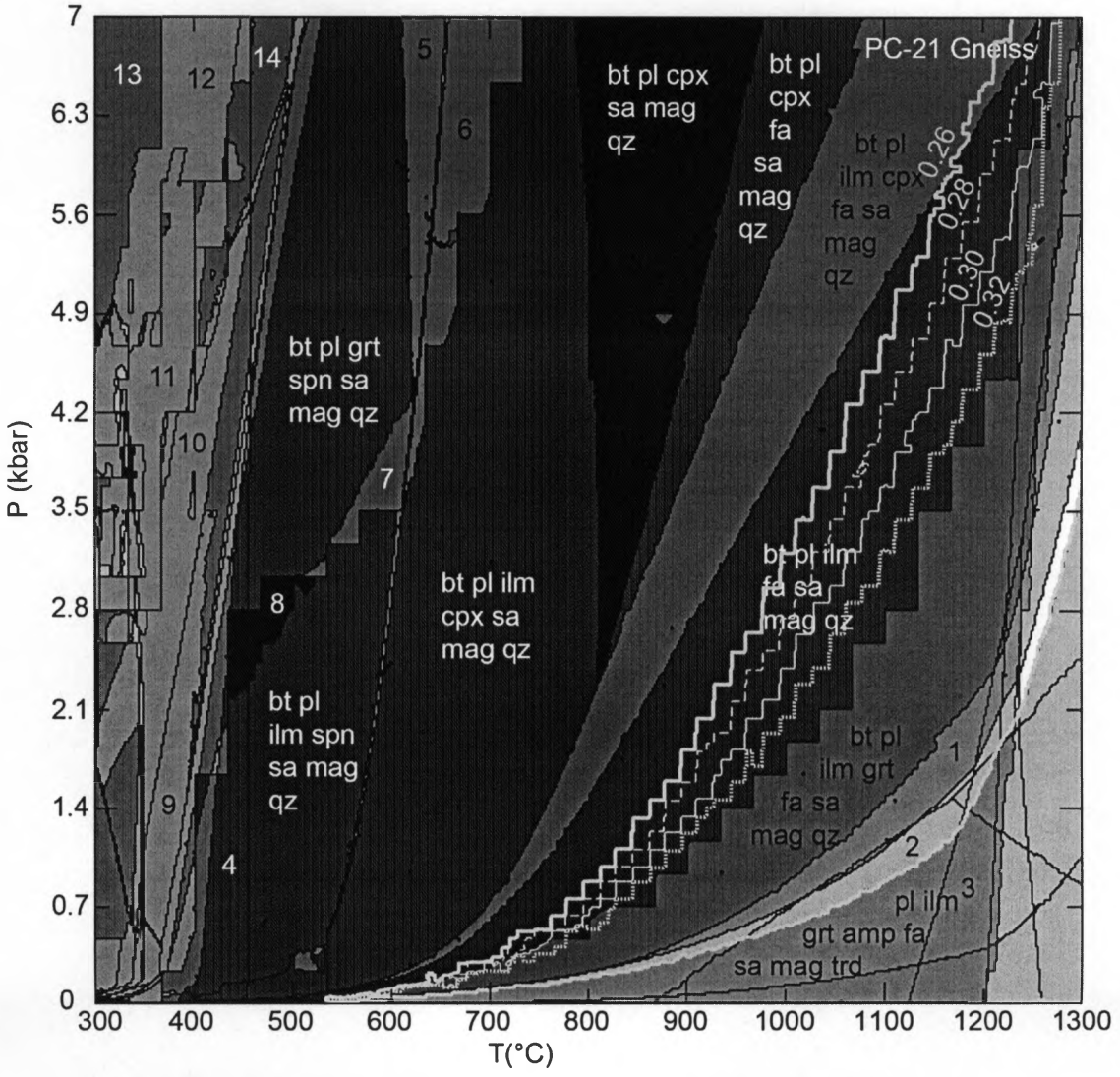

1 - bt pl ilm grt fa sa mag qz
2 - bt pl ilm grt amp fa sa mag trd
3 - pl ilm grt amp fa lct mag trd
4 - bt pl ilm spn mc mag qz
5 - bt pl grt cpx spn sa mag qz
6 - bt pl ilm cpx sa mag qz
7 - bt pl ilm grt spn sa mag qz
8 - bt pl spn sa mag qz
9 - bt ms grt ep spn ab mc mag qz
10 - bt ms grt ep spn rbk ab mc qz
11 - bt ms grt amp spn ab mc qz
12 - bt ms grt amp cpx spn ab mc qz
13 - ms grt amp cpx spn ab mc qz
14 - bt ms grt cpx spn ab sa qz

Note: ab-albite; abL-albite liquid; amp-amphibole; and-andalusite; bt-biotite; chl-chlorite; cpx-clinopyroxene; crd-cordierite; czo-clinozoisite; ep-epidote; fa-fayalite; grt-garnet;

hem-hematite; ilm-ilmenite; ky-kyanite; lc-leucite; lct-leucite; mc-microline; ms-muscovite; mag-magnetite; pl-plagioclase; qz-quartz; rbk-riebeckite; rt-rutile; sa-sanidine; sil-sillimanite; spn-sphene (titanite); trd-tridymite; wrk-wairakite; zo-zoisite.